Cynhadledd Ymchwil
Peirianneg Caerdydd

Cardiff Engineering
Research Conference

# Proceedings of the Cardiff University School of Engineering Research Conference 2024

EDITORS
Emiliano Spezi
Michaela Bray

CARDIFF
UNIVERSITY

PRIFYSGOL
CAERDYDD

School of Engineering
Ysgol Peirianneg

Cardiff
University
Press

Gwasg
Prifysgol
Caerdydd

# Proceedings of the Cardiff University School of Engineering Research Conference 2024

**CARDIFF UNIVERSITY**
**PRIFYSGOL CAERDYDD**

School of Engineering
Ysgol Peirianneg

EDITORS
Emiliano Spezi
Michaela Bray

# Contents

## Biobased Engineering

## Computational Modelling and Digital Twins

## AI and Deep Learning

# Net Zero

# Future Engineering

# Foreword

We are delighted to welcome you to the Proceedings of the Cardiff University School of Engineering Research Conference 2024. Launched in 2023, this conference is part of our initiative to foster a vibrant research culture and promote dissemination activities at the School of Engineering, Cardiff University, in Cardiff, United Kingdom. The conference provides a platform to celebrate achievements in various engineering disciplines, and to explore and discuss further advancements in the diverse fields that shape contemporary engineering. In this edition, the structure of the conference programme reflected the crosscutting themes and collaborative nature of our research and was built around current and emerging research areas in the School:

*Bio-based engineering* brings together all of the engineering topics that interface with medicine or biology. This theme recognises both the pivotal role technology plays in revolutionizing healthcare and the implementation of biological processes in providing novel solutions to engineering problems.

*Computational modelling and digital twins* represents cutting-edge research into virtual representations of objects or systems that are updated with real time information and used to guide decision making. Our research in this area focuses on developing smart materials and structures, and sustainable processes that help create a sustainable and greener economy.

*AI and deep learning* focuses on the application of artificial intelligence and machine learning techniques in engineering.  Our research in this field harnesses the power of AI in medical applications and in agriculture, improving the health and wellbeing of society.

*Net Zero* is a testament to our commitment to a greener, more efficient future. We aim to advance energy technology and play a key role in addressing the increasing demand for sustainable and low carbon technologies while reducing environmental impact and ensuring a sustainable environment. Our work helps to drive forward net-zero solutions for achieving the government carbon targets.

*Future engineering* represents state of the art technologies for the next generation such as wireless communication systems and future power systems engineering.  This theme showcases the exciting and emerging interdisciplinary work being done in the School of Engineering.

These proceedings embody the shared vision of engineers and researchers from our School as they work to tackle today's challenges and pave the way for a brighter future. We extend our heartfelt gratitude to all participants, presenters, and sponsors for their invaluable contributions to this effort, and we eagerly anticipate hosting this event again soon.

**Professor Emiliano Spezi**
*Organizing Committee Chair*
*Cardiff University School of Engineering*
*Research Conference 2024*

**Dr Michaela Bray**
*Organizing Committee Deputy Chair*
*Cardiff University School of Engineering*
*Research Conference 2024*

# Acknowledgements

## Green T
*Cardiff University*
*School of Dentistry*

## Ayre WN
*Cardiff University*
*School of Dentistry*

## Bigot S
*Cardiff University*
*School of Engineering*

## Brousseau E
*Cardiff University*
*School of Engineering*

## Bhaduri D
*Cardiff University*
*School of Engineering*

BIOBASED ENGINEERING

# Laser Surface Texturing of Bulk Metallic Glass for Orthopaedic Application

Osteoarthritis in weight bearing joints, such as the hip and knee, is the primary indicator for orthopaedic intervention in the UK. Joint replacements remain the only viable treatment for osteoarthritis, however implant metallics exhibit insufficiencies in their physical properties, producing high implant failure rates. Bulk metallic glasses (BMGs) have unique physical properties (high elasticity, high wear resistance) which can improve integration between biomaterials and host tissue. Laser surface texturing (LST) allows tuning of distinct surface properties, promoting favourable clinical outcomes (enhanced osseointegration). Following a comprehensive literature review on LST of BMGs, this work presents an experimental outline to assess how laser input parameters influence functional surface properties, in particular wettability, free energy, corrosivity, and surface chemistry. Future work will investigate both the antimicrobial properties of LST BMGs, and their propensity to modulate the host inflammatory response, with the goal of optimising LST parameters enhanced osseointegration of the peri-implant surface.

## INTRODUCTION

Osteoarthritis (OA) is a degenerative joint disease, characterised by progressive degradation of articular cartilage and the subsequent lysis of subchondral bone. OA affects around 10 million people in the UK [1], and its prevalence is expected to rise as a result of an increasingly obese and aging population. OA afflicts patients with joint pain and reduced mobility, costing the nation ~1% of gross national product (GNP) through operative care and lost working days [2].

Biomaterials are products which are engineered to interact with biological systems of the body for therapeutic or diagnostic purposes. Orthopaedic implants are an example of a biomaterial, utilised for the purposes of fixation, reconstruction, and realignment, and remain the only viable long-term treatment strategy for patients with moderate to high levels of joint degradation. Unfortunately, around 10% of orthopaedic implants fail within 10 years [3].

Structural and articulating components of orthopaedic implants have been manufactured from polycrystalline metals such as titanium alloys, cobalt chromium, and stainless steel. Whilst these materials have relatively low fabrication costs and are bioinert in nature [4], they also exhibit fairly poor long-term wear and corrosion resistance and are poorly reflective of the elasticity of their surrounding tissue; acting to induce stress-shielding events and resulting in peri-implant bone resorption.

Metallic glasses are a group of alloys with amorphous molecular structure, inherited from their liquid state. Since their experimental discovery by the research team of Pol Duwez [5], developments in their manufacturing process and compositional design, have vastly increased the size at which fully amorphous alloys can be produced.

Bulk metallic glasses (BMGs), i.e. metallic glasses with a critical diameter >1 mm, have advantageous physical properties such as high strength and fracture toughness, low elastic moduli, high elasticity, and high wear and corrosion resistance, which find them suitable for orthopaedic applications [6].

Surface texturing via micro- and nano-patterning of biomaterial surfaces can be used to tailor surface properties such as wettability, surface energy and topography. Such texturing may enhance the performance of orthopaedic implants as modulation of surface properties can influence extent of integration between the peri-implant surface and native bone. Nanosecond ($10^{-9}$ s) pulsed laser ablation is a laser surface texturing (LST) technique utilising short pulses of high intensity laser light to initiate melting and vaporisation at a material's surface and thus is capable of producing structured geometries, such as those presented in Fig. 1. Laser ablation demonstrates a number of advantages, e.g., high energy efficiency, low operation cost, and low contamination risk, over alternative surface texturing techniques such as sand-blasting and acid etching and photolithography.
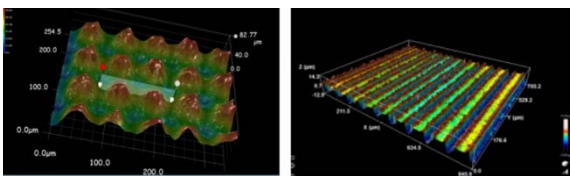


Fig. 1. Micro-pillar (left) and groove (right) surface patterning, produced via ns pulsed laser ablation [7,8].

## LITERATURE REVIEW

*Early investigations and single-pulse laser-texturing of BMGs*
Early investigations into ns pulsed laser ablation of BMGs were focused on observing topological and morphological features following modulation of laser parameters. Perhaps the first of these studies determined that increasing laser fluence (energy density) or decreasing laser scanning speed would increase the depth of machined features (Fig. 2), albeit with an increased likelihood of crystalline precipitation [7]. Irradiation of a BMG with a single pulse induces crater formation, the depth and diameter of which are primarily determined by the laser fluence and pulse duration. Often concentric ripple-like structures are observed at the circumference of this crater, attributed to the Kelvin-Helmholtz instability, resulting from the motion of vapour across the material melt-pool [8]. Finally, redeposited material is observed towards and beyond the crater circumference, resulting from the generation of recoil pressure during material vaporisation, and subsequent melt ejection [9].

*Physical and functional properties of ns laser-textured BMGs*
Recent work has focused on texturing of larger BMG surface areas, as well as how LST may influence certain surface properties. It has been suggested that increasing laser scanning speed can improve the resolution of textured surface features via a reduction in melt ejection and its resulting redeposition. Further augmentations in scanning speed, however, may subsequently lower feature definition due to a loss of the laser-material interaction time [10], as such texturing of defined surface geometries (e.g., cross-hatch, grooves, dimples), requires parameter optimisation.

Interestingly, a change from classical concave to convex, and a return to concave texturing has been reported, dependent on pulse overlap and applied pulse energy. The concave-convex transition occurs through a change in the surface tension gradient, and a resulting switch in the direction of the Marangoni effect producing a regime of laser texturing via 'pulling' of the surface [11].

LST in the nanosecond regime influences surface wettability, however the mechanism by which this occurs remains debated. Jiao, et al. [12] suggested that the wettability of the commercially available BMG Vitreloy 105 (Vit105) decreased following LST, resulting from a removal of hydrophilic carbonyl (C=O) and carboxyl (O=C-O) groups, and a degeneration of the surface oxide layer. It was stipulated, however, that wettability may still be increased by laser texturing, albeit in a morphology-dependent manner. In contrast, subsequent work has suggested that ns LST enhances surface wettability, by increasing surface oxidation [10]. Separately, surface hardening of up to ~39% of a Ti-based BMG following LST was attributed to surface oxidation [13].

Whilst the above highlights the potential for ns LST to modulate surface properties in an input-parameter dependent manner, additional investigation is imperative to assess these relationships before they can be optimised for orthopaedic application.

*Biological response to ns laser-textured BMGs*
In consideration of the antimicrobial performance of LST BMGs, increasing pulse power and decreasing scanning speed is reported to increase surface roughness and wettability, as well as promote ion (Cu2+ and Ni2+) release and production of reactive oxygen species (ROS) on Zr-BMG

surfaces textured with a pulse overlap of 66%. Bacterial colony formation of *S. aureus* was observed to be reduced following LST, albeit only significantly so on surfaces with scanning speeds between 10-100 mm/s [14]. Unfortunately, laser texturing at these scanning speeds was also associated with an increase in crystalline precipitate formation, which can negatively affect the material's physical property
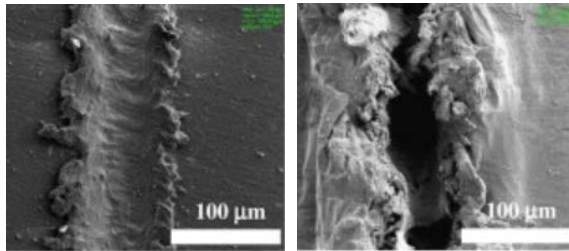


performance. Further work is needed to establish the antimicrobial mechanism of LST BMGs.

Fig. 2. A reduction in pulsed laser scanning speed from 300 mm/s (left) to 30 mm/s (right), at constant fluence (12 J/cm2), is associated with increased machining depth and material redeposition [7].

Regarding the regenerative capacity of LST BMGs, MG-63 human osteoblasts cultured on dimple and groove-patterned Vit105 have been shown to exhibit increased cell viability, compared to cells cultured on smooth samples. Furthermore, cells on groove-patterned samples exhibited a significant increase (p<0.05) in proliferation when compared to as-cast surfaces. This increase in proliferative activity was correlated with cell alignment along textured grooves (Fig. 2), providing evidence to suggest that the BMG provides both a biocompatible material surface, and that considered application of LST may promote regenerative phenotypic responses [15].

Overall, several distinct gaps remain within the literature regarding ns LST of BMGs for orthopaedic application. Foremost is a lack of a systematic investigation into how laser parameters influence BMG surface characteristics, and consequently functional surface properties. Additionally, the literature review outlined above remains the only research regarding biological responses to ns LST of BMGs. Thus, considerable investigation into both the antimicrobial and regenerative potential of these surfaces is required to enhance their clinical performance.
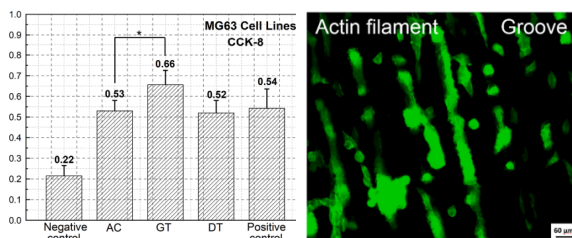


Fig. 3. MG-63 osteoblasts exhibit increased proliferation on ns LST groove-patterned Vit105 surfaces (left). Cells undergo contact guidance and align along groove patterning (right) [8].

**METHODOLOGY OF THE PRESENT RESEARCH**

*Materials and laser system*
A commercially available BMG, AMLOY-Zr02, with a nominal composition of $Zr_{65}Cu_{16}Ni_{12}Al_4Ti_3$, purchased from Heraeus (Germany) will be used for the present research on the LST of BMG. Laser surface texturing will be conducted

using a Yb-doped fiber laser system (SPI lasers, UK) with a wavelength of 1064 nm and 32 µm nominal spot diameter. Laser parameters are defined by pre-set waveform specifications, as outlined in Table 1, and are to be chosen as experimentally appropriate.

*Influence of independent laser parameters on surface properties - Initial investigations*
Preliminary investigations will involve assessment of the influence of laser input parameters on surface characteristics, with the aim of accounting for confounding factors which may influence surface functional properties. This will be split into two sections:

i.    Influence of pulse duration and applied fluence on surface characteristics.

Pulse duration, according to the waveforms outlined in Table 1, and fluence will be varied at a constant pulse overlap value. This analysis will allow pulse duration to be accounted for in the assessment of the effect of laser parameters on functional surface properties.

| Waveform | Pulse duration (ns) | Frequency (kHz) | $E_{max}$ (mJ) |
|---|---|---|---|
| 11 | 220 | 35 | 0.57 |
| 16 | 140 | 51 | 0.39 |
| 22 | 65 | 80 | 0.25 |

Table 1. Preset laser waveform specifications.

ii.    Influence of pulse overlap on surface characteristics.

For a given pulse duration (e.g., 220 ns, waveform 11), applied fluence will be kept constant, and the influence of varying pulse overlap on surface characteristics will be assessed. In each of these instances surface characterisation will entail consideration of resulting topographies via evaluation of surface roughness, as well as quantification of the depth and width of morphological features, and the height of redeposited material following melt ejection.

*Influence of ns laser-texturing on functional surface properties.*
In order to determine which laser input parameters most significantly influence BMG surface characteristics, a full-factorial design of experiments (DOE) approach will be utilised, according to Table 2.

| Fluence (J/cm2) | Scanning speed (mm/s) |
|---|---|
| 10 | 50 |
| 20 | 100 |
| 30 | 150 |
| 40 | 200 |
| 50 | 250 |
| 60 | 300 |
| 70 | 350 |

Table 2. DOE for investigation into influence of laser input parameters on BMG surface properties.

Additionally, particular sample groups i.e., low, mid, and high values, will be taken forward for assessment of functional surface properties, specifically: wettability, surface energy, corrosivity, and surface chemistry, as well as for analysis of surface crystallinity.

**CONCLUSIONS AND FUTURE DIRECTIONS OF RESEARCH**

Nanosecond pulsed laser ablation has been identified as an energy-efficient technique for reproducible biomaterial surface texturing, with low associated contamination risk. Variations in particular laser input parameters are associated with changes in surface characteristics, and consequently functional surface properties. The research proposed in this paper will systematically investigate these relationships, with the goal of enhancing the design and long-term osseointegration of orthopaedic implants.

To further meet this aim, future work will investigate the biological responses to ns LST AMLOY-Zr02. This will initially be achieved via assessment of the response of THP-1 derived macrophages, as a model for the host response, to differentially textured surfaces. Directing macrophages towards anti-inflammatory phenotypes is associated with enhanced osseointegration at the peri-implant surface and may improve clinical implant success rates.

Additionally, changes in bacterial adhesion and biofilm formation have been associated with variations in biomaterial wettability and surface roughness. As such, the antimicrobial activity of LST AMLOY-Zr02 will be assessed using the bacterial strains most associated with orthopaedic infection: *S. aureus* and *P. aeruginosa*. Optimisation of antimicrobial LST may provide two significant contributions to the application of biomaterials. Firstly, the reliance on antibiotics may be lessened, alleviating the occurrence and pathogenic antibiotic resistance. Additionally, the prevalence of post-operative infection, caused by the presence of dormant bacteria and the biomaterial surface may be reduced, thereby improving the likelihood of successful clinical outcomes such as enhanced peri-implant osseointegration and reduced rates of infection.

*Conflicts of Interest*
*The authors declare no competing conflicts of interest.*

**REFERENCES**

[1]  VersusArthritis, The state of musculoskeletal health 2023: *Arthritis and other musculoskeletal conditions in numbers*, 2023 [online]. Available: https://www.versusarthritis.org

[2]  R. Bitton, 'The economic burden of osteoarthritis', *Am. J. Manag. Care*, vol. 15, no. 8 Suppl, pp. S230-235, Sep. 2009. PMID 19817509.

[3]  NJR,  *National Joint Registry for England and Wales 20th Annual Report*, 2023 [online]. Available at https://reports.njrcentre.org.uk/downloads

[4]  D.C. Tapscott and C. Wottowa, 'Orthopedic Implant Materials', in *StatPearls*, Treasure Island (FL): StatPearls Publishing, 2024 [online]. Available: http://www.ncbi.nlm.nih.gov/books/NBK560505/

[5]  W. Klement, R.H. Willens, and P. Duwez, 'Non-crystalline Structure in Solidified Gold–Silicon Alloys', *Nature*, vol. 187, no. 4740, pp. 869–870, Sep. 1960. doi.org/10.1038/187869b0

[6]  Y.Q. Cheng and E. Ma, 'Atomic-level structure and structure–property relationship in metallic glasses', *Progress in Materials Science*, vol. 56, no. 4, pp. 379–473, May 2011. doi.org/10.1016/j.pmatsci.2010.12.002

[7]  H.-K. Lin, C.-J. Lee, T.-T. Hu, C.-H. Li, and J. C. Huang, 'Pulsed laser micromachining of Mg–Cu–Gd bulk metallic glass', *Optics and Lasers in Engineering*, vol. 50, no. 6, pp. 883–886, Jun. 2012. doi.org/10.1016/j.optlaseng.2012.01.003

[8]  Y. Zhu, J. Fu, C. Zheng, and Z. Ji, 'Effect of nanosecond pulse laser ablation on the surface morphology of Zr-based metallic glass', *Optics & Laser Technology*, vol. 83, pp. 21–27, Sep. 2016. doi.org/10.1016/j.optlastec.2016.03.021

[9]  Y. Liu, M.Q. Jiang, G.W. Yang, J.H. Chen, Y. J. Guan, and L.H. Dai, 'Saffman–Taylor fingering in nanosecond pulse laser ablating bulk metallic glass in water', *Intermetallics*, vol. 31, pp. 325–329, Dec. 2012. doi.org/10.1016/j.intermet.2012.07.014

[10]  Q. Wang, Y. Cheng, Z. Zhu, N. Xiang, and H. Wang, 'Modulation and Control of Wettability and Hardness of Zr-Based Metallic Glass via Facile Laser Surface Texturing', *Micromachines*, vol. 12, no. 11, p. 1322, Oct. 2021. doi.org/10.3390/mi12111322

[11]  M. Cui, H. Huang, L. Zhang, and J. Yan, 'Nanosecond Laser "Pulling" Patterning of Micro–Nano Structures on Zr-Based Metallic Glass', *Small*, vol. 19, no. 14, p. 2206516, Apr. 2023. doi.org/10.1002/smll.202206516

[12]  Y. Jiao *et al.*, 'Investigations in the fabrication of surface patterns for wettability modification on a Zr-based bulk metallic glass by nanosecond laser surface texturing', *Journal of Materials Processing Technology*, vol. 283, p. 116714, Sep. 2020 doi.org/10.1016/j.jmatprotec.2020.116714

[13]  H. Zhang, H. Wu, L. Zhang, M. Jiang, H. Huang, and J. Yan, 'Surface hardness and scratch characteristics of nanosecond laser colored Ti-based metallic glass', *Journal of Alloys and Compounds*, vol. 970, p. 172659, Jan. 2024. doi.org/10.1016/j.jallcom.2023.172659

[14]  C. Du, W. Chengyong, T. Zhang, H. Peng, J. Sui and L. Zheng, 'Antibacterial performance of nanosecond laser irradiated zirconium-based bulk metallic glass', *Authorea*, 2020 [preprint withdrawn].

[15]  Y. Jiao *et al.*, 'In vitro cytocompatibility of a Zr-based metallic glass modified by laser surface texturing for potential implant applications', *Applied Surface Science*, vol. 547, p. 149194, May 2021. doi.org10.1016/j.apsusc.2021.149194

## Zhu H

*Cardiff University*
*School of Engineering*

## Zhang Z

*Cardiff University*
*School of Engineering*

COMPUTATIONAL MODELLING AND DIGITAL TWINS

# Interpenetrating Composites with Enhanced Stiffness, Desired Poisson's Ratio and Superior Conductivity

Fibre matrix debonding, fibre pullout, delamination and mechanical anisotropy are the main common disadvantages of most fibre-reinforced composites. Interpenetrating phase composites (IPCs), however, do not have these problems because both their matrix material and their reinforcement fibre materials are self-connected networks, and interpenetrate each other. Moreover, IPCs could be designed to have an almost isotropic Young's modulus much larger than the Voigt limit, and a Poisson's at a desired value (i.e. positive, or negative or zero). In addition, they could have an isotropic thermal or electrical conductivity very close to the theoretical upper limit (i.e. the Hashin—Shtrikman's upper limit). This paper will introduce the relevant theoretical, simulation and experimental results on the elastic properties and thermal/electrical conductivities of some IPCs and compare their properties with those of other types of composites.

## INTRODUCTION

Fibre composites are widely used in engineering applications, in which the fibres are usually much stronger and stiffer than the matrix material and used to reinforce the matrix material. To make the best use of the reinforcement material, it is very important that the reinforcement material is self-connected to form a network structure. For example, in modern buildings, bridges or water containing dams, the reinforcement steel bars are welded together to form a self-connected network, and the concrete material (i.e. the matrix material) is then casted into the porous space of the steel network. If the reinforcement steel bars are not self-connected, even if the same amount of the reinforcement steel material is used in buildings, bridges or dams, these structures could easily fall apart. Thus, in conventional fibre composites, the reinforcement fibres are in general not best used. Their common disadvantages include fibre matrix debonding, fibre pullout, delamination and mechanical anisotropy, etc [1]. In contrast, interpenetrating phase composites (IPCs) can avoid all these disadvantages because the reinforcement phase is a self-connected network. By theoretical analysis and computational simulations, Zhu et al. [2,3] and Zhang et al. [4,5] have found that IPCs could have an almost isotropic Young's modulus much larger than the Voigt limit, a Poisson's ratio at a desired value (i.e. positive, negative or zero), and a thermal or electrical conductivity close to the Hashin-Shtrikman's upper limit[6]. The aim of this paper is to highlight the advantages of IPCs over the fibre or particle composites.

## MATERIAL MODELS

In our theoretical and simulation research works, the IPCs are reinforced by a self-connected periodic regular fibre network or a lattice structure. Thus, periodic representative volume elements (RVEs) and periodic boundary conditions can be used to obtain the elastic properties and thermal/electrical conductivities. Based on the geometric feature of the reinforcement network structure, the IPCs are classified into two main types: normal and auxetic. In the normal IPCs as shown in Fig. 1, the reinforcement fibre network is a normal network or lattice which has a positive Poisson's ratio. In the auxetic IPCs as shown in Fig. 2, the reinforcement fibre network is an auxetic network or lattice which has a negative Poisson's ratio. In theoretical analysis, the reinforcement fibre network and the matrix are divided into a number of blocks. In finite element simulations, both the reinforcement fibre network and the matrix are partitioned into a large number of tetrahedral elements.
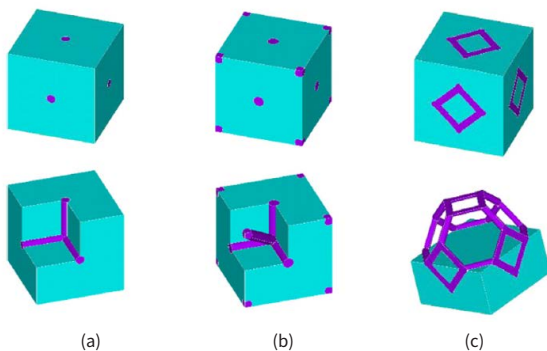


Fig. 1. Different types of normal IPCs: (a) type I, (b) type II, (c) type III.
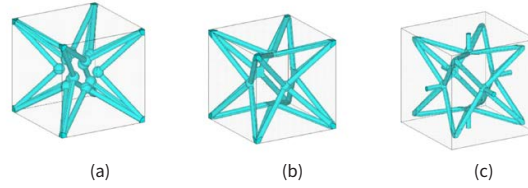


Fig. 2. Different types of auxetic IPCs: (a) type I, (b) type II, (c) type III.

## RESULTS

*Enhanced Young's modulus*
The Voigt limit has long been regarded as the upper limit for the Young's moduli of isotropic composites [1]. For composites composed of a reinforcement material with a Young's modulus of $E_f$ and a matrix material with a Young's modulus of $E_m$, the Voigt limit is given as

$$E_{Voigt} = E_f V_f + E_m V_m \qquad (1)$$

where $V_f$ and $V_m$ are the volume fractions of the fibre and matrix materials in the composites, respectively, and $V_f + V_m = 1$.

To make the theoretical and the finite element simulation results of the IPC more useful, the Young's modulus of the matrix material is assumed to be 1, and the Young's modulus of the reinforcement fibre material is the value of $E_f / E_m$, i.e. the ratio of the actual Young's modulus of the fibre material to that of the matrix material. Further, the obtained Young's of the IPC is normalized by the Voigt limit given by Eq. (1).

For different types of IPCs reinforced by a normal fibre network shown in Fig. 1, the effects of the different combinations of the constituent material properties on the normalized Young's moduli of the IPCs are presented in Fig. 3.
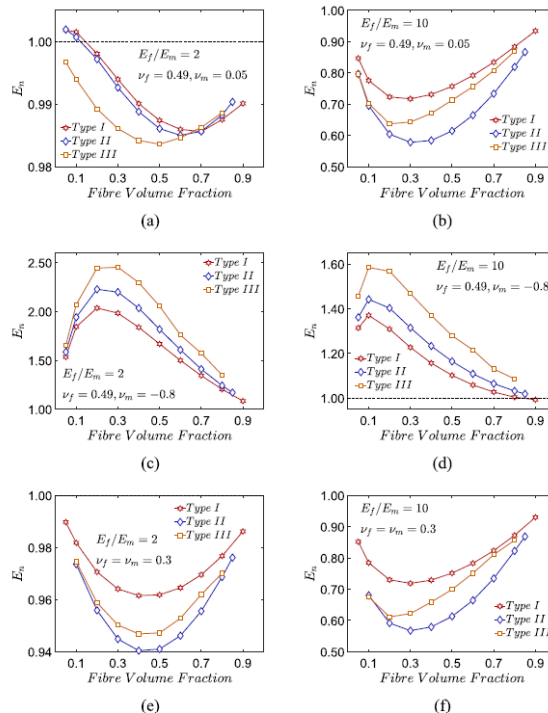


Fig. 3. Effects of the different combinations of the constituent material properties on the normalized Young's modulus of different types of normal IPCs [5], where $v_f$ and $v_m$ are the Poisson's ratios of the fibre and matrix materials, respectively.

Both the constituent materials, i.e. the fibre and matrix, are assumed to be isotropic. Thus, the possible range of their Poisson's ratio is (-1.0, 0.5). The theoretical [2] and finite element simulation [5] results indicate that the elastic properties of the IPCs are nearly isotropic. The results in Fig. 3(c) and 3(d) show clearly that the Young's moduli of the IPCs could be much larger than the Voigt limit, and therefore much larger than those of the conventional particle or fibre composites. In general, the larger the difference between the Poisson's ratios of the matrix and the reinforcement fibre materials, or the smaller the difference between the Young's moduli of the two constituent materials, the larger will be normalized Young's modulus of the IPCs. It is noted that for different types of IPCs [4] reinforced by an auxetic fibre network shown in Fig. 2, their Young's moduli are in general smaller that those of the IPCs reinforced by a normal fibre network, but still much larger than those of the conventional particle or fibre reinforced composites. It is also worth noting that for the same given amounts of the matrix and reinforcement materials, if the geometric structure of the reinforcement material is a perfect regular closed cell foam with a uniform wall thickness and the matrix material fills the identical cubic cells, the resultant composite [7] has the largest nearly isotropic Young's modulus. This is because among all the possible geometrical structures of the self-connected porous reinforcement material, the regular closed-cell foam structure with identical cubic cells and uniform wall thickness has the largest nearly isotropic stiffness. However, this type of composites is not IPC because its matrix material/phase doesn't form a self-connected network.

*Desired value of Poisson's ratio*
For different types of IPCs with different fibre volume fractions and reinforced by a normal fibre network shown in Fig. 1, the effects of the different combinations of the constituent material properties on the Poisson's ratio of the IPCs are demonstrated in Fig. 4. As can be seen, if both the matrix and the fibre materials have a positive Poisson's ratio, the Poisson's ratio of the IPCs would always be positive [5]. If the matrix material has a large magnitude of negative Poisson's ratio, the Poisson's ratio of the IPCs could have a large magnitude negative Poisson's ratio.

For different types of IPCs with different fibre volume fractions and reinforced by an auxetic fibre network shown in Fig. 2, the effects of the different combinations of the constituent material properties on the Poisson's ratio of the IPCs [4] are demonstrated in Fig. 5. In contrast to the results of the IPCs reinforced by a normal fibre network, even if the Poisson's ratios of both the matrix and the fibre materials are positive, the IPCs reinforced by an auxetic fibre network can have a large magnitude negative Poisson's ratio.

Based on the results demonstrated in Figs. 4 and 5, it is concluded that the Poisson's ratio of PCs could be designed to achieve a desired value (i.e. positive, or negative or zero) by carefully choosing the combination of the properties of the constituent materials.
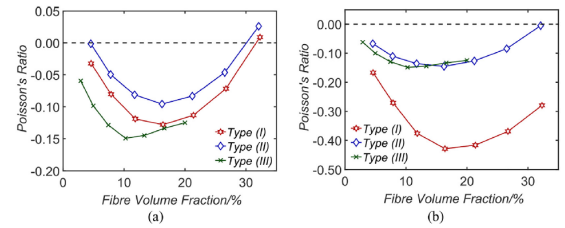


Fig. 5. Effects of fibre volume fraction on the Poisson's ratio of the composites [4] when $\alpha = 20°$. (a) $v_m = 0.1$, $v_f = 0.25$, $E_f / E_m = 1000$; (b) $v_m = 0$, $v_f = 0.25$, $E_f / E_m = 1000$.

*Superior conductivity*
In two phase composites, the constituent fibre and matrix are assumed to be homogenous and isotropic materials A and B, with conductivities $\mu_A$ and $\mu_B$ and volume fractions $V_A$ and $V_B$, respectively.

For composites with anisotropic conductivity, the largest and the smallest possible effective conductivities can be easily achieved if the two constituent materials A and B are uniformly arranged in parallel, for example, sandwich/laminate composites with layers of uniform thickness. For such anisotropic composites, their upper limit of conductivity is given by $\mu_U = \mu_A V_A + \mu_B V_B$ and their lower limit is given as $\mu_L = \frac{\mu_A \mu_B}{\mu_A V_B + \mu_B V_A}$ where $V_A + V_B = 1$.

For composites with isotropic conductivity, the magnitude of the conductivity is limited by the Hashin and Shtrikman's upper and lower bounds [6].

$$\mu_{HS\_U} = \mu_A + \frac{V_B}{\frac{1}{\mu_B - \mu_A} + \frac{V_A}{3\mu_A}} \qquad (2)$$

$$\mu_{HS\_L} = \mu_B + \frac{V_A}{\frac{1}{\mu_A - \mu_B} + \frac{V_B}{3\mu_B}} \qquad (3)$$

where it is assumed that $\mu_A \geq \mu_B$.

For IPCs reinforced by the normal type-I fibre network with $V_A = 0.104$, the relationship between the effective conductivity and the ratio $\mu_A / \mu_B$ has been obtained by theoretical analysis and finite element simulation using ABAQUS [3]. Fig. 6 shows the effects of the ratio $\mu_A / \mu_B$ on the effective conductivity of such IPCs, where different bounds/limits are plotted for comparison [3] and the results are normalized by $\mu_B$.
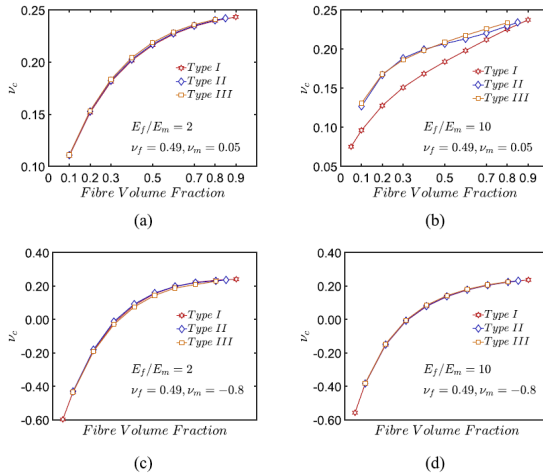


Fig. 4. Effects of the different combinations of the constituent material properties on the Poisson's ratio of different types of normal IPCs [5] reinforced by a normal fibre network.

As can been seen, the theoretical results are very close to those of the finite element simulation results, and the conductivities of the IPCs are closer to the Hashin-Shtrikman's upper bound than to their lower bound (see Fig. 6), and much larger than the experimentally measured results of the conventional particle or short- fibre composites, as shown in Fig. 7.
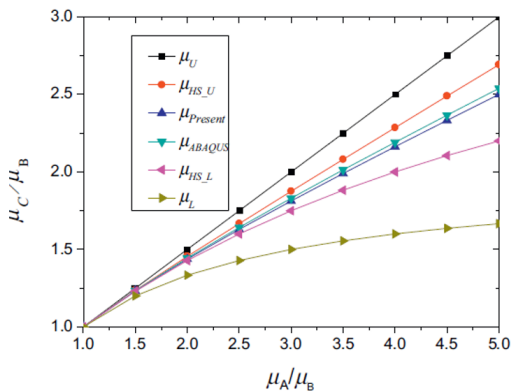


Fig. 6. Effects of $\mu A / \mu B$ on the conductivity of IPCs reinforced by a normal type-I fibre network [3], where the fibre volume fraction $V_A$ = 0.104.
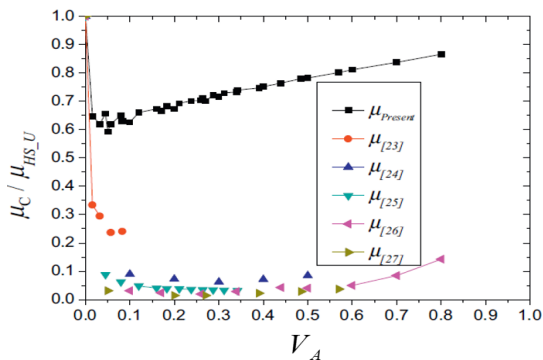


Fig. 7. Comparison between the conductivities of IPCs and the experimentally measured results of the conventional particle and short-fibre composites, where the results are normalized by the Hashin-Shtrikman's upper limit.

It is noted that for the same given amounts of the matrix and reinforcement materials, if the geometric structure of the reinforcement material is a perfect regular cubic closed cell foam with a uniform wall thickness and the matrix material fills the identical cubic cells, the resultant composite will have the largest isotropic conductivity [7], which is exactly the same as the Hashin-Shtrikman's upper limit. However, such composite is not an IPC.

**DISCUSSION AND CONCLUSIONS**

It is relatively easy to manufacture IPCs. The regular reinforcement fibre network structure can be produced first, the matrix material (e.g. concrete, resin, or polymer) can then be casted into the self-connected porous network of the reinforcement structure. The theoretical and finite element simulation results have demonstrated that for the same amounts of the constituent matrix and reinforcement materials used, IPCs can have a much larger nearly isotropic Young's modulus than those of the conventional particle or short fibre composites. Further, the nearly isotropic Young's modulus of IPCs could be designed to be much

larger than the Voigt limit that was generally regarded as the unexceedable upper limit for all composites. In addition, IPCs can be designed as functional material with a Poisson's ratio at a desired value, e.g. positive, or negative, or zero. Moreover, IPCs have a conductivity significantly larger than those of the conventional particle and short-fibre composites. Therefore, IPCs have very important engineering applications in many different areas.

*Conflicts of Interest*
*The authors declare no conflict of interest.*

**REFERENCES**

[1]    D. Hull and T. W. Clyne, *An Introduction to Composite Materials*, 2nd ed. Cambridge University Press, 1996. doi.org/10.1017/CBO9781139170130

[2]    H. Zhu, T. Fan, C. Xu, and D. Zhang, 'Nano-structured interpenetrating composites with enhanced Young's modulus and desired Poisson's ratio', *Composites Part A: Applied Science and Manufacturing*, vol. 91, pp. 195–202, Dec. 2016. doi.org/10.1016/j.compositesa.2016.10.006

[3]    H. Zhu, T. Fan, and D. Zhang, 'Composite Materials with Enhanced Conductivities', *Adv. Eng. Mater.*, vol. 18, no. 7, pp. 1174–1180, Jul. 2016. doi.org/10.1002/adem.201500482

[4]    Z. Zhang *et al.*, 'Auxetic interpenetrating composites: A new approach to non-porous materials with a negative or zero Poisson's ratio', *Composite Structures*, vol. 243, p. 112195, Jul. 2020. doi.org/10.1016/j.compstruct.2020.112195

[5]    Z. Zhang *et al.*, 'The near-isotropic elastic properties of interpenetrating composites reinforced by regular fibre-networks', *Materials & Design*, vol. 221, p. 110923, Sep. 2022. doi.org/10.1016/j.matdes.2022.110923

[6]    Z. Hashin and S. Shtrikman, 'A variational approach to the theory of the elastic behaviour of multiphase materials', *Journal of the Mechanics and Physics of Solids*, vol. 11, no. 2, pp. 127–140, Mar. 1963. doi.org/10.1016/0022-5096(63)90060-7

[7]    H. X. Zhu, T. X. Fan, and D. Zhang, 'Composite materials with enhanced dimensionless Young's modulus and desired Poisson's ratio', *Sci. Rep.*, vol. 5, no. 1, p. 14103, Sep. 2015. doi.org/10.1038/srep14103

Zhang X

*Cardiff University*
*School of Engineering*

Cleall P

*Cardiff University*
*School of Engineering*

Sapsford D

*Cardiff University*
*School of Engineering*

COMPUTATIONAL MODELLING AND DIGITAL TWINS

# Exploring the Circular Economy Potential of the ASPIRE Method: A Numerical Study on Copper Ion Trapping

This study explores the Accelerated Supergene Processes in Repository Engineering (ASPIRE) concept for long-term trapping of copper ions from contaminated water using numerical simulations. The ASPIRE method offers a sustainable approach to water remediation and resource recovery through permeable reactive barriers. A numerical framework, based on unsaturated soil mechanics and reactive transport, is presented, considering water flow, copper ion transport, adsorption, and precipitation. A case study evaluates the ASPIRE concept's performance over a 5-year period, demonstrating the system's effectiveness in capturing approximately 45,000 kg of copper. Adsorption and precipitation mechanisms contribute to the enrichment process. The study highlights the importance of monitoring and maintenance to address potential challenges like clogging. The findings support the feasibility of the ASPIRE concept as a promising approach for simultaneous water remediation and resource recovery, aligning with circular economy principles.

## INTRODUCTION

The treatment of contaminated wastewater is a critical environmental challenge that requires effective remediation methods. While numerous techniques have been developed to address this issue, the focus has primarily been on purifying wastewater sources by removing contaminants. However, a novel approach known as the accelerated supergene processes in repository Engineering (ASPIRE) method [1–3]at the same time, they must sustainably manage continued multimillion tonne annual arisings of mineral-dominated wastes from mining and industry. In an antithesis of circular economy principles, these wastes continue to be landfilled despite often comprising valuable components, such as critical metals, soil macronutrients and mineral components which sequester atmospheric carbon dioxide ($CO2$, shifts the paradigm by emphasizing the enrichment of valuable metal materials in contaminated water for potential future utilization.

In contrast to conventional methods like "Pump and Treat," which can be energy-intensive and limited in scale, the ASPIRE method offers a more sustainable and passive approach through the use of permeable reactive barriers (PRBs). PRBs have been extensively studied for their efficacy in removing specific contaminants from groundwater, mine drainage, etc., showcasing their potential in environmental remediation. The unique advantage of the ASPIRE method lies in its dual functionality of purifying wastewater and concentrating valuable metals, aligning with the principles of a circular economy by promoting resource recovery.

Before real-world implementation, it is crucial to evaluate the ASPIRE concept's feasibility and potential outcomes through numerical simulations. This study aims to investigate the ASPIRE concept's capabilities, providing valuable insights for further development and decision-making.

## THE NUMERICAL FRAMEWORK

In this section, the governing equations of the numerical framework that describe the transport of liquid and ionic species within the trapping area are presented.

*Wastewater flow*
In practical implementations, the ASPIRE concept's capture zone may experience unsaturated conditions due to its interaction with the surrounding environment. To properly describe wastewater flow in this context, we employed the theory of unsaturated soil mechanics [4] in our numerical simulations.

$$S_r \rho_w \frac{\partial n}{\partial t} - \frac{nC_m}{g} \frac{\partial s}{\partial t} + nS_r \frac{\partial \rho_w}{\partial t}$$
$$- \nabla \cdot (nS_r D_w)\nabla \rho_w + \nabla \cdot (\rho_w v_w) = 0 \tag{1}$$

where $S_r$ (-) is the saturation, $\rho_w$ (kg·m$^{-3}$) is the wastewater density, $n$ (-) is the porosity, $t$ (s) is the time, $C_m$ (m$^{-1}$) is the specific liquid wastewater capacity, $g$ (m·s$^{-2}$) is the gravity acceleration, $s$ (Pa) is the total suction, $D_w$ (m$^2$·s$^{-1}$) is the wastewater diffusivity.

The Darcy type flow is used for the description of solution flow in the unsaturated trap porous material by considering the driving forces of suction and gravity:

$$v_w = \frac{\kappa \cdot \kappa_{rw}}{\mu_w} \nabla(s + \rho_w gD) \tag{2}$$

where $v_w$ (m·s$^{-1}$) is the liquid wastewater velocity, $\kappa$ (m$^2$) is the intrinsic saturated wastewater permeability, $\kappa_{rw}$ (-) is the relative wastewater permeability, $\mu_w$ (Pa·s) is the dynamic viscosity of wastewater, $D$ (m) is the wastewater head.

Besides, the intrinsic saturated wastewater permeability is obtained through the original Kozeny-Carman equation:

$$\kappa = \frac{\kappa_0(1 - n_0)^2}{n_0{}^3} \cdot \frac{n^3}{(1 - n)^2} \tag{3}$$

where $\kappa_0$ (m$^2$) is the initial intrinsic saturated wastewater permeability, $n$ (-) is the initial porosity.

*Copper ion transportation and precipitation*
The copper ions are considered a dilute species and are transported along with the wastewater flow in unsaturated media. During the transport process, the effects of dispersion, diffusion, chemical reactions, and precipitation are taken into account.

$$\frac{\partial(nS_r c_i)}{\partial t} + r_{ads,i} = nS_r \cdot (r_{eq,i} + r_{kin,i}) \tag{4}$$
$$- \nabla \cdot (\rho_w \nu_w c_i - (D_{d,i} + D_{e,i})\nabla c_i)$$

where $c_i$ (mol·m$^{-3}$) is the concentration of aqueous species, $D_{d,i}$ (m$^2$·s$^{-1}$) and $D_{e,i}$ (m$^2$·s$^{-1}$) are the effective dispersion and diffusion tensor of aqueous species, respectively. $r_{ads}$ (mol·m$^{-3}$·s$^{-1}$), $r_{eq,i}$ (mol·m$^{-3}$·s$^{-1}$) and $r_{kin,i}$ (mol·m$^{-3}$·s$^{-1}$) are the reaction rates caused by adsorption, equilibrium chemical reaction and kinetic chemical reaction, respectively.

The Langmuir type of adsorption is adopted for illustrating the adsorption process:

$$r_{ads,i} = \rho_s(1 - n) \cdot \frac{\partial\left(\frac{K_{L,i}c_{ads,\max,i}c_i}{1 + K_{L,i}c_i}\right)}{\partial c_i} \tag{5}$$
$$- \frac{K_{L,i}c_{ads,\max,i}c_i}{1 + K_{L,i}c_i} \cdot \rho_s \frac{\partial n}{\partial t}$$

where $\rho_s$ (kg·m$^{-3}$) is the density of solid particles, $K_{L,i}$ (m$^3$·mol$^{-1}$) is the Langmuir constant, $c_{asd,max,i}$ (mol·kg$^{-1}$) is the constant for the maximum adsorption.

The effective dispersion tensor is built from the dispersivities through the following form:

$$D_{dxx} = \alpha_l \frac{v_x^2}{|v_w|} + \alpha_t \frac{(v_y^2 + v_z^2)}{|v_w|}, D_{dxy} = D_{dyx} = (\alpha_l - \alpha_t)\frac{v_x v_y}{|v_w|}$$
$$D_{dxx} = \alpha_l \frac{v_x^2}{|v_w|} + \alpha_t \frac{(v_y^2 + v_z^2)}{|v_w|}, D_{dxy} = D_{dyx} = (\alpha_l - \alpha_t)\frac{v_x v_y}{|v_w|}$$
$$D_{dyy} = \alpha_l \frac{v_y^2}{|v_w|} + \alpha_t \frac{(v_x^2 + v_z^2)}{|v_w|}, D_{dxz} = D_{dzx} = (\alpha_l - \alpha_t)\frac{v_x v_z}{|v_w|} \tag{6}$$

The components of the velocity field $v_w$ (m·s$^{-1}$) in the $x$, $y$, and $z$ directions correspond to the fluid velocities $v_x$ (m·s$^{-1}$), $v_y$ (m·s$^{-1}$), and $v_z$ (m·s$^{-1}$), respectively. The longitudinal and transverse dispersivities are represented by $\alpha_l$ (m) and $\alpha_t$ (m), respectively.

In the trapping area, the copper ions are assumed to be collected as a solid and adhere to the surface of the porous media. And the Monod type equation is applied to describe the global precipitation process. The accumulation of precipitates containing copper elements occupies the void space of the porous material, thereby changing the porosity of the trapping area. The change of porosity due to precipitation is calculated in the following formula:

$$\frac{\partial n_p}{\partial t} = (r_{eq,i} + r_{kin,i}) \cdot V_{m,i} = c_o \frac{c_i}{K_M + c_i} \cdot V_{m,i} \qquad (7)$$

In addition, the change of porosity due to adsorption is calculated through:

$$\frac{\partial n_{ads}}{\partial t} = r_{ads,i} \cdot V_{m,i} \qquad (8)$$

And therefore, the total porosity $n$ is obtained from the equation:

$$n = n_0 - n_p - n_{ads} \qquad (9)$$

where $n_p$ (-) and $n_{ads}$ (-) are the porosity occupied by the precipitation and adsorption, respectively. $V_{m,i}$ (m³·mol⁻¹) is the molar volume, $K_m$ (mol/m³) is the constant parameter in Monod equation, $c_0$ (mol·m⁻³) is the inflow concentration.

**CASE STUDY ON THE ASPIRE CONCEPT**

A numerical case study is provided in this section to preliminary test the long-term application capacity of the ASPIRE concept in trapping copper ions from contaminated water under a real condition. In addition, the model is discretized and solved by COMSOL Multiphysics 6.2 through the PDE interfaces.

*Geometry size and mesh*
A 10 m × 10 m × 5 m porous trapping area (eg. permeable reactive barrier, reactive soil) is used for the simulation. Copper ion-rich contaminated water is injected from the top surface at a constant velocity of 5 E-6 m·s⁻¹ and flows out through 0.2 m diameter pipes installed at 1 m intervals at the bottom. All other parts of the geometry are sealed. The geometry size and its related mesh are illustrated in Fig 1.
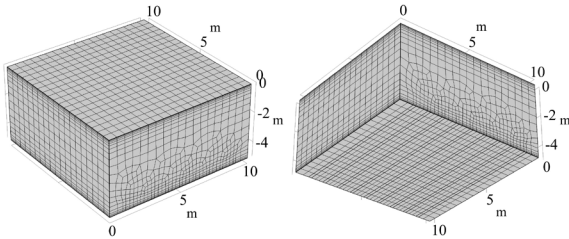


Fig 1. Geometry and mesh of the trapping area from different viewing angles.

*Boundary conditions and constant parameters*
The inflow wastewater at the top of the trapping area is characterized as follows:

$$-\vec{n} \cdot \rho_w v_w = \rho_w v_0 \qquad (10)$$

The wastewater flowing out through the pipes is represented by setting the suction at the boundary to zero, as the pipes are in direct contact with the atmospheric air:

$$s = 0 \qquad (11)$$

The copper ions flow along with the wastewater through the top surface, as described by the following expression:

$$\vec{n} \cdot (v_w c_i - (D_{d,i} + D_{e,i}) \nabla c_i) = \vec{n} \cdot v_w c_0 \qquad (12)$$

The copper ion is forbidden to diffuse and disperse on the sealed boundary:

$$-\vec{n} \cdot (-(D_{d,i} + D_{e,i}) \nabla c_i) = 0 \qquad (13)$$

where $v_0$ (m·s⁻¹) is the inflow velocity of the contaminated water.

Furthermore, the constant parameters employed in this numerical study are summarized and presented in Table 1.

| $\rho_s$ | $\kappa$ | $n_c$ | $K_m$ |
|---|---|---|---|
| 2620[5] kg/m³ | 1E-12[6] m² | 0.389 | 0.012 mol/m³ |
| $V_{m,i}$ | $c_0$ | $v_0$ | $\mu_w$ |
| 1E-4 m³/ mol | 3.1476 mol/m³ | 5E-6 m/s | 1E-3 Pa·s |

Table 1. Constant parameters for numerical simulation

*Simulation results*
As the copper precipitates continuously accumulate in the trapping area, the occupied pore space may hinder wastewater flow and subsequently lead to clogging. Consequently, the simulation is terminated when the porosity of the porous media falls below 0.1. This section illustrates the geochemical characteristics of the trapping area at 365 days.
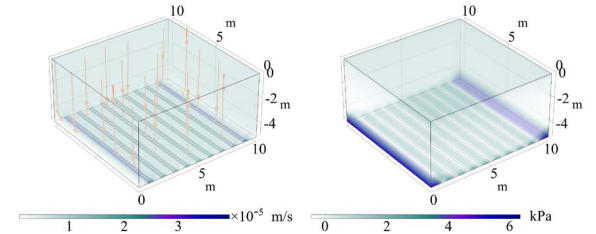


Fig 2. Velocity (left) and pressure (right) distributions in trapping area at 365 days.

Fig. 2 shows the velocity and pressure distributions in the trapping area after 365 days. The wastewater flows from the top surface of the trapping system with a velocity close to the injected velocity of 5 × 10-6 m/s (as shown by the orange lines). The outflow velocity from the pipes installed at the bottom is higher than that inside the trapping area due to the pressure difference between the trapping area and the surrounding atmosphere. Moreover, the outflow wastewater near the vertical surrounding walls exhibits the highest velocity, which is caused by higher wastewater pressure resulting from the effects of gravity and the sealed boundary condition. Additionally, since higher wastewater pressure may lead to mechanical damage and fractures, attention should be paid to the interval areas of the installed pipes and the regions near the sealed walls that experience higher wastewater pressure, as these areas require stronger structural integrity to maintain the normal and safe operation of the system.

Fig 3. Copper ion concentration (left) and porosity (right) distributions in trapping area at 365 days.

Fig. 3 illustrates the concentration distributions of the copper ions in the trapping area as well as the potential clogging due to copper particulate precipitation. The figure shows that the copper ion concentration decreases with increasing depth. Furthermore, after 365 days of operation, the copper ions initially injected from the top surface have reached an area with a depth of approximately 2 m. As physical adsorption an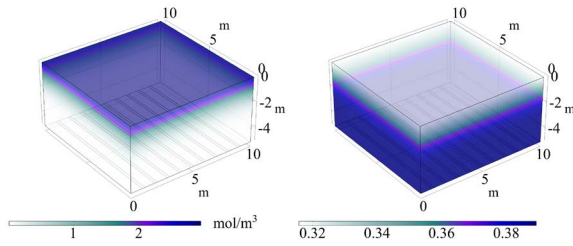d chemical reactions continuously occur along with the flow of copper ions, the void pore volume is occupied by the precipitated copper particulates, leading to a decrease in the porosity of the trapping system as the depth increases. Specifically, the porosity at the top decreases by 17% from the initial value of 0.389 to around 0.32, indicating that after one year of operation, the system is not seriously affected by clogging problems. However, clogging issues should be monitored over time to ensure proper system operation.
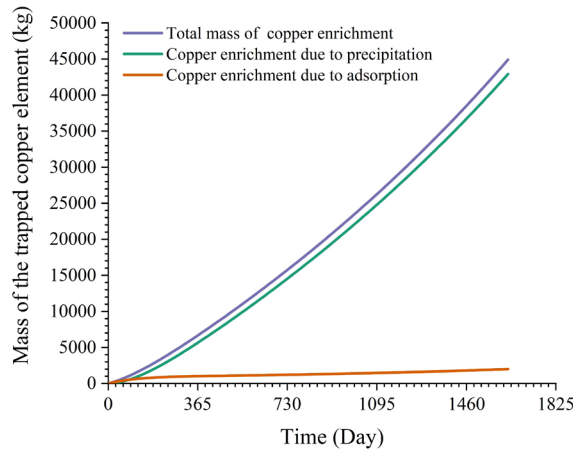


Fig 4. Mass of the trapped copper element according to time.

Fig. 4 demonstrates that both adsorption and precipitation contribute to the total copper enrichment, with adsorption initially being the dominant mechanism. However, as time progresses, precipitation becomes increasingly significant. The total mass of copper enrichment reaches approximately 45,000 kg by the end of the nearly 5-year period, highlighting the system's effectiveness in capturing and accumulating copper elements from contaminated water.

## CONCLUSIONS

The numerical case study presented in this paper demonstrates the potential of the ASPIRE concept for the long-term trapping of copper ions from contaminated water under realistic conditions. The simulation results highlight the effectiveness of the system in capturing and accumulating copper elements over a nearly 5-year period, with a total mass of copper enrichment reaching approximately 45,000 kg for a trapping zone with the dimension of 10 m in length, 10 m in width, and 5 m in depth. The study also reveals the interplay between adsorption and precipitation mechanisms, with adsorption initially dominating and precipitation becoming increasingly significant over time. Furthermore, the analysis of velocity, pressure, copper ion concentration, and porosity distributions provides valuable insights into the system's performance and potential challenges, such as clogging and structural integrity requirements. These findings underscore the importance of monitoring and maintenance to ensure the proper operation of the ASPIRE system. Overall, this numerical investigation supports the feasibility of the ASPIRE concept as a promising approach for the simultaneous remediation of contaminated water and the recovery of valuable resources, aligning with the principles of a circular economy.

It is important to note that the results of this study are based on numerical simulations, and the constant parameters and boundary conditions employed in this investigation require further experimental validation. Moreover, additional research and field-scale implementations are necessary to confirm the effectiveness of the ASPIRE concept and optimize its design for a wide range of environmental conditions and contaminants.

*Conflicts of Interest*
*The authors declare no conflict of interest.*

**REFERENCES**

[1]. D. J. Sapsford *et al*., 'Circular economy landfills for temporary storage and treatment of mineral-rich wastes', *Proceedings of the Institution of Civil Engineers - Waste and Resource Management*, vol. 176, no. 2, pp. 77–93, Apr. 2023.
doi.org/10.1680/jwarm.22.00008

[2]. P. Srivastava, S. A. Al-Obaidi, G. Webster, A. J. Weightman, and D. J. Sapsford, 'Towards passive bioremediation of dye-bearing effluents using hydrous ferric oxide wastes: Mechanisms, products and microbiology', *Journal of Environmental Management*, vol. 317, p. 115332, Sep. 2022.
doi.org/10.1016/j.jenvman.2022.115332

[3]. A. Mohammad, D. Sapsford, M. Harbottle, P. Cleall, D. Stewart, F. Sepulveda, 'Effect of Different Physical and Geochemical Parameters on Mobilisation of Metals: A Crucial Step Towards Resource Recovery from Waste', *ISSMGE*, Jul. 2022.
doi.org/10.53243/ICEG2023-314

[4]. P. J. Cleall, S. C. Seetharam, and H. R. Thomas, 'Inclusion of Some Aspects of Chemical Behavior of Unsaturated Soil in Thermo/Hydro/Chemical/ Mechanical Models. I: Model Development', *J. Eng. Mech.*, vol. 133, no. 3, pp. 338–347, Mar. 2007.
doi.org/10.1061/(ASCE)0733-9399(2007)133:3(338)

[5]. X. Zhang and H. Nowamooz, 'Chemo-thermo-hydro-mechanical behavior of a cement-stabilized rammed earth wall in interaction with the environment and underground soil', *Engineering Structures*, vol. 293, p. 116638, Oct. 2023.
doi.org/10.1016/j.engstruct.2023.116638

[6]. F. Tang and H. Nowamooz, 'Factors influencing the performance of shallow Borehole Heat Exchanger', *Energy Conversion and Management*, vol. 181, pp. 571–583, Feb. 2019.
doi.org/10.1016/j.enconman.2018.12.044

Negus R
*Cardiff University*
*School of Engineering*

Novelli V
*Cardiff University*
*School of Engineering*

Bertolesi E
*Cardiff University*
*School of Engineering*

Cashell K
*University College London*
*Department of Civil, Environmental*
*and Geomatic Engineering*

COMPUTATIONAL MODELLING AND DIGITAL TWINS

# Investigation into the Accumulated Fatigue Damage in Riveted Connections in Steel Bridges using Advanced Numerical Techniques

Fatigue in traditional riveted steel bridges is being observed at increasing frequency due to an increase in both the volume and mass of expected traffic. The financial ramifications of retrofitting, repairing and insuring bridges from this damage is vast, and many rail networks suffer from inadequate funding to address these issues. In the financial year 2019-2020 it was estimated that the cost of maintenance on the British rail network was £1.488 billion, and arguments for safety and sustainability can also be emphasised because of this form of damage. With comparable increases in volume and frequency of rail traffic, it is not inconceivable to see comparable damage occurring in contemporary infrastructure soon. This paper investigates the validity of using traditional numerical techniques to model a complex system of rivets and structural members, with the future aim of utilising the more advanced eXtended Finite Element Method (XFEM) to analyse the mechanism behind fatigue propagation in the riveted connections of steel rail bridges, addressing the effect of loading conditions and rivet geometry on crack nucleation, propagation, and failure.

Investigation into the Accumulated Fatigue Damage in Riveted Connections in Steel Bridges Using Advanced Numerical Techniques

15

## INTRODUCTION

Most traditional rail bridges in the UK, Europe, and America were constructed from a system of riveted wrought-iron girders and perpendicular stringers over 100 years ago [1][2]. The loading conditions on these structures has acutely increased in both frequency and magnitude since their initial construction, with demands from both freight and passengers rising. In recent years, it has been observed that these increasing loads have caused accelerated fatigue deterioration in the riveted sites, causing cracking and weakening of key intersections.

The primary focus of this project will look at the loading conditions for these bridges and use advanced numerical techniques to model the mechanism of fatigue nucleation occurring within the riveted points at the primary connection sites. These connections will be modelled in ABAQUS using the eXtended Finite Element Method (XFEM), with an emphasis on analysing the specific geometry of the rivet holes at the connection sites.

This paper presents the initial results from numerical modelling of static loading criteria of a complex system of rivets and structural elements that make up a crossbeam of the Quisi Bridge, constructed in Spain in 1915 (Fig. 1). Due to the non-standardised construction methods employed prior to 1940, unknown factors such as coefficient of friction, clamping force, and pre-stress effect are considered [3]. The approach is validated using strain gauge data from a crossbeam of the Quisi bridge subject from previous studies [4].
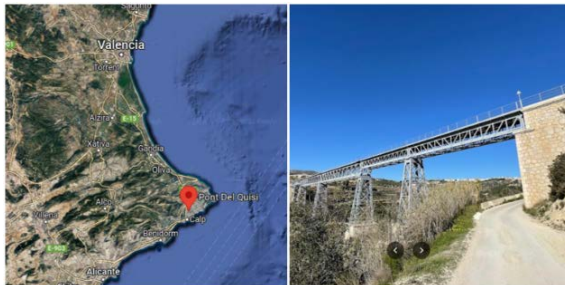


Fig 1. Location and view of the Quisi Bridge, the focus of this work.

## MATERIALS AND METHODS

*Fatigue*
Fatigue is understood to occur through crack nucleation and propagation caused by cyclical loading at a point of localised high stress. At regions of high stress, localised plastic strain occurs in metal grains causing dislocations in atomic arrangement, allowing crystal planes to slide over one another (known as a slip plane). Crystal planes tend to be formed parallel to one another, and the shear stress of one slip plane moving drags others with it, resulting in "slip bands". Continuous cyclic stresses cause these slip bands to slide back and forth, resulting in extrusions and intrusions at the grain boundary. These anomalies result in micro-crack nucleation (known as Stage I crack growth), and it is at these points where cracks begin. Micro-cracks will slowly propagate through a series of grains, until the micro-crack is large enough that a tensile plastic stress zone forms around the tip. Once the crack is large enough, the global tensile stresses dominate and force the crack to open, travelling perpendicular to this applied stress (known as Stage II crack growth). For this reason, tensile forces are far more dominant in fatigue performance of metals than compressive forces.

Fatigue can generally be characterised as high cycle fatigue (HCF), low cycle fatigue (LCF), or a combination of the two. LCF is characterised by micro0plastic damage in the stress cycle, typically greater than the endurance limit of the material (where cracks develop), coupled with low frequency [5][6]. LCF is also notably predominant in geometric features such as holes and sharp changes, such as notches, and as such, is the representative loading case in railway structures.

*FEM and XFEM*
The finite element method is a numerical tool that can be traced back to the 1940s when Hrennikoff proposed using a series of rods and beams to approximate a stress solution in continuous solids. Development of more sophisticated computers led to more complex matrices being solved, resulting in the advent of the stiffness matrix in the 1950s. For both implicit and explicit approaches in FEA, the analysis is ultimately aiming to solve a series of displacements arising from disturbances applied to the finite element mesh from a boundary-value problem. In either case, the solver will approximate a solution for the global displacement vector in three dimensions. The fundamental equations for solving for displacement using implicit and explicit solvers are given in Eq. 1 and Eq. 2. In Eq. 1, $K$ and $F$ represent the stiffness matrix and force vector, while in Eq. 2, $N$ represents the individual node degree of freedom, $i$ the relevant increment, and $t$ the time step.

$$[K][u] = [F] \tag{1}$$

$$u^N_{(i+1)} = u^N_{(i)} + \Delta t_{i+1} \dot{u}^N_{(i+\frac{1}{2})} \tag{2}$$

In both cases, the displacement vector or matrix, $u$ is clearly independent. Melenk introduced the concept of enriching the vector, $u$ through the partition of unity [7], modifying the element that the crack occupies by introducing enrichment functions to estimate a solution to where the crack will propagate. In 1999, Ted Belytschko expanded upon this principle to accommodate the development of discontinuities within the finite element mesh [8].

Proper description of discontinuities is difficult and is generally defined as either a strong or weak discontinuity in the FE mesh [9]. Strong discontinuities tend to arise when there are discontinuities in the solution variables due to large displacement jumps, such as cracks and holes, whereas weak discontinuities occur due to discontinuities in the derivatives of the solution variables, resulting in strain differences, often caused by variation in material properties.

Enriched nodes are generally defined by the user with some degree of knowledge about the approximate location that a crack will develop, but the nucleation point does not have to be explicitly defined. Pre-defining the enriched crack "zone" is necessary to reduce computational time and resources.

As previously discussed, the fundamental principle behind the XFEM method is the enrichment of the displacement vector alone. Currently, Abaqus only provides capability to conduct XFEM analysis in an implicit environment. Whereas explicit solvers primarily converge on a solution which aims to solve for the acceleration of nodes and thus calculate the displacement vector from a given time-step (referring to Eq. 2), the convergence of an implicit solver is not time dependent and therefore is unconditionally stable. As seen in Eq. 3, the XFEM approach is not time-dependant, and

therefore cannot be used in explicit analyses. Unfortunately, this means that for more complex structural issues with large geometries, simulations can be very inefficient due to the generation of the stiffness matrix. It should also be noted, therefore, that within the XFEM approach for modelling crack growth, it is implied that it is a "static" crack growth and therefore time-independent, making it ideal to simulate slow crack progression in low-cycle fatigue, independent of simulating an actual cyclic load.

*Preliminary numerical modelling*
Due to the limited background research on combining the XFEM approach with other FEM techniques on a large structural example, the first stage of validating the numerical approach is to measure the response of the numerical model of a beam section under simplified static loading conditions via a traditional FEM approach and compare the response to strain gauge data previously acquired from experimental studies (Fig. 2). The static response is compared to the pre-damage strain results (roughly <10,000 load cycles), acquired from strain gauges – SG$N$ – mounted on the crossbeam (Fig. 3).
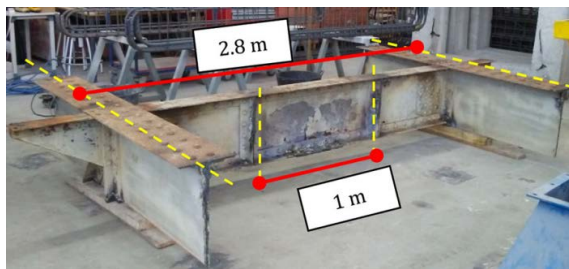


Fig. 2. Original bridge geometry of Ponte del Quisi crossbeam.
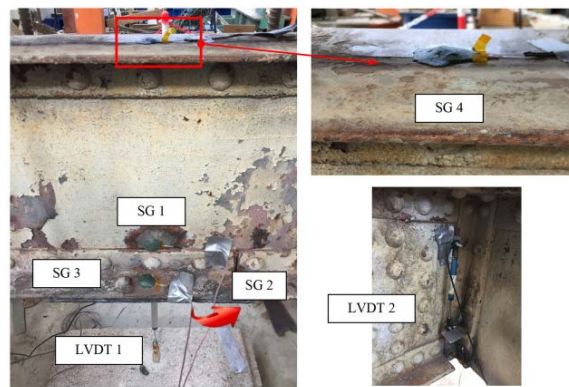


Fig. 3. Crossbeam strain gauge locations.

The geometry of the crossbeam is replicated in Solidworks/AutoCAD and exported to Abaqus. Symmetry is exploited to improve the efficiency of the simulation. The pre-process geometry, loading, and strain gauge locations are shown in Fig. 4.

The material and interaction properties are evaluated by comparing the strain results, and in addition to this, a mesh sensitivity study is carried out to ensure efficiency of the numerical model.
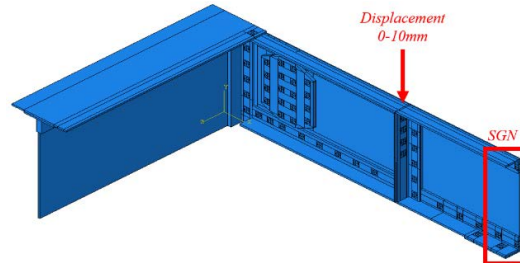


Fig. 4. Pre-process geometry of Quisi bridge.

As the model consists of many independent parts, contact interaction must be modelled to ensure realistic behaviour is captured during analysis. The coefficient of friction, $v$, plays a key role in the interaction between parts. It is simply defined as the relationship between the normal and reaction forces when an object moves along a surface The friction coefficient varies dramatically for given loading criteria. Due to the difficulty in determining clamping force, the normal force, $R$, cannot be directly determined, and therefore neither can the frictional force, $F$. In addition to this, the effect of material degradation on both the friction coefficient and chemical cohesiveness is difficult to determine without extensive testing. Due to the unknown characteristic of the friction of the structural steel, a range of friction coefficients from 0.14–0.74 [10], were considered for steel-on-steel friction behaviour, representing a variety of conditions from dry and clean to heavily corroded. A value for $v$ of 0.00 was also considered to act as a control and observe whether the effect of the friction coefficient is significant.

The loading conditions are simulated by applying a simple step displacement at the point where loading from railway traffic is expected to occur via a railway track; based on the loading criteria defined in the experimental study.

Investigation into the Accumulated Fatigue Damage in
Riveted Connections in Steel Bridges Using Advanced
Numerical Techniques

17

## RESULTS

*Preliminary strain results*
The strain response for a range of friction coefficients at an element size of 5mm is presented in Fig. 5.
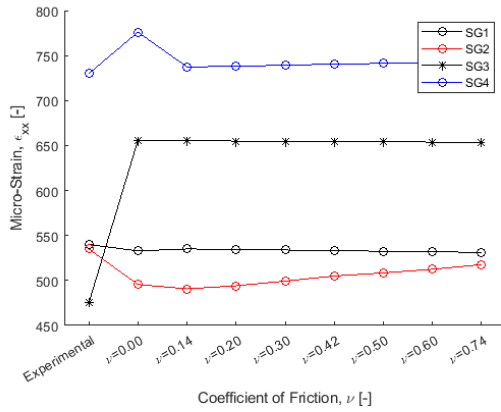


Fig. 5. Strain results using an element size of 5.

*Mesh sensitivity study*
Due to the size and implementation of interaction criteria, it was necessary to maximise the size of meshed elements to reduce computational time – for example, simulation run time for an approximate global element size of 5mm is roughly one hour – while maintaining accuracy of numerical results. For this purpose, a sensitivity study for elements of the following approximate global sizes was carried out (Table 1) and compared with the experimental data. Figure 6 shows the comparison between computational time required, and the percentage deviation for each strain gauge for different element sizes, using a value of v of 0.74.



Fig. 6. Mesh sensitivity study results.

## DISCUSSION

This paper presents the initial numerical work carried out investigating the response of the crossbeam, including the evaluation of the mesh. The initial results are encouraging, and using the proposed interaction and material criteria yield results within 5% deviation for all element sizes for SG1 and SG4. At a more refined mesh, the accuracy of SG2 is also within satisfactory levels of accuracy. The strain results tend to be most accurate for a higher friction coefficient, which is likely caused by high levels of steel corrosion.

The results for SG3, however, deviate significantly from the experimental results no matter the context. On the original crossbeam, SG3 is mounted on a lower plate where fatigue is seen to occur in previous experimental studies. The reduced clamping, potentially from plastic deformation in the rivet, means that in a practical scenario, the plates in the crossbeam are likely to undergo a small amount of slip, reducing the actual strain. As it is around these rivets where the maximum tensile stress and fatigue onset occurs, these potential causes will require further in-depth investigation.

A major factor to consider is the computational time required to run the simulations. A mesh sensitivity study has already been carried out, noting the computational time required, and from Fig. 5, it is possible to infer an inverse exponential relationship between the element size and computational effort. Looking ahead, the XFEM process typically requires a highly refined mesh to perform accurate analysis; if a coarse mesh can be used to accurately simulate the static response of the beam, it is proposed to use a simplified global model with a refined mesh where fatigue is expected.

### Conflicts of Interest
*The authors declare no conflict of interest.*

| Strain gauge | Experimental | Es | | | | | |
| --- | --- | --- | --- | --- | --- | --- | --- |
| | | 15 | 12.5 | 10 | 7.5 | 5 | 3 |
| SG1 | 540.00 | 528.57 | 533.49 | 541.13 | 541.13 | 535.90 | 520.77 |
| SG2 | 535.00 | 462.45 | 442.65 | 432.76 | 432.76 | 538.47 | 517.34 |
| SG3 | 475.00 | 640.97 | 652.51 | 658.61 | 666.94 | 653.12 | 629.47 |
| SG4 | 730.00 | 745.33 | 744.96 | 740.29 | 748.51 | 765.25 | 750.40 |

Table 1. Mesh sensitivity results.

**REFERENCES**

[1]   B. M. Imam and T. D. Righiniotis, 'Fatigue evaluation of riveted railway bridges through global and local analysis', *Journal of Constructional Steel Research*, vol. 66, no. 11, pp. 1411–1421, Nov. 2010. doi.org/10.1016/j.jcsr.2010.04.015

[2]   A. L. L. Silva *et al.*, 'Fatigue strength assessment of riveted details in railway metallic bridges', *Engineering Failure Analysis*, vol. 121, p. 105120, Mar. 2021. doi.org/10.1016/j.engfailanal.2020.105120

[3]   A. Pipinato, M. Molinari, C. Pellegrino, O. S. Bursi, and C. Modena, 'Fatigue tests on riveted steel elements taken from a railway bridge', *Structure and Infrastructure Engineering*, vol. 7, no. 12, pp. 907–920, Dec. 2011. doi.org/10.1080/15732470903099776

[4]   E. Bertolesi, M. Buitrago, J. M. Adam, and P. A. Calderón, 'Fatigue assessment of steel riveted railway bridges: Full-scale tests and analytical approach', *Journal of Constructional Steel Research*, vol. 182, p. 106664, Jul. 2021. doi.org/10.1016/j.jcsr.2021.106664

[5]   B. K. Parida, 'Fatigue Testing', in *Encyclopedia of Materials: Science and Technology*, Elsevier, 2001, pp. 2994–2999. doi.org/10.1016/B0-08-043152-6/00533-7

[6]   H. Farhat, *Operation, Maintenance, and Repair of Land-Based Gas Turbines*, S.L.: Elsevier, 2021.

[7]   J. M. Melenk and I. Babuška, 'The partition of unity finite element method: Basic theory and applications', *Computer Methods in Applied Mechanics and Engineering*, vol. 139, no. 1–4, pp. 289–314, Dec. 1996. doi.org/10.1016/S0045-7825(96)01087-0

[8]   N. Moes, J. Dolbow, and T. Belytschko, 'A finite element method for crack growth without remeshing', *International Journal for Numerical Methods in Engineering*, vol. 46, no. 1, pp. 131–150, Sep. 1999. doi.org/10.1002/(SICI)1097-0207(19990910)46:1<131::AID-NME726>3.0.CO;2-J

[9]   J. Ding, T. Yu, and T. Q. Bui, 'Modeling strong/weak discontinuities by local mesh refinement variable-node XFEM with object-oriented implementation', *Theoretical and Applied Fracture Mechanics*, vol. 106, p. 102434, Apr. 2020. doi.org/10.1016/j.tafmec.2019.102434

[10]  H. A. Rothbart and T.H. Brown, *Mechanical Design Handbook*, 2nd ed. New York: Mcgraw-Hill, 2006.

Warren F

*Cardiff University*
*School of Medicine*

Spezi E

*Cardiff University*
*School of Engineering*

Paisey S

*Cardiff University*
*School of Medicine*

Smith R

*Cardiff University*
*School of Medicine*

Lai Y

*Cardiff University*
*School of Computer Science*
*and Informatics*

AI AND DEEP LEARNING

# The Use of Mutual Information and Entropy as an Acquisition Function to be Used in Active Learning

This work has explored the theoretical principles of Mutual Information and Entropy and their use as combined acquisition score. The work looked at mutual information and entropy combined score values produced from a deep learning model trained to segment preclinical CT scans, which supported the investigation into its use in an active learning pipeline as an information metric, to guide the selection of data from the unlabelled data pool to incorporate into the training set. The work has shown that the combined acquisition function shows promise. Further refinement and validation are necessary to fully establish its utility in active learning tasks.

## INTRODUCTION

Medical image segmentation is a fundamental and necessary task performed when analysing CT images. Deep learning has been shown to be useful in medical image segmentation. However, it faces issues including the requirement of large amounts of labelled data to act as the ground truth reference during training. Obtaining annotated data by experts is an expensive and time-consuming task [1]. An approach used to reduce the need for large amounts of annotated data is Active Learning (AL) [2].

The goal of AL is to select the most valuable and informative data from an unlabelled data pool to be labelled and added to the training set, to minimize the overall amount of data needed to be labelled. In AL, instead of labelling a large dataset, it iteratively acquires labels from an expert only for the most informative or uncertain data points from a unlabelled data pool. Following each acquisition step, the recently labelled data points are incorporated into the training set, and the model undergoes retraining. This iterative procedure continues until a satisfactory level of accuracy is attained [3].

In AL, the informativeness or uncertainty of new data points is assessed by an acquisition function. Acquisition functions can include entropy, least confident, margin and density-based sampling [4]. Effective metrics are essential for guiding the selection of informative samples. It is the most crucial component and the primary distinguishing factor among AL methods in the literature.

The main aim of this work is to present a base model trained on a minimal dataset that can be used for preclinical segmentation and utilise the model to show how an information metric, along with an uncertainty metric, can be used in AL as an acquisition function to guide the selection of data to incorporate into the training set.

## MATERIALS AND METHODS

*Deep Learning Model*
The dataset used to train the base model was obtained from the Positron Emission Tomography Imaging Centre (PETIC). The data consisted of 76 preclinical CT scans of mice, all with corresponding ground truths with 6 labels corresponding to background, skeleton, liver, kidney, left tumour and right tumour. The ground truths were manually outlined by an expert user from PETIC. 20 randomly selected scans including their ground truths were used in a 80:20 split for training, where 16 samples were used for the initial training and 4 samples were used for testing. The remaining 56 scans created the unlabelled data pool. Additional preprocessing of the dataset was performed including resampling and resizing the scans to make the dimensions coincide together.

The base model was developed to predict the segmentation masks of the data utilizing NiftyNet open-source platform [5]. For the network architecture, a dense VNet was used with an initial learning rate of 0.001 along with the Adaptive Moment estimation (Adam) optimiser. The model was trained on the training set for 3000 iterations on whole images. Following training inference was performed on the test scans within the testing set to produce predicted segmentations and on the unlabelled data pool to produce the predicted segmentation and the probability masks.

The metric employed to evaluate the performance of the model and thus segmentation was the Dice Score Coefficient (DSC). The DSC shows the similarity between the predicted segmentation and the ground truth by measuring the overlap and is calculated using Eq. 1.

$$DSC = \frac{2 \times |GT \cap SM|}{|GT| + |SM|} \tag{1}$$

Where GT is the ground truth mask and SM is the segmented predicted mask. $| GT \cap SM |$ is the number of pixels common to both the segmented predicted mask and the ground truth mask. $|GT|$ is the total number of pixels in the ground truth mask and $|SM|$ is the total number of pixels in the segmented predicted mask [6]. A DSC of 0.7 and above is considered to have good overlap [7].

*Active Learning Acquisition Function*
Two acquisition functions were combined to create one final score, which is applied following inference of the unannotated pool. The final score consists of the uncertainty function which calculates the uncertainty associated with the prediction of the model for image $x$. The entropy is used as the measure of predictive uncertainty. The entropy (H) of an image $x$ for a n-class task is defined in Eq. 2.

$$H(x) = -\sum_{i-1}^{n} P(y_i|x) \log\big(P(y_i|x)\big) \tag{2}$$

$P(y_i \backslash x)$ is the probability that the current sample $x$ is predicated to be of class $y_i$. A higher entropy corresponds to a higher uncertainty, thus suggesting lower overall confidence [8].

The second part of the acquisition function is the Mutual Information (MI). In general, MI evaluates the degrees of relatedness between two variables [9]. In terms of images calculates the similarity between two images. MI of two random variables A and B is defined by Eq. 3.

$$I(A,B) = \sum_{a,b} P_{A,B}(a,b) \log \frac{P_{A,B}(a,b)}{P_A(a)P_B(b)} \tag{3}$$

Where $P_A(a)$ and $P_B(b)$ are the marginal probability functions and $P_{A,B}(a,b)$ is the joint probability function. MI measures the degree of dependence of A and B by measuring the distance between the joint probability and the probability associated with the case of complete independence [10]. The MI is 0 if the two variables are independent, meaning there is no relationship between them and if the two variables are dependent MI is greater than 0 [11].

The MI is normalised to produce the normalised mutual information (NMI) using Eq. 4 proposed by [12].

$$\tilde{I}(A,B) = \frac{H(A) + H(B)}{H(A,B)} \tag{4}$$

Where $H(A)$ is the entropy of $A$ and $H(B)$ is the entropy of $B$ and $H(A,B)$ is the joint entropy of $A$ and $B$.

The final scoring function is calculated by combining MI and entropy and can be expressed as Eq. 5.

$$Score(x) = \alpha \cdot Uncertainty(x) - \beta \cdot MI(x, X_{train}) \tag{5}$$

$MI(x, X_{train})$ represents the NMI between the image from the unannotated data pool and the training dataset and the $Uncertainty(x)$ represents the uncertainty with the model's prediction of the segmentation for image $x$ from the unannotated data pool.

The terms are weighted by coefficients and that control the contribution of uncertainty and NMI to the overall score. By adjusting these coefficients, one aspect can be prioritised over the other based on the specific requirements of the learning task.

The images with the highest combined score would be selected. These images represent those with a high entropy which indicates high uncertainty meaning the model has lower confidence in the correct label for that image and low MI meaning they contain information that the current training set doesn't contain.

*Implementation*
The DSC was calculated for each label in the predicted segmentation of the test images and the average taken across them.

The NMI was calculated on a label basis, by making comparisons of histograms of CT intensity values in the training set versus the unannotated data pool. The background label was ignored, to focus on the relevant regions of interest as background can introduce noise and unnecessary complexity. Each image within the unannotated pool has 16 values for each label and the average is taken per label. The overall average NMI value is the taken per image and these were normalised for the set.

To calculate the entropy of each image in the unannotated data pool, the predicted segmentations are used and the entropy is calculated for each pixel and the average is taken across the image. These were then normalised for the set.

The two calculations were combined as shown in Eq. 45 to provide a final score for each image in the unannotated data pool. To demonstrate the effectiveness of the combined acquisition score the DSC is used, as a low DSC indicates poor segmentation performance, suggesting that the sample is informative and should be added to the training pool. If the combined acquisition function consistently identifies samples with low DSC, it indicates that the combined function is effectively selecting the most informative samples.

**RESULTS**

The predicted segmentations were analysed using the DSC for each label in the test images and the average taken across them as shown in Table.1 Test image 4 had no left tumour present.

| | Labels | | | | | | |
|---|---|---|---|---|---|---|---|
| Test Image | 0 | 1 | 2 | 3 | 4 | 5 | Average |
| 1 | 1.0 | 0.9 | 0.7 | 0.6 | 0.4 | 0.5 | 0.7 |
| 2 | 1.0 | 0.8 | 0.6 | 0.6 | 0.6 | 0.5 | 0.7 |
| 3 | 1.0 | 0.9 | 0.5 | 0.7 | 0.7 | 0.6 | 0.7 |
| 4 | 1.0 | 0.9 | 0.5 | 0.8 | N/A | 0.4 | 0.7 |

Table 1. Dice coefficient score for test images.

The images within the unannotated data pool are labelled 0-56 for display purposes and ease, where each number refers to a different image.

The average NMI and the average entropy per image were combined and the values are demonstrated in the bar chart in Fig. 1. The bar chart is ordered from lowest to highest where each bar represents a different image and the height of the bar represents the combined score consisting of entropy and NMI for that image. Within the graph, a line has been drawn, where the line acts as a cut-off point. All data to the right of the bar represent images that would be sent to the oracle for annotation as they represent images with both high entropy (indicating high uncertainty) and low mutual information (indicating information not present in the current training set) and all data to the right of the bar would not be annotated.
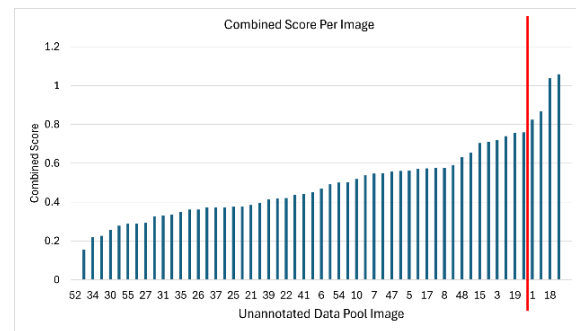


Fig. 1. Combined score per image of the image in the unannotated data pool.

The DSC were calculated for each image, ignoring the background, in the unannotated data pool, where the average DSC has a value of 0.6 and ranges from 0.2 to 0.8.

Based on the analysis, the combined acquisition score exhibits a Pearson correlation coefficient of -0.25 with the DSC, reflecting a slight negative correlation as depicted in Fig. 2. The p-value obtained was 0.059.
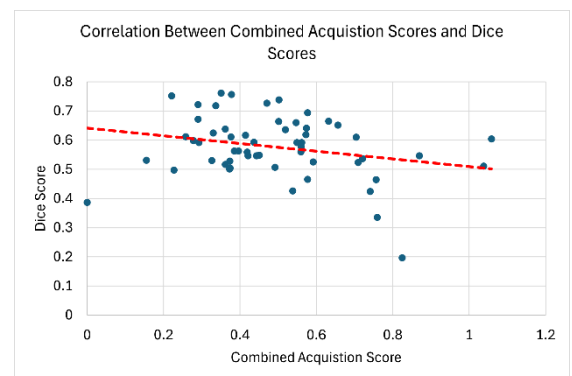


Fig. 2. Correlation plot between the combined acquisition score and the dice score.

## DISCUSSION

The dice coefficient values showed the model performed well as all test scan segmentations had an average dice score of 0.7 showing good overlap when compared to the ground truth.

The Pearson correlation coefficient of -0.25 reflects a slight negative correlation. This suggests that higher acquisition scores tend to be associated with lower DSC, indicating that the function may have a tendency, albeit modest, to select more informative samples for model enhancement.

While the p-value of 0.059 slightly exceeds the conventional significance threshold of $P<0.05$, it remains close to this boundary, hinting at a potential trend where the acquisition function targets challenging samples for labelling. This near-significant result suggests that our acquisition function may be on the cusp of demonstrable effectiveness in enhancing the active learning process. Additionally, it's important to note that the effectiveness of the acquisition function does not necessarily depend on a linear relationship. The nuanced nature of data distribution and the complexity of the learning model might mean that non-linear relationships are also of substantial value in improving model accuracy. This insight provides an encouraging direction for further refinement and potential adjustments to the acquisition strategy to better capture and utilize informative samples for improving the model performance.

**Conflicts of Interest**
*The authors declare no conflict of interest.*

## REFERENCES

[1] S. Boehringer, A. Sanaat, H. Arabi, and H. Zaidi, 'An active learning approach to train a deep learning algorithm for tumor segmentation from brain MR images', *Insights Imaging*, vol. 14, no. 1, p. 141, Aug. 2023. doi.org/10.1186/s13244-023-01487-6

[2] J. Sourati, M. Akcakaya, J. Dy, T. Leen, and D. Erdogmus, 'Classification Active Learning Based on Mutual Information', *Entropy*, vol. 18, no. 2, p. 51, Feb. 2016. doi.org/10.3390/e18020051

[3] A. Kirsch, J. van Amersfoort, and Y. Gal, 'BatchBALD: Efficient and Diverse Batch Acquisition for Deep Bayesian Active Learning', *arXiv*, 28 Oct. 2019. doi.org/10.48550/arXiv.1906.08158.

[4] S. Budd, E. C. Robinson, and B. Kainz, 'A survey on active learning and human-in-the-loop deep learning for medical image analysis', *Medical Image Analysis*, vol. 71, p. 102062, Jul. 2021. doi.org/10.1016/j.media.2021.102062

[5] E. Gibson et al., 'NiftyNet: a deep-learning platform for medical imaging', *Computer Methods and Programs in Biomedicine*, vol. 158, pp. 113–122, May 2018. doi.org/10.1016/j.cmpb.2018.01.025

[6] S. M. Sundara and R. Aarthi, 'Segmentation and Evaluation of White Blood Cells using Segmentation Algorithms', in *2019 3rd International Conference on Trends in Electronics and Informatics (ICOEI)*, Tirunelveli, India: IEEE, Apr. 2019, pp. 1143–1146. do.org/10.1109/ICOEI.2019.8862724

[7] A. P. Zijdenbos, B. M. Dawant, R. A. Margolin, and A. C. Palmer, 'Morphometric analysis of white matter lesions in MR images: method and validation', *IEEE Trans. Med. Imaging*, vol. 13, no. 4, pp. 716–724, Dec. 1994. doi.org/10.1109/42.363096

[8] P. Ren *et al.*, 'A Survey of Deep Active Learning', *ACM Comput. Surv.*, vol. 54, no. 9, pp. 1–40, Dec. 2022. doi.org/10.1145/3472291

[9] M. Noshad, J. Choi, Y. Sun, A. Hero, and I. D. Dinov, 'A data value metric for quantifying information content and utility', *J. Big Data*, vol. 8, no. 1, p. 82, Dec. 2021. doi.org/10.1186/s40537-021-00446-6

[10] H. Chen, 'Mutual Information: A Similarity Measure for Intensity Based Image Registration', in *Advanced Image Processing Techniques for Remotely Sensed Hyperspectral Data*, Berlin, Heidelberg: Springer Berlin Heidelberg, 2004, pp. 89–108. doi.org/10.1007/978-3-662-05605-9_4

[11] L. Zheng, 'Using mutual information as a cocitation similarity measure', *Scientometrics*, vol. 119, no. 3, pp. 1695–1713, Jun. 2019. doi.org/10.1007/s11192-019-03098-9

[12] D. Hill, 'Across-Modality Registration Using Intensity-Based Cost Functions', in *Handbook of Medical Image Processing and Analysis*, Elsevier, 2009, pp. 613–628. doi.org/10.1016/B978-012373904-9.50047-7

# Oyibo P

*Cardiff University*
*School of Engineering*

# Brynolfsson P

*Skåne University Hospital, Sweden*
*Department of Hematology, Oncology,*
*and Radiation Physics*

# Spezi E

*Cardiff University*
*School of Engineering*

AI AND DEEP LEARNING

# Integrating Radiomic Image Analysis in the Hero Imaging Platform

We present the integration of radiomic image analysis in the Hero Imaging platform. We created a SPAARC node on Hero Imaging Platform, which facilitates access to SPAARC's cutting-edge functionality with the visual programming simplicity of the Hero Imaging platform. Subsequently, we validated the reliability of the $SPAARC_{Hero}$ using the IBSI validation dataset of multimodal imaging (CT, F18-FDG -PET, and T1w MRI) comprising 51 patients with soft-tissue sarcoma. This validation involved evaluation of the ICC of $SPAARC_{Hero}$ and two other IBSI compliant software, MIRP and $SPAARC_{MATLAB}$ using IBSI 2 phase 3 configuration and Test cases. Out of the 486 extracted features, 462 were found to be reproducible across the three software, with lower bounds of 95% confidence intervals (CIs) of ICCs greater than 0.75. Our results verify the compliance of SPAARCHero with IBSI standard for Radiomics feature extraction.

## INTRODUCTION

Typical user interactions in medical image processing often involve utilizing command-line inputs or scripting within text editors [1]. While expert engineers and computer scientists may find it straightforward to leverage text-based coding to develop complex algorithms from a series of basic image processing steps, non-experts and clinicians may find this difficult. This challenge is evident in the field of radiomics,  a rapidly growing area of research focused on extracting quantitative metrics from medical images, known as radiomic features. These features include characteristics such as tissue and lesion heterogeneity and shape. They show potential for aiding clinical diagnosis or prognosis, either on their own or when combined with demographic, histologic, genomic, or proteomic data. [2]. Despite their potential in quantifying medical imaging characteristics, the requirement of image processing knowledge as well as the absence of standardized definitions and validated reference values has hindered their clinical utility.

Recently, a collaboration involving twenty-five research teams contributed to a significant joint effort known as the Image Biomarker Standardization Initiative (IBSI). This initiative aimed to address critical challenges within the field of radiomics, particularly focusing on the reproducibility and reliability of common radiomic features. In its initial effort, the IBSI standardized procedures for computing a comprehensive set of 169 radiomics features, facilitating the validation and calibration of various radiomics software tools [3]. Subsequently, the IBSI further defined and standardized eight convolutional

filter types intended to enhance specific structures and patterns in medical imaging. This standardization supported reproducible radiomics analyses, thereby improving consistency and reliability for more robust clinical insights [4]. The outcomes of the IBSI have significantly influenced the development of various radiomics frameworks, including LIFEx [5], Pyradiomics [6], Medical Image Radiomics Processor (MIRP) [7] and SPAARC [8].

SPAARC[1] stands for Spaarc Pipeline for Automated Analysis and Radiomics Computing. SPAARC is a rigorously tested package designed for reproducible extraction of radiomic features from both 2D and 3D image arrays [9, 10]. For radiomic features to be beneficial, they must be applied clinically, requiring an adequate level of visualization and interaction. Consequently, a substantial advancement in medical image analysis is expected if these algorithms can be smoothly integrated into clinical environments, with reasonable effort dedicated to validating their relevance, thereby ultimately enhancing healthcare.

In this work, we present and validate the integration of radiomic image analysis in the Hero Imaging Platform by developing a SPAARC node (SPAARC_Hero) which allows an easy combination of the IBSI compliant radiomic feature extraction algorithms with visualizations created by the Hero Imaging platform to facilitate ease-of-use in both clinical and research settings without the requirement of computer programming knowledge.
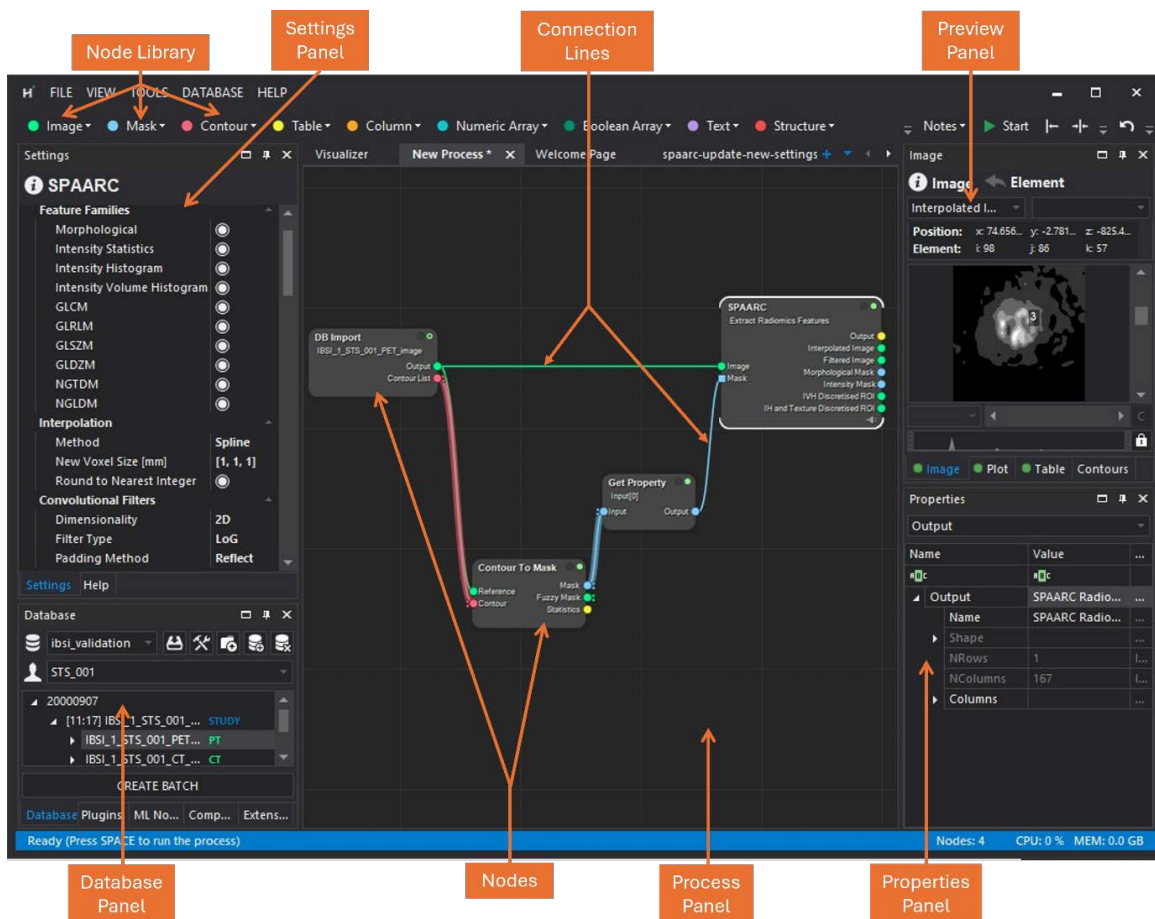
---

1          https://spaarc-radiomics.io



Fig. 1. Hero Imaging Workspace highlighting the 5 Primary panels; the Database, Process, Settings, Preview, and Properties panels.
The Process panel also contains a sample radiomics workflow with Nodes and Connection Lines.

## MATERIALS AND METHODS

*Hero Imaging Platform*

Hero Imaging platform offers an intuitive visual programming interface which simplifies advanced medical imaging workflows. The Hero Imaging workspace (shown in Fig. 1) comprises five primary panels: the Database, Process, Settings, Preview, and Properties panels. Within the Database panel, medical image databases in DICOM or NIfTI file formats are stored and retrieved. These databases are organized by patients and studies, which enables support for batch processing. Scans can be imported from the database panel into the process panel as nodes through a simple drag-and-drop interface. Additional nodes can be incorporated into the process panel from the node library or by utilizing right-click functionality within the process window. The settings panel allows for the adjustment of parameters associated with a selected node, while the preview panel facilitates the visualization of outputs, including images, plots, tables, or contours generated by the selected node. Furthermore, the properties panel provides detailed information regarding the output produced by any selected node.

Node input and output connections are color-coded for clarity: green, blue, red, and yellow signify that a node of type image, mask, contour, and table, respectively, can be connected. A white colour indicates that multiple node types can be connected. The shapes of the connections also convey information: circles represent mandatory inputs, while squares denote optional ones. Two small dots signify that a list can be connected, and outlines indicate that multiple inputs can be connected. Nodes are connected by dragging from the output of one node to the input of another and can be disconnected by double-clicking on the connection lines. Moreover, each node features a status button located in the top right corner, providing information about the node's execution when hovered upon. A green status button indicates a successful execution, while yellow denotes an encountered error during execution. A red status button signifies that the node cannot be executed.

*Hero Imaging SPAARC Node*

SPAARC is a multiplatform software that incorporates a comprehensive set of 165 standardized radiomic features and 7 convolutional filters, adhering to the guidelines established by the IBSI [3, 4]. SPAARC offers implementations in both MATLAB[2] (The Mathworks, Natick, USA) and Python[3] programming environment. However, SPAARC_Hero is specifically developed in Python, as Hero Imaging platform provides robust support for creating custom nodes to execute Python libraries, with full debugging capabilities.
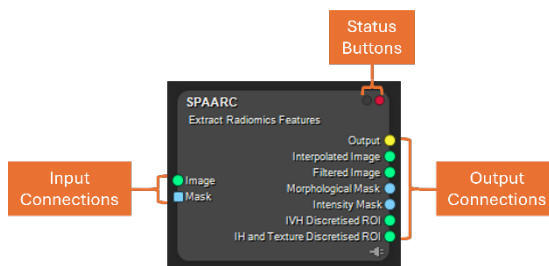


Fig. 2. SPAARC_Hero node highlighting the input connections, output connections and status button.

As shown in Fig. 2 the SPAARC_Hero node consists of 2 inputs and a max of 7 output connections. It accepts, as input, a medical image and a binary annotation mask from Hero nodes of type image and mask, respectively. The SPAARC_Hero node returns the computed radiomic features as Hero connection type table. The interpolated image, filtered image, and discretized region of interest images are returned as Hero connection type image. While morphological and intensity masks are returned as Hero connection type mask.

Configuration of SPAARC_Hero follows the IBSI configuration standard and can be adjusted in the settings panel, which is divided into sub-menus described as follows:

- Feature Families: settings for selecting families of radiomic features to extract.

- Convolutional Filtering: settings for specifying the type of convolutional filtering to apply.

- Interpolation: settings for translating image intensities from the original image grid to an interpolation grid.

- Convolutional filters: settings for configuring the properties of the IBSI-standardized convolutional filters.

- Re-segmentation: settings for defining exclusion criteria for voxels from a previously segmented ROI.

- Discretization: settings for quantizing image intensities within the ROI.

- Texture Analysis: settings for texture-based feature families.

The IBSI manuals include full detailed description of the configuration settings and functions within the Radiomic feature extraction pipeline to which SPAARC adhere [11, 12].

*IBSI Validation Dataset and Configuration*

To validate the developed SPAARC_Hero, we employed the IBSI validation dataset [4]. This dataset comprises a group of 51 patients diagnosed with soft-tissue sarcoma who underwent multimodality imaging, including co-registered computerized tomography (CT), fluorine 18 fluorodeoxyglucose (F18-FDG) positron emission tomography (PET), and T1-weighted (T1w) magnetic resonance imaging (MRI) scans. Each image in the dataset was accompanied by a segmentation of the gross tumor volume, utilized as the region of interest (ROI). For each imaging modality, nine specific Test cases were defined for image processing and convolutional filters. More details about the test cases and configurations can be found in the Benchmarking Phase 3: validation section of the IBSI 2 manual [11].

## RESULTS

An illustrative radiomic analysis workflow with SPAARC$_{Hero}$ is depicted in the process panel of Fig. 1. A total of 486 features were extracted, comprising 18 features extracted through 9 different configurations, across 3 image modalities. These features were extracted using SPAARC$_{Hero}$ as well as two other IBSI-compliant frameworks: (a) the MATLAB version of SPAARC (SPAARC$_{MATLAB}$) and MIRP, and exported to comma separated values file format (CSV) for further statistical analysis. Figure 3, shows the intraclass correlation coefficient (ICC) estimates and their 95% confidence intervals. The ICC was calculated using the Pingouin statistical package[4] version 0.5.4, based on a single rater, absolute-agreement, two-way random-effects model. The reproducibility of each feature was categorized as follows [4]: poor (lower bound less than 0.50), moderate (between 0.50 and 0.75), good (between 0.75 and 0.90), and excellent (greater than 0.90). Among the 486 features, 462 (95.06%) demonstrated good to excellent reproducibility (ICC 95% CI lower bound, >0.75). Only twelve features (2.47% of 486) were poorly reproducible (ICC 95% CI lower bound, <0.50). These features were primarily associated with Laplacian of Gaussian and, separable and non-separable wavelet filters. Specifically, coefficient of variation and quartile coefficient of dispersion features represented the majority, accounting for 4 and 7 out of the 12 poorly reproducible features, respectively.

## DISCUSSION

The integration of IBSI-compliant radiomic image analysis in the Hero Imaging platform improves the usability of SPAARC for researchers and clinicians battling cancer. The findings from our validation experiment complement the reported IBSI validation results [4], where similar features were found to be poorly reproducible. SPAARC's adherence to IBSI's standardized methodological details mitigate discrepancies in extracted features, thus enhancing reproducibility in radiomics studies. Moving forward, we aim to assess SPAARC Hero for its potential in the diagnosis, prognosis, and monitoring of cancer and other diseases.

**Conflicts of Interest**
*Patrik Brynolfsson, PhD is an employee of Hero Imaging and developer of the Hero Imaging platform.*
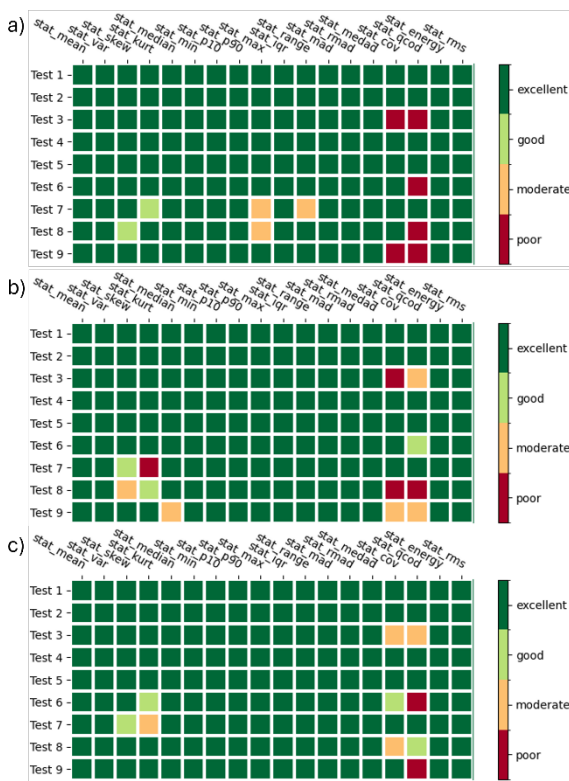


Fig. 3. Reproducibility of features extracted by SPAARC$_{Hero}$, SPAARC$_{MATLAB}$ and MIRP from the IBSI validation dataset a) CT, b) T1w MRI and C) F18-FDG PET.

---

4          https://pingouin-stats.org/

## REFERENCES

[1]  J. J. Birchman, S. L. Tanimoto, A. H. Rowberg, H.-S. C. M.d, and Y. Kim, 'Applying a visual language for image processing as a graphical teaching tool in medical imaging', in *Medical Imaging VI: Image Capture, Formatting, and Display*, SPIE, May 1992, pp. 379–390. doi.org/10.1117/12.59516

[2]  M. E. Mayerhoefer et al., 'Introduction to Radiomics', *J. Nucl. Med.*, vol. 61, no. 4, pp. 488–495, Apr. 2020. doi.org/10.2967/jnumed.118.222893

[3]  A. Zwanenburg *et al.*, 'The Image Biomarker Standardization Initiative: Standardized Quantitative Radiomics for High-Throughput Image-based Phenotyping', *Radiology*, vol. 295, no. 2, pp. 328–338, May 2020.
doi.org/10.1148/radiol.2020191145

[4]  P. Whybra *et al.*, 'The Image Biomarker Standardization Initiative: Standardized Convolutional Filters for Reproducible Radiomics and Enhanced Clinical Insights', *Radiology*, vol. 310, no. 2, p. e231319, Feb. 2024.
doi.org/10.1148/radiol.231319

[5]  C. Nioche *et al.*, 'LIFEx: A Freeware for Radiomic Feature Calculation in Multimodality Imaging to Accelerate Advances in the Characterization of Tumor Heterogeneity', *Cancer Research*, vol. 78, no. 16, pp. 4786–4789, Aug. 2018.
doi.org/10.1158/0008-5472.CAN-18-0125

[6]  J. J. M. Van Griethuysen *et al.*, 'Computational Radiomics System to Decode the Radiographic Phenotype', *Cancer Research*, vol. 77, no. 21, pp. e104–e107, Nov. 2017.
doi.org/10.1158/0008-5472.CAN-17-0339.

[7]  A. Zwanenburg *et al.*, 'Assessing robustness of radiomic features by image perturbation', *Sci. Rep.*, vol. 9, no. 1, p. 614, Jan. 2019.
doi.org/10.1038/s41598-018-36938-4

[8]  P. Whybra,'Standardisation and optimisation of radiomic techniques for the identification of robust imaging biomarkers in oncology', PhD Thesis, Cardiff University, 2021.

[9]  P. Whybra, C. Parkinson, K. Foley, J. Staffurth, and E. Spezi, 'Assessing radiomic feature robustness to interpolation in 18F-FDG PET imaging', *Sci. Rep.*, vol. 9, no. 1, p. 9649, Jul. 2019.
doi.org/10.1038/s41598-019-46030-0

[10] C. Piazzese, K. Foley, P. Whybra, C. Hurt, T. Crosby, and E. Spezi, 'Discovery of stable and prognostic CT-based radiomic features independent of contrast administration and dimensionality in oesophageal cancer', *PLoS ONE*, vol. 14, no. 11, p. e0225550, Nov. 2019.
doi.org/10.1371/journal.pone.0225550

[11] A. Depeursinge *et al.*, 'Standardised convolutional filtering for radiomics', Feb. 07, 2024, *arXiv*, 7 Feb. 2024. doi.org/10.48550/arXiv.2006.05470

[12] A. Zwanenburg, S. Leger, M. Vallières, and S. Löck, 'Image biomarker standardisation initiative', *Radiology*, vol. 295, no. 2, pp. 328–338, May 2020. doi.org/10.48550/arXiv.1612.07003

## Kim KW

*Cardiff University*
*School of Engineering*

## Duman A

*Cardiff University*
*School of Engineering*

## Spezi E

*Cardiff University*
*School of Engineering*

AI AND DEEP LEARNING

# RGU-Net: Computationally Efficient U-Net for Automated Brain Extraction of mpMRI with Presence of Glioblastoma

Brain extraction refers to the process of removing non-brain tissues in brain scans and is one of the initial pre-processing procedures in neuroimage analysis. Since errors produced during this process can be challenging to amend in subsequent analyses, accurate brain extraction is crucial. Most deep learning-based brain extraction models are optimised on performance, leading to computationally expensive models. Such models may be ideal for research; however, they are not ideal in a clinical setting. In this work, we propose a new computationally efficient 2D brain extraction model, named RGU-Net. RGU-Net incorporates Ghost modules and residual paths to accurately extract features and reduce computational cost. Our results show that RGU-Net has 98.26% fewer parameters compared to the original U-Net model, whilst yielding state-of-the-art performance of 97.97 ± 0.84% Dice similarity coefficient. Faster run time was also observed in CPUs which illustrates the model's practicality in real-world applications.

## INTRODUCTION

Brain extraction, also known as brain segmentation or skull stripping, is one of the initial pre-processing stages for neuroimage analysis and refers to the process of separating brain and non-brain (e.g. eyes, neck, skull) tissues in Magnetic Resonance Imaging (MRI) scans through medical image segmentation [1, 2]. The quality of brain extraction has a significant impact on subsequent analysis as errors produced during this process will be present in further stages of the analysis. To this day, manual segmentation is still considered the "gold standard", however, such a method is prone to introducing inter and intra-rater variability between radiologists and the process is extremely time-consuming [3].

In recent years, there has been an increase in the demand for neuroimage analysis and the size of datasets, resulting in the difficulty of performing manual segmentation. To tackle this problem, several deep learning models have been developed [4 - 9], as the implementation of the deep learning approach allows the decrease of the cost associated with the radiologist and the time taken to produce the segmentation. However, most studies to date focused on increasing the performance, often resulting in computationally inefficient models which are not ideal for deployment in a clinical setting.

To address this problem, we developed a computationally efficient 2D brain extraction model which has similar performance as the original U-Net [10] but requires significantly less computational power. The proposed model, Residual Ghost U-Net (RGU-Net), integrates Ghost modules and residual paths to enhance feature extraction whilst decreasing the number of trainable parameters to achieve computational efficiency. Our objective is not to claim the proposed model's optimality for the task or to compare the model to existing brain extraction algorithms, but instead focus on potential lightweight architecture to increase the practicality of deep learning-based approaches in clinical settings.

## MATERIALS AND METHODS

*Dataset: UPenn-GBM*
The proposed model was developed and validated using the publicly available dataset, UPenn-GBM[1]. The UPenn-GBM dataset contains multi-parametric MRI (mpMRI) scans of 630 patients diagnosed with glioblastoma and a brain segmentation produced using a deep learning model [11]. The dataset includes 611 MRI scans prior to initial surgery and 60 follow-up scans for the second resection surgery. For this study, four structural MRI scans were used: T1-weighted (T1; n=671), gadolinium-based agent-enhanced T1 (T1Gd; n=671), T2-weighted (T2; n=671), and Fluid Attenuated Inversion Recovery (FLAIR; n=671) scans. The dataset was split into training (n=1612), validation (n=536), and testing (n=536) datasets.

*Data Pre-processing and Augmentation*
To develop a computationally efficient model, a 2D segmentation approach was proposed as 3D convolutional layers are computationally expensive to operate. Due to this, the MRI scans were converted from NIfTI imaging format to a series of 2D JPEG images.

Additionally, data augmentation and transformation techniques were applied to increase the variety of the

training and validation data. Five transformations were applied to the original scans: horizontal flip, vertical flip, rotation, random brightness, and elastic transformation. Each transformation had a 50% chance of being applied, allowing random combinations of transformations, creating a unique dataset with a wide variety of data.

*Network Architecture and Implementation*
RGU-Net (Fig. 1) is a modification of the U-Net architecture [10] optimised for automated brain extraction, with a focus on decreasing computational cost through the incorporation of Ghost modules and residual paths. Ghost modules, which were first proposed by Han et al. [12], were implemented to produce feature maps at a lower computational cost compared to the conventional convolutional layer approach. In addition to this, residual paths [13] were also integrated into the architecture to allow the deeper layers of the model to capture appropriate features during the training.



Fig. 1. Overview of RGU-Net architecture.
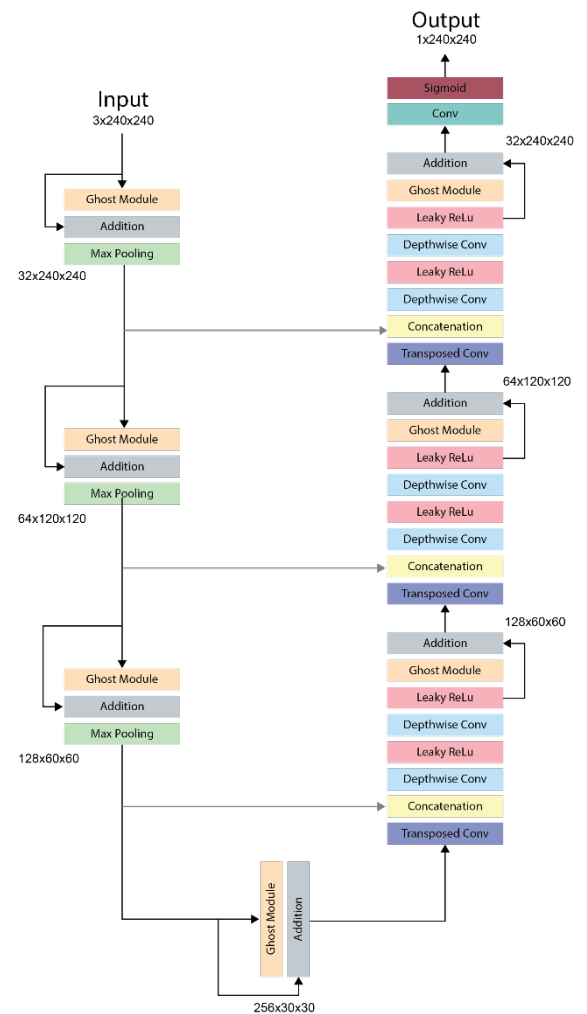
The ablation study showed that the combination of Ghost modules and residual paths alone reduces the performance of the model. Therefore, asymmetrical encoder-decoder architecture was introduced to further enhance the performance. The decoder block incorporates two additional depthwise convolutional layers followed by Leaky ReLU (α=0.01). This approach further reduces noise

and increases performance, by reconstructing accurate segmentation masks of the brain. The combination of Ghost modules, residual paths, and asymmetrical encoder-decoder has shown success in producing accurate predicted masks and requires significantly fewer trainable parameters.

RGU-Net was implemented using the PyTorch framework [14]. During the training process, a Dice loss function was implemented to monitor the performance of the model. The Dice loss function ranges from 0 to 1, where 0 means the predicted mask (PM) is identical to the ground truth (GT). The loss function is expressed as:

$$L_{Dice} = 1 - \frac{2 \cdot |PM \cap GT|}{|PM| + |GT|} \qquad (1)$$

Furthermore, to prevent overfitting of the model, a validation loop was implemented after every training epoch, and the model parameters were saved when the validation loss improved. The model was trained with the Adam optimiser algorithm [15] with an initial learning rate of 0.0001. If the validation loss does not improve for three epochs, the learning rate decays by a factor of 0.1. The decaying learning rate aids the model to learn complex patterns and increases the performance [16]. Lastly, to decrease training time, an early stopper function was implemented to stop the training when the model converges.

*Post-processing*
3D segmentation was produced through the concatenation of a series of 2D PMs. Thresholding and a post-processing technique introduced by Lucena et al. [4] were applied to the concatenated 3D masks. This allowed the reduction of floating segments and noise, producing a clean brain segmentation mask.

**RESULTS**

The proposed model was evaluated using the Dice similarity coefficient (DSC), which compares the similarity between the PM and the GT [17]. The DSC can be calculated as follows:

$$DSC = \frac{2 \cdot |PM \cap GT|}{|PM| + |GT|} \times 100 \qquad (2)$$

Additionally, the number of model parameters were calculated using the model summary function from PyTorch.

Figure 2 shows the segmentation results in mpMRI scans of three random slices from each MRI sequence to illustrate the general segmentation generated by RGU-Net. The red arrow indicates areas of over/under-segmentation of the brain.
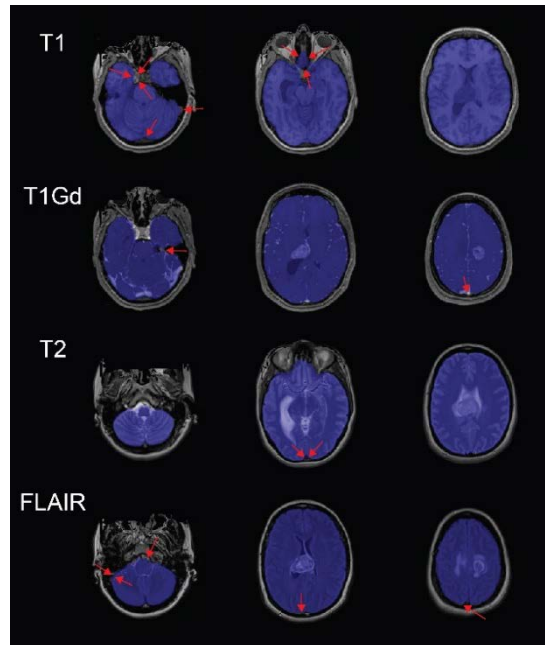


Fig. 2. The segmentation results of RGU-Net in different MRI sequences. Red arrows indicate regions of over/under-segmentation.

*Ablation study*
The ablation study was conducted to investigate the effect of encoder and decoder blocks using a baseline model and two additional variations of RGU-Net: U-Net (baseline), RGU-Net without residual paths, RGU-Net without asymmetrical encoder-decoder, and RGU-Net. All models were implemented as specified and hyper-parameters were kept constant. Table 1 shows the comparison of model performances. Furthermore, the average run time to produce a 3D segmentation on a CPU device (Intel Core i7-1165G7) was measured and showed that the proposed RGU-Net is 80 seconds faster than the U-Net model.

| Model | No. Param | Run time (s) | DSC (%) | | | |
|---|---|---|---|---|---|---|
| | | | T1 | T1Gd | T2 | FLAIR |
| U-Net (baseline) | 31.03M | 113 | 98.10.9 | 98.01.0 | 97.80.9 | 97.61.0 |
| RGU-Net w/o residual paths | 0.56M | 19 | 97.71.0 | 97.51.1 | 97.40.9 | 97.11.1 |
| RGU-Net w/o asymmetrical encoder-decoder | 0.65M | 24 | 97.61.0 | 97.51.1 | 97.31.0 | 97.11.4 |
| RGU-Net | 0.54M | 33 | 98.00.8 | 97.81.0 | 97.70.9 | 97.51.1 |

Table 1. Performance comparison for ablation study.

## DISCUSSION

RGU-Net demonstrated state-of-the-art performance in automated brain extraction, whilst maintaining significantly less trainable parameters, as shown in Table 1. Despite slightly lower performance compared to the U-Net, all differences are considered to be clinically insignificant since segmentations produced by trained radiologists have greater variance between segmentation masks [18].

All models in the ablation study exhibited the highest performance on T1 scans, followed by T1Gd, T2, and FLAIR scans, suggesting sensitivity to the different contrast settings of MRI scans. This could be mitigated by introducing contrast transformation to the training data during data augmentation. While RGU-Net demonstrates high performance. In some MRI slices, signs of over/under-segmentation were observed (Fig. 2), suggesting further optimisation of the model is needed. The use of a single dataset during the development of the model reduced the variety of image acquisition within the training data. Leading to poorer performance when MRI scans with different imaging parameters are inputted. To address this, an increase in the number of datasets and input from radiology consultants is highly recommended.

Furthermore, to increase the accuracy of the model whilst decreasing the number of parameters, an asymmetrical encoder-decoder architecture was introduced. However, the method increased the number of operations, and Table 1 suggests a correlation between the model complexity and the run time of the model. Therefore, further investigation on the model's complexity and run time is required to further optimise the model to improve computational efficiency. Additionally, to decrease computational cost of the model, 2D convolutional layers were implemented, limiting the model's ability to capture 3D contextual and spatial information. Although the high DSC implies that this loss is not significant, it is worth exploring a potential implementation of the 3D convolutional layer for optimised performance.

One of the major strengths of RGU-Net is the computational efficiency of the model, achieved through the implementation of Ghost modules and residual paths which make the model ready for in real-world applications in environments where access to powerful computing devices is not warranted. This is crucial for the integration of automated brain extraction tools into clinical workflow, as the run time of the model will accumulate when inputted with a large dataset.

## CONCLUSION

Overall, RGU-Net showed promising results for automated brain extraction. Its high performance, computational efficiency and compatibility with CPUs make the model a valuable tool for neuroimage analysis. Further research and optimisation of the model could further enhance the reliability, performance and computational efficiency of the model.

*Conflicts of Interest*
*The authors declare no conflict of interest.*

*Data Availability Statement*
*The UPenn-GBM dataset is publicly available at The Cancer Imaging Archive (TCIA): doi.org/10.7937/TCIA.709X-DN49. Source code of this study has been made publicly available at: https://github.com/KWKIM128/Brain_Extraction*

## REFERENCES

[1]    H. Z. U. Rehman, H. Hwang, and S. Lee, 'Conventional and Deep Learning Methods for Skull Stripping in Brain MRI', *Applied Sciences*, vol. 10, no. 5, p. 1773, Mar. 2020. doi.org/10.3390/app10051773

[2]    P. Kalavathi and V. B. S. Prasath, 'Methods on Skull Stripping of MRI Head Scan Images—a Review', *J. Digit. Imaging*, vol. 29, no. 3, pp. 365–379, Jun. 2016. doi.org/10.1007/s10278-015-9847-8

[3]    F. Yepes-Calderon and J. Gordon McComb, 'Manual Segmentation Errors in Medical Imaging. Proposing a Reliable Gold Standard', in *Applied Informatics*, vol. 1051, H. Florez, M. Leon, J. M. Diaz-Nafria, and S. Belli, Eds., Cham: Springer International Publishing, 2019, pp. 230–241. doi.org/10.1007/978-3-030-32475-9_17

[4]    O. Lucena, R. Souza, L. Rittner, R. Frayne, and R. Lotufo, 'Convolutional neural networks for skull-stripping in brain MR imaging using silver standard masks', *Artificial Intelligence in Medicine*, vol. 98, pp. 48–58, Jul. 2019. doi.org/10.1016/j.artmed.2019.06.008

[5]    S. Thakur *et al.*, 'Brain extraction on MRI scans in presence of diffuse glioma: Multi-institutional performance evaluation of deep learning methods and robust modality-agnostic training', *NeuroImage*, vol. 220, p. 117081, Oct. 2020. doi.org/10.1016/j.neuroimage.2020.117081

[6]    F. Isensee *et al.*, 'Automated brain extraction of multisequence MRI using artificial neural networks', Human Brain Mapping, vol. 40, no. 17, pp. 4952–4964, Dec. 2019. doi.org/10.1002/hbm.24750

[7]    L. Pei *et al.*, 'A general skull stripping of multiparametric brain MRIs using 3D convolutional neural network', *Sci. Rep.*, vol. 12, no. 1, p. 10826, Jun. 2022. doi.org/10.1038/s41598-022-14983-4

[8]    A. Hoopes, J. S. Mora, A. V. Dalca, B. Fischl, and M. Hoffmann, 'SynthStrip: skull-stripping for any brain image', *NeuroImage*, vol. 260, p. 119474, Oct. 2022. doi.org/10.1016/j.neuroimage.2022.119474

[9]    J. S. Park, S. Fadnavis, and E. Garyfallidis, 'Multi-scale V-net architecture with deep feature CRF layers for brain extraction', *Commun. Med.*, vol. 4, no. 1, p. 29, Feb. 2024. doi.org/10.1038/s43856-024-00452-8

[10]   O. Ronneberger, P. Fischer, and T. Brox, 'U-Net: Convolutional Networks for Biomedical Image Segmentation', in *Medical Image Computing and Computer-Assisted Intervention – MICCAI 2015*, vol. 9351, N. Navab, J. Hornegger, W. M. Wells, and A. F. Frangi, Eds., Cham: Springer International Publishing, 2015, pp. 234–241. doi.org/10.1007/978-3-319-24574-4_28

[11]   S. Bakas *et al.*, 'The University of Pennsylvania glioblastoma (UPenn-GBM) cohort: advanced MRI, clinical, genomics, & radiomics', *Sci. Data*, vol. 9, no. 1, p. 453, Jul. 2022. doi.org/10.1038/s41597-022-01560-7

[12]   K. Han, Y. Wang, Q. Tian, J. Guo, C. Xu, and C. Xu, 'GhostNet: More Features From Cheap Operations', in *2020 IEEE/CVF Conference on Computer Vision and Pattern Recognition (CVPR)*, Seattle, WA, USA: IEEE, Jun. 2020, pp. 1577–1586. doi.org/10.1109/CVPR42600.2020.00165

[13]   K. He, X. Zhang, S. Ren, and J. Sun, 'Deep Residual Learning for Image Recognition', in *2016 IEEE Conference on Computer Vision and Pattern Recognition (CVPR)*, Las Vegas, NV, USA: IEEE, Jun. 2016, pp. 770–778. doi.org/10.1109/CVPR.2016.90

[14]   A. Paszke *et al.*,'Pytorch: An imperative style, high-performance deep learning library'. *NeurIPS* 2019, 32. doi.org/10.48550/ARXIV.1912.01703

[15]   D. P. Kingma and J. Ba, 'Adam: A Method for Stochastic Optimization', *arXiv*, Jan. 29, 2017. doi.org/10.48550/arXiv.1412.6980

[16]   K. You, M. Long, J. Wang, and M. I. Jordan, 'How Does Learning Rate Decay Help Modern Neural Networks?', *arXiv*, 26 Sep. 2019. doi.org/10.48550/arXiv.1908.01878

[17]   L. R. Dice, 'Measures of the Amount of Ecologic Association Between Species', *Ecology*, vol. 26, no. 3, pp. 297–302, Jul. 1945. doi.org/10.2307/1932409

[18]   M. A. Deeley *et al.*, 'Comparison of manual and automatic segmentation methods for brain structures in the presence of space-occupying lesions: a multi-expert study', *Phys. Med. Biol.*, vol. 56, no. 14, pp. 4557–4577, Jul. 2011. doi.org/10.1088/0031-9155/56/14/021

## Zhao Z

*Cardiff University*
*School of Engineering*

## Hicks Y

*Cardiff University*
*School of Engineering*

## Sun X

*Cardiff University*
*School of Computer Science*
*and Informatics*

AI AND DEEP LEARNING

# Faster Segmentation Models for Peach Ripeness Determination

To build an in-field fruit harvesting robot, it is important to locate the fruit efficiently and accurately. Instance segmentation is incorporated to evaluate peach ripeness, which enables precise identification of the ripeness level for each peach instance, allowing robots to selectively harvest ripe peaches, thereby maximizing harvesting efficiency. We have proposed a peach-specific instance segmentation model comprising three components: a ResNet50 backbone, a Feature Pyramid Network (FPN), and a Transformer decoder. Demonstrating a mean average precision (mAP) of 66.401, our model outperforms other state-of-the-art models in accurately segmenting peach instances. Notably, it achieves impressive AP of 64.818 for unripe peaches, 62.640 for semi-ripe ones, and 71.745 for ripe peaches, highlighting its effectiveness across varying ripeness levels. The model maintains the rapidest inference time of 91 ms per iteration. This comprehensive summary underscores the model's efficacy in peach instance segmentation, promising significant advancements in automated fruit harvesting and agricultural productivity.

*Keywords:*
*Segmentation, artificial intelligence, fruit, robot.*

*Corresponding author:*
*ZhaoZ60@cardiff.ac.uk*

## INTRODUCTION

The rapid advancement of artificial intelligence has revolutionized the agricultural sector. For example, the development of automated harvesting robots represents a significant trend in the field of agricultural automation, offering a promising solution to challenges such as labor shortages and rising labor costs faced by farmers. However, to achieve efficient fruit harvesting, robots must possess the ability to accurately identify and locate fruits to ensure harvesting efficacy and quality. In this regard, the technology of fruit instance segmentation plays a pivotal role. Fruit instance segmentation, leveraging computer vision and deep learning techniques, facilitates meticulous analysis and processing of fruit images, identifying various parts such as the fruit body, leaves, and branches, and accurately delineating them. This precise segmentation capability furnishes crucial information to automated harvesting robots, enabling them to precisely localize the position and size of fruits, thereby minimizing damage and waste during harvesting operations.

Through fruit instance segmentation technology, automated harvesting robots can better plan harvesting trajectories, optimize harvesting actions, and enhance harvesting efficiency through real-time adjustments. This not only reduces the need for manual intervention and lowers harvesting costs but also improves harvesting speed and quality, maximizing the utilization of orchard yields.

In the context of fruit automation production, the efficient and precise location of the target fruit serves as the foundational prerequisite to building a fruit-picking robot, which senses the working surroundings and guides the robotic arm to detach the fruits. Accurately locating target fruits is fundamental for developing efficient fruit-picking robots. These robots utilize sensors to perceive their environment and guide robotic arms to detach fruits. Over recent years, numerous harvesting robots have emerged for various fruits and crops, including kiwifruit [1], apple [2], green citrus [3] and asparagus spear [4].

Instance segmentation models offer individual identification for each fruit, enabling robots to precisely pinpoint the location of each peach instance. There are several works that have applied segmentation on agriculture. Xu et al. [5] proposed an enhanced instance segmentation model which accepts RGB and depth images for robust visual recognition for cherry tomatoes. Yu et al. [6] introduced Mask RCNN to improve the performance of fruit detection for a strawberry harvesting robot.

However, most of existing works do not consider the ripeness of the target fruit when designing the segmentation model for harvesting robot, thus results in some unnecessary loss when performing automatic in-field fruit picking.

To alleviate this problem, this paper proposed a fast and efficient instance segmentation model to determine in-field peaches at different ripeness stages. This capability facilitates precise harvesting actions, minimizing plant damage, and ensuring selective picking of only ripe fruits.

## MATERIALS AND METHODS

*The NinePeach Dataset*
In this paper, the NinePeach dataset [7] is selected to test the performance of the segmentation models. A total of 3849 images were captured in a peach orchard at various times throughout a complete picking campaign, representing nine cultivars of peaches that have been classified into three distinct stages of ripeness: unripe, semi-ripe, and ripe. These images are organized into training, and validation subsets, encompassing 2690 and 1159 images, respectively. Samples of images from each kind of peach are presented in Fig. 1.



Fig. 1. The NinePeach Dataset.

To our best knowledge, the NinePeach dataset is the largest and the most varied peach dataset among publicly available peach datasets with individual instance annotation provided. It includes some challenging in-field scenarios like varying natural light intensity, instances of multiple fruit adhesion, and occlusion caused by stems and leaves. The instance category distribution of the dataset can be seen at Table 1.

| Category | Train | Validation |
|----------|-------|------------|
| unripe | 3669 | 1717 |
| semiripe | 3312 | 1307 |
| ripe | 1307 | 737 |
| **Total** | **8679** | **3761** |

Table 1. The instance category distribution of the NinePeach dataset.
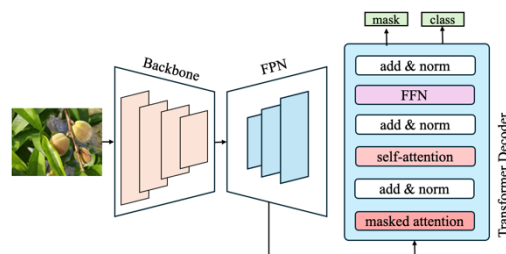
*The Segmentation Model*



Fig. 2. The proposed segmentation model.

The structure of our segmentation model is shown in Fig. 2. It mainly consists of three parts: a backbone, a FPN and a Transformer decoder.

**Backbone**. Image feature extraction is the process of identifying and extracting relevant information or features from an image. ResNet [8] was proposed to solve the

image classification task. ResNet's residual blocks enable the learning of residual functions, making it easier for the network to approximate the identity mapping. This property enhances gradient flow during training, enabling smoother optimization and faster convergence. As a result, ResNet's ability to effectively combat degradation and facilitate the training of extremely deep networks makes it a highly desirable choice as a backbone architecture. This makes it easier for ResNet to learn useful features from the input image. ResNet50 is used as backbone in our segmentation model.

**FPN.** The Feature Pyramid Network (FPN) [9] was introduced to extend the backbone network, which is especially effective for the detection of targets at different scales. FPN works by taking the feature maps produced by backbone at different levels of the network, and building a feature pyramid that includes high-level features with strong semantics, as well as low-level features with strong spatial information. By combining features from various depths of the network, FPN enables the generation of a hierarchical pyramid of features, where each level corresponds to a different scale of the input image. This hierarchical representation facilitates the extraction of rich and diverse information, allowing the network to effectively handle objects of varying sizes and complexities. Additionally, FPN incorporates lateral connections to enhance feature propagation across different scales, enabling seamless information flow and promoting robust feature extraction. The final output of the FPN consists of a set of feature maps at four resolutions. We use FPN to fuse all features at different scales.

**Transformer Decoder.** The Transformer decoder module serves as a critical role within the model's architecture, acting as a pivotal bridge between the learned features extracted by the Feature Pyramid Network and the generation of final output predictions. Inspired by the foundational design principles of the original Transformer architecture [10], the decoder component orchestrates the transformation of object embeddings into output embeddings. Comprising a series of stacked decoder layers, each layer is meticulously crafted to incorporate essential components such as masked attention mechanisms, self-attention layers, and feed-forward networks (FFN). This intricate architecture allows the decoder to effectively capture intricate context dependencies and semantic relationships within the input data. In each Transformer decoder layer, the model generates predictions for both mask and class, leveraging the rich contextual information encoded within the feature representations. However, to ensure optimal performance and efficiency, only the predictions from the last layer are utilized as the final output. By strategically configuring the number of Transformer decoder layers to 3, we strike a delicate balance between model accuracy and computational efficiency.

## RESULTS

*Training details*
The experiments are meticulously conducted using Python 3.9 and PyTorch 1.13, leveraging the computational power of two Nvidia Tesla P100 GPUs. Employing the efficient AdamW [11] optimizer coupled with a meticulously designed step learning rate schedule, our initial learning rate is set at 0.0001, accompanied by a weight decay of 0.05. To fine-tune the training process, a learning rate multiplier of 0.1 is strategically applied to the backbone architecture.

Additionally, we employ a progressive decay strategy, decreasing the learning rate by a factor of 10 at specific intervals corresponding to 0.9 and 0.95 fractions of the total training iterations. This comprehensive training regimen ensures the robustness and generalization capability of our models. The batch size is 8.

*Average Precision*
Precision acts as a prevalent and established measure for assessing the network's capacity to precisely detect target objects, mirroring the overall efficacy of the network. We calculated the average precision of proposed model every 5k iterations, as reported in Table 2.

| Iteration | mAP | $AP_{unripe}$ | $AP_{semiripe}$ | $AP_{ripe}$ |
|-----------|--------|--------|--------|--------|
| 15k | 54.204 | 51.580 | 50.693 | 60.338 |
| 20k | 61.179 | 58.281 | 56.655 | 68.600 |
| 25k | 63.051 | 60.695 | 57.503 | 70.956 |
| 30k | 62.356 | 63.677 | 58.413 | 64.978 |
| 35k | 64.449 | 59.082 | 62.236 | 72.029 |
| 40k | 66.401 | 64.818 | 62.640 | 71.745 |
| 45k | 65.670 | 64.225 | 61.469 | 71.315 |

Table 2. The average precision of our proposed model across iterations.

We observe a gradual improvement in the mean average precision (mAP) as the number of training iterations increases. From 15k to 45k iterations, the mAP increases from 54.204 to 65.670, indicating enhancements in the model's ability to recognize and segment target objects. Regarding the AP for different classes, we note the performance in identifying various levels of fruit ripeness. With the progression of training, most classes exhibit an upward trend in average precision. Particularly noteworthy is the "ripe" class, where the AP increases from 60.338 to 71.315, signifying significant improvement in identifying ripe fruits. In the "unripe" class, the increase in AP is relatively modest, rising from 51.580 to 64.225, suggesting the need for additional training data or model adjustments to further enhance performance. However, 40k iteration shows slightly better results than 45k, therefore it is selected as our final output model.

| Model | mAP | $AP_{unripe}$ | $AP_{semiripe}$ | $AP_{ripe}$ |
|-------|--------|--------|--------|--------|
| Mask2Former | 61.088 | 53.926 | 58.889 | 70.449 |
| CMT | 61.179 | 58.281 | 56.655 | 68.600 |
| PVT | 63.051 | 60.695 | 57.503 | 70.956 |
| Ours | 66.401 | 64.818 | 62.640 | 71.745 |

Table 3. The average precision of different models.

We compared the performance of our model and other similar state-of-the-art models Mask2Former [12], CMT [13] and PVT [14]. The results are shown in Table 3, highlight our model's superior performance within the same experimental framework, surpassing all other models across all metrics. With improvements of 5.313, 5.222, and 3.350 in mAP, our model demonstrates a strong performance compared to its counterparts. Notably, the relatively lower APunripe suggests that the unripe peaches are usually difficult to detect due to their green colour. On the contrary, all models demonstrate higher APripe indicates that

ripe peaches are relatively easy to find because they are distinguishable from the leaves and trunks.

Our model outperforms the other state-of-the-art models across the three ripeness classes, demonstrating superior capability in detecting fruit at various ripeness stages. This indicates its potential as a highly effective tool for applications requiring precise ripeness classification.

| Model | Inference |
|---|---|
| Mask2Former | 121 ms/iter |
| CMT | 130 ms/iter |
| PVT | 109 ms/iter |
| Ours | 91 ms/iter |

Table 4. The inference speed of different models.

In terms of model efficiency, we report the inference speed of our model and the counterparts. The inference time denotes the time taken by the model to process the input data and generate predictions. This encompasses the forward pass through the model architecture, including operations such as feature extraction, feature ablation, and object prediction.

With the shortest inference time of 91 ms per iteration, our model demonstrates its capability to process input data swiftly and accurately. Compared to Mask2Former, CMT, and PVT, our model operates 24.8%, 30.0%, and 16.5% faster, respectively, underscoring its efficiency. Overall, the combination of efficient data loading and swift inference times highlights the effectiveness and practicality of our model for real-world applications, where both speed and accuracy are important.

*Visualization*
Figure 3 presents a visual representation of our model's performance, showcasing its capability to accurately segment peaches across diverse conditions. Despite encountering challenging scenarios where peaches are positioned at the periphery of the image or partially obscured, our proposed models demonstrate robustness and precision in segmenting these instances. This resilience underscores the model's ability to generalize well to various real-world conditions and effectively delineate peach instances from complex backgrounds.

Moreover, our model exhibits consistent performance across different scenarios, accurately capturing the contours and boundaries of peaches regardless of their location or occlusion level. This reliability is crucial for practical applications where precise fruit segmentation is paramount, such as automated harvesting or quality assessment in agricultural settings.



Fig. 3. Visualization of the segmentation.

## CONCLUSION

Integrating instance segmentation for assessing peach ripeness enhances the intelligence and efficiency of automatic fruit-picking robots. By accurately identifying the ripeness level of each peach instance, robots can selectively harvest ripe fruits, maximizing harvesting efficiency while avoiding picking immature ones. To achieve this, we have introduced an instance segmentation model specifically designed for peaches, comprising three key components: a ResNet50 backbone, a FPN, and a Transformer decoder. With the highest mAP of 66.401, our model demonstrates better performance in segmenting peach instances comparing to other state-of-the-art models. Notably, it achieves AP scores of 64.818 for unripe peaches, 62.640 for semi-ripe ones, and 71.745 for ripe peaches, showcasing its effectiveness across different ripeness levels. Despite its high accuracy, the model maintains the shortest inference time of 91 ms per iteration, ensuring swift processing suitable for real-time applications. This comprehensive summary underscores the model's efficacy in peach instance segmentation, promising advancements in automated fruit harvesting and agricultural productivity.

*Conflicts of Interest*
*The authors declare no conflict of interest.*

### REFERENCES

[1] L. Mu, G. Cui, Y. Liu, Y. Cui, L. Fu, and Y. Gejima, 'Design and simulation of an integrated end-effector for picking kiwifruit by robot', *Information Processing in Agriculture*, vol. 7, no. 1, pp. 58–71, Mar. 2020. doi.org/10.1016/j.inpa.2019.05.004

[2] H. Kang and C. Chen, 'Fruit detection, segmentation and 3D visualisation of environments in apple orchards', *Computers and Electronics in Agriculture*, vol. 171, p. 105302, Apr. 2020. doi.org/10.1016/j.compag.2020.105302

[3] J. Lu *et al.*, 'Lightweight green citrus fruit detection method for practical environmental applications', *Computers and Electronics in Agriculture*, vol. 215, p. 108205, Dec. 2023. doi.org/10.1016/j.compag.2023.108205

[4] M. Peebles, S. H. Lim, M. Duke, and B. McGuinness, 'Investigation of Optimal Network Architecture for Asparagus Spear Detection in Robotic Harvesting', *IFAC-PapersOnLine*, vol. 52, no. 30, pp. 283–287, 2019. doi.org/10.1016/j.ifacol.2019.12.535

[5] P. Xu, N. Fang, N. Liu, F. Lin, S. Yang, and J. Ning, 'Visual recognition of cherry tomatoes in plant factory based on improved deep instance segmentation', *Computers and Electronics in Agriculture*, vol. 197, p. 106991, Jun. 2022. doi.org/10.1016/j.compag.2022.106991

[6] Y. Yu, K. Zhang, L. Yang, and D. Zhang, 'Fruit detection for strawberry harvesting robot in non-structural environment based on Mask-RCNN', *Computers and Electronics in Agriculture*, vol. 163, p. 104846, Aug. 2019. doi.org/10.1016/j.compag.2019.06.001

[7] Z. Zhao, Y. Hicks, X. Sun, and C. Luo, 'Peach ripeness classification based on a new one-stage instance segmentation model', *Computers and Electronics in Agriculture*, vol. 214, p. 108369, Nov. 2023, doi.org/10.1016/j.compag.2023.108369

[8] K. He, X. Zhang, S. Ren, and J. Sun, 'Deep Residual Learning for Image Recognition', in *2016 IEEE Conference on Computer Vision and Pattern Recognition (CVPR)*, Las Vegas, NV, USA: IEEE, Jun. 2016, pp. 770–778 doi.org/10.1109/CVPR.2016.90

[9] T.-Y. Lin, P. Dollar, R. Girshick, K. He, B. Hariharan, and S. Belongie, 'Feature Pyramid Networks for Object Detection', in *2017 IEEE Conference on Computer Vision and Pattern Recognition (CVPR)*, Honolulu, HI: IEEE, Jul. 2017, pp. 936–944. doi.org/10.1109/CVPR.2017.106

[10] A. Vaswani *et al.*, 'Attention Is All You Need', *arXiv*, 1 Aug. 2023. doi.org/10.48550/arXiv.1706.03762

[11] I. Loshchilov and F. Hutter, 'Decoupled Weight Decay Regularization', *arXiv*, 4 Jan. 2019. doi.org/10.48550/arXiv.1711.05101

[12] B. Cheng, I. Misra, A. G. Schwing, A. Kirillov, and R. Girdhar, 'Masked-attention Mask Transformer for Universal Image Segmentation', in *2022 IEEE/CVF Conference on Computer Vision and Pattern Recognition (CVPR)*, New Orleans, LA, USA: IEEE, Jun. 2022, pp. 1280–1289. doi.org/10.1109/CVPR52688.2022.00135

[13] J. Guo *et al.*, 'CMT: Convolutional Neural Networks Meet Vision Transformers', *arXiv*, 14 Jun. 2022. doi.org/10.48550/arXiv.2107.06263

[14] W. Wang *et al.*, 'Pyramid Vision Transformer: A Versatile Backbone for Dense Prediction without Convolutions', *arXiv*, 11 Aug. 2021. doi.org/10.48550/arXiv.2102.12122

## Degani I

*Cardiff University*
*School of Engineering*

## Maddalena R

*Cardiff University*
*School of Engineering*

## Kulasegaram S

*Cardiff University*
*School of Engineering*

NET ZERO

# The Effect of Curing Temperature and Supplementary Cementitious Materials on Chloride Permeability of Self-Compacting Concrete

In recent years, self-compacting concrete (SCC) has gained popularity due to its high flowability and reduced energy demand in construction. With a notable paste content, SCC undergoes intensified hydration reactions, resulting in a distinct microstructure compared to traditional concrete. When exposed to varying curing temperatures, SCC exhibits unique mechanical traits. However, the influence of curing temperature on SCC with supplementary cementitious materials (SCMs) remains underexplored. This study evaluates SCC performance with diverse SCMs, substituting specific volume fractions of cement with 10% silica fume (SF) and 40% fly ash (FA), under different curing temperatures. Emphasis lies on assessing the durability of these compositions for concrete structures. For evaluating critical chloride permeability, high-strength SCC specimens were cured underwater at 10 °C, 20 °C, and 50 °C. Incorporating supplementary cementitious materials (SCMs) enhances SCC's resistance to chloride permeability and mitigates the adverse effects of elevated curing temperatures. The study showcased remarkable enhancements in concrete performance with the addition of silica fume (SF) and fly ash (FA) compared to plain SCC. Particularly, at 10 °C, SCC with SF exhibited a significant increase rate of 78.89% over SCC without SF. These results underscore the pivotal role of SF and FA in bolstering the electrical resistance of SCC under different curing temperatures.

The Effect of Curing Temperature and Supplementary
Cementitious Materials on Chloride Permeability of
Self-Compacting Concrete

39

## INTRODUCTION

The development of new types of concrete has opened up new possibilities in the construction field. One of these innovations is self-compacting concrete (SCC), first developed in Japan in the 1980s. SCC is a type of concrete that flows naturally through formwork without the need for vibration, filling it in a seamless manner and compacting under its own weight as it passes through reinforcing bars [1]. SCC boasts excellent deformability, passing ability, and high segregation resistance, making it suitable for heavily reinforced applications and self-compaction. Additionally, SCC enhances construction productivity, reduces the total cost of structures, improves the work environment, and exhibits sustainable characteristics [2]self-compacting concrete (SCC [3]. Several factors influence concrete properties, notably the composition of self-compacting concrete (SCC), where the high volume of paste in SCC is considered the major cause of porosity in the concrete, whereby replacing aggregates with paste increases the volume of porous material per volume of concrete, and thus the new concrete is more porous. Various harmful substances like water, chloride ions, acids, and other hazardous elements can easily penetrate concrete through these cracks and the pore system, leading to a degradation of its strength and overall durability [4][5].

The deterioration of concrete structures induced by chlorides is widely recognized as one of the most common causes of degradation [6] [7] .

Temperature, whether arising from internal reactions, curing conditions, or ambient surroundings, constitutes another influential factor impacting the properties of concrete, shaping its microstructure. Temperature significantly influences concrete properties by affecting hydration rates and microstructure. Lower curing temperatures initially increase porosity but lead to densification over time, reducing water absorption and permeability. In contrast, higher temperatures accelerate hydration, initially creating a denser microstructure but ultimately leading to increased porosity with prolonged exposure. This dual impact of temperature on concrete properties is detailed by [8] [9].

Incorporating cementitious materials SCMs such as SF and FA into concrete mixes results in the formation of concrete with a denser and finer structure due to very fine particle size of these SCMs, consequently enhancing mechanical properties [10] [11] . Moreover, FA mitigates the impact of high temperatures on concrete, slows down the hydration reaction [12] [13] [14] [15] [16]. The mechanical and durable properties of SCC containing mineral admixtures may exhibit more pronounced variations across different temperature conditions compared to conventional concrete.

The aim of this research is to evaluate the performance of SCC containing supplementary cementitious materials (SCMs) under different curing temperatures. Specifically, the study seeks to assess the durability of SCC compositions incorporating SF and FA by analysing chloride permeability through bulk electrical resistivity testing. The research aims to investigate how variations in curing temperatures affect the mechanical and durability properties of SCC, with a focus on understanding the influence of SCMs on mitigating the adverse effects of elevated curing temperatures.

## MATERIALS AND METHODS

*Materials*
Portland cement (CEM I 52.5) was used as a binder, where Portland cement has a fineness of 384 m2/kg. Silica fume (SF) and fly ash (FA) with specific gravities of 2.4 and 2.2, respectively, were used. A poly-aryl-ether-based superplasticiser (SP) with a specific gravity of 1.07 was utilized. The fine aggregate used in this experiment is river sand sieved to a diameter of 2.0 mm and a specific gravity of 2.55; approximately 30% of the fine aggregate was replaced with limestone dust (limestone dust) with a specific gravity of 2.6 and a size ranging from 0.125 mm to 2 mm. The coarse aggregate has a specific gravity of 2.65 and a maximum size of 10 mm. Superplasticiser with a specific gravity of 1.07 was used.

*Test methods*
The fresh properties were investigated according to [17]. Cubes with a size of $100 \times 100 \times 100$ mm$^3$ were prepared for the compressive strength test in compliance with established standards outlined in BS EN 12390–3. For the bulk electrical resistivity test, 12 cylinders with 100 mm diameter and 200 mm height for each mix were performed. The test was conducted according to ASTM C1760. Nine samples for each mix were prepared: 3 samples for each curing temperature. The samples were wrapped with a plastic sheet and cured in water directly after casting. The samples were cured at 10 °C, 20 °C, 35 °C, and 50 °C for 90 days, and the tests were done at ages 1, 3, 7, 14, 28, 56, and 90 days.

## RESULTS AND DISCUSSIONS

*Fresh and hardened properties*
Table 1 presents the findings from tests on fresh properties and compressive strength after 28 days. These tests, including slump flow, J-ring, and compressive strength, were carried out as part of quality control measures to verify that the mixture attained self-compacting concrete properties and the anticipated strength.

| Mix code | (mm) | (mm) | D_slump-D_(J-ring) (mm) | Compressive strength at 28 days (MPa) | STDEV |
|---|---|---|---|---|---|
| SCC-C | 660 | 617.5 | 42.5 | 71.23 | 1.323 |
| SCC-SF-10% | 645 | 602.5 | 42.5 | 78.5 | 2.324 |
| SCC-FA-40% | 715 | 710 | 5 | 51.25 | 1.979 |

Table 1. Fresh and compressive strength results.

*Bulk Electrical Resistivity*

Figures 1 and 2 describe the results of the Bulk Electrical Resistivity test conducted on all mixes. This test is typically carried out to assess the chloride permeability in concrete samples. Observing the figures, it is clear that the electrical resistivity of all samples rises with increased curing time. Notably, the electrical resistivity of the SCC-C mix obtained the lowest electrical resistivity compared with other mixes for all curing temperatures. After 90 days of curing, the samples cured at 10 °C exhibited the highest electrical resistivity value (8.4 kΩ.cm), representing an increase of 79.7 from the 3-day curing age value of (1.7 kΩ.cm). While at for SCC-C-20 °C, the average electrical resistivity value ranges from 2.9 kΩ.cm to 7.2 kΩ.cm, showing an increased rate of 59 %. The SCC-C-50° exhibited the highest resistivity value at early ages (3.03 kΩ.cm), but later, it achieved the lowest value (4.26 kΩ.cm) compared to other SCC-C samples, showing an increase rate of 28.9 %.

This trend can be attributed to the significant impact that long-term exposure to low curing temperatures has on the hydration reaction. As the curing period extends, a microscopic structure begins to form, resulting in a denser microstructure with smaller, more uniform pores. Consequently, this transformation leads to a reduction in the porous structure, hindering ion movement and subsequently increasing electrical resistance. In contrast, high curing temperatures initially accelerate the hydration reaction, resulting in faster formation of hydration products creates pore structure and a temporary increase in electrical resistivity. Over the time, the differences in pore structure and hydration products due to the high curing temperature result in a less dense microstructure. This less dense structure allows for easier ion flow, which ultimately contributes to lower electrical resistivity. [1] [2] [3] [4].

It is observed that the addition of supplementary cementitious materials significantly enhanced the performance of concrete in terms of electrical resistivity. The SF mix achieved the highest electrical resistivity values at later curing ages. SF samples revealed that those cured at a lower temperature of 10 °C exhibited higher electrical resistivity compared to those cured at higher temperatures. The electrical resistivity value for SCC-SF-10 °C was 39.83 kΩ.cm, while for SCC-SF-20 °C it was 36.2 kΩ.cm. SCC-SF-50 °C exhibited lower electrical resistivity of 28.8 kΩ.cm. These values were higher than SCC-C values cured at the same temperature, with a rate of 78.8%, 80 %, and 85.20% higher, respectively. The electrical resistivity values of SF concrete samples cured at 10 °C and 20 °C, are highest due to the slower cement hydration rate at these temperatures, allowing for a more effective pozzolanic reaction of silica fume. This results in a denser and refined pore structure, restricting ion and electron movement and increasing resistivity. However, SF concrete samples cured 50 °C exhibit higher lower resistivity values. The higher temperatures accelerate cement hydration and initial strength development but may lead to less effective pozzolanic reaction of SF, resulting in larger pores. This facilitates easier ion and electron movement decreasing resistivity [5] [1] [6].

The addition of FA to SCC mixtures enhanced the electrical resistance performance of concrete. Its effect varied from that of SF in terms of resistance performance with temperatures. FA samples cured at 50 °C achieved the highest electrical resistivity value (36.93 kΩ.cm), This is attributed to the higher temperatures activate pozzolanic reactions in fly ash, leading to the creation of additional cementitious compounds like calcium silicate hydrate (CSH)

gel, resulting in a denser and less porous concrete matrix. This denser matrix impedes ion movement, thus increasing electrical resistivity. while at lower curing temperatures, the pozzolanic reactions in fly ash are less activated compared to higher temperatures.

As a result, there is a reduced formation of additional cementitious compounds such as calcium silicate hydrate (CSH) gel, which contributes to a less dense microstructure and lower electrical resistivity [7] [8] [9] [10]. This was evident in the results of FA samples cured at 20 °C and 10 °C, which obtained much lower resistance values of 26.76 kΩ.cm and 13.46 kΩ.cm respectively. The increase rate of SCC-FA at 10 °C, 20 °C, and 50 °C compared to SCC-C at the same curing temperatures was 37.5%, 73.2%, and 88%, respectively.
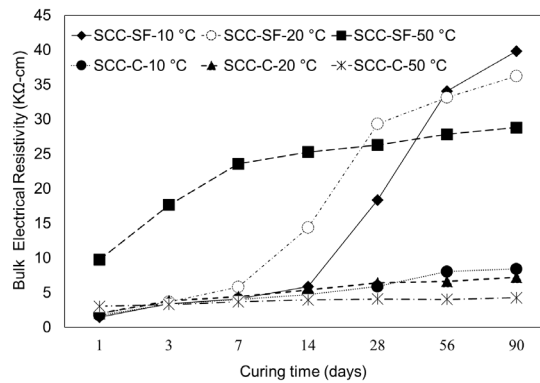


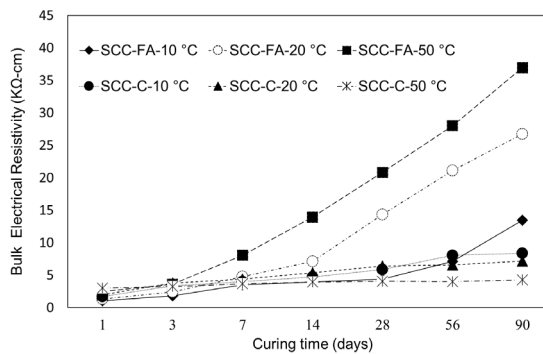Fig. 1. Results of electrical resistivity of cement mix and SF mix cured at 10 °C, 20 °C and 50 °C.



Fig. 2. Results of electrical resistivity of cement mix and FA mix cured at 10 °C, 20 °C and 50 °C.

The Effect of Curing Temperature and Supplementary
Cementitious Materials on Chloride Permeability of
Self-Compacting Concrete

41

## CONCLUSION

This study emphasizes the significant impact of curing
temperatures and supplementary cementitious materials
(SCMs) on self-compacting concrete (SCC) properties.
It highlights the importance of considering factors such
as hydration reactions, pore structure development,
and ion movement when evaluating SCC performance
and durability across different curing conditions. Lower
curing temperatures promote the formation of a denser
microstructure over time, enhancing electrical resistance,
while higher temperatures can lead to larger pores and
decreased resistivity.

The incorporation of SCMs like silica fume (SF) and fly ash
(FA) improves SCC resistance, though effects vary with
temperature. SF contributes to denser concrete matrices,
especially at lower temperatures, while FA enhances
resistance, particularly at higher temperatures, through
activated pozzolanic reactions. These findings underline the
complex relationship between curing conditions, SCMs, and
concrete properties, offering valuable insights for optimizing
SCC performance in diverse construction scenarios.

*Conflicts of Interest*
*The authors declare no conflict of interest.*

## REFERENCES

[1] H. Okamura and K. Ozawa, 'Self-Compacting High
Performance Concrete', *Structural Engineering
International*, vol. 6, no. 4, pp. 269–270, Nov. 1996.
doi.org/10.2749/101686696780496292

[2] W. Zhu, J. C. Gibbs, and P. J. M. Bartos, 'Uniformity of in
situ properties of self-compacting concrete in full-scale
structural elements', *Cement and Concrete Composites*,
vol. 23, no. 1, pp. 57–64, Feb. 2001.
doi.org/10.1016/S0958-9465(00)00053-6

[3] H. Okamura and M. Ouchi, 'Self-Compacting Concrete',
*ACT*, vol. 1, no. 1, pp. 5–15, 2003.
doi.org/10.3151/jact.1.5

[4] S. Kolias and C. Georgiou, 'The effect of paste
volume and of water content on the strength and
water absorption of concrete', *Cement and Concrete
Composites*, vol. 27, no. 2, pp. 211–216, Feb. 2005.
doi.org/10.1016/j.cemconcomp.2004.02.009

[5] W. Sun, H. Chen, X. Luo, and H. Qian, 'The effect of
hybrid fibers and expansive agent on the shrinkage and
permeability of high-performance concrete', *Cement
and Concrete Research*, vol. 31, no. 4, pp. 595–601, Apr.
2001.
doi.org/10.1016/S0008-8846(00)00479-8

[6] U. Angst, B. Elsener, C. K. Larsen, and Ø. Vennesland,
'Critical chloride content in reinforced concrete — A
review', *Cement and Concrete Research*, vol. 39, no. 12,
pp. 1122–1138, Dec. 2009.
doi.org/10.1016/j.cemconres.2009.08.006

[7] L. Basheer, J. Kropp, and D. J. Cleland, 'Assessment
of the durability of concrete from its permeation
properties: a review', *Construction and Building
Materials*, vol. 15, no. 2–3, pp. 93–103, Mar. 2001.
doi.org/10.1016/S0950-0618(00)00058-1

[8] D. J. Naus and H. L. Graves, 'A Review of the Effects
of Elevated Temperature on Concrete Materials and
Structures', in *Volume 1: Plant Operations, Maintenance
and Life Cycle; Component Reliability and Materials
Issues; Codes, Standards, Licensing and Regulatory
Issues; Fuel Cycle and High Level Waste Management*,
Miami, Florida, USA: ASMEDC, Jan. 2006, pp. 615–624.
doi.org/10.1115/ICONE14-89631

[9] D. Wang, X. Zhou, Y. Meng, and Z. Chen, 'Durability of
concrete containing fly ash and silica fume against
combined freezing-thawing and sulfate attack',
*Construction and Building Materials*, vol. 147, pp.
398–406, Aug. 2017.
doi.org/10.1016/j.conbuildmat.2017.04.172

[10] R. Madandoust and S. Y. Mousavi, 'Fresh and hardened
properties of self-compacting concrete containing
metakaolin', *Construction and Building Materials*, vol.
35, pp. 752–760, Oct. 2012.
doi.org/10.1016/j.conbuildmat.2012.04.109

[11] N. Chahal, R. Siddique, and A. Rajor, 'Influence of
bacteria on the compressive strength, water absorption
and rapid chloride permeability of fly ash concrete',
*Construction and Building Materials*, vol. 28, no. 1, pp.
351–356, Mar. 2012.
doi.org/10.1016/j.conbuildmat.2011.07.042

[12] N. Lahmar *et al.*, 'Experimental and finite element
analysis of shrinkage of concrete made with recycled
coarse aggregates subjected to thermal loading',
*Construction and Building Materials*, vol. 247, p. 118564,
Jun. 2020.
doi.org/10.1016/j.conbuildmat.2020.118564

[13] E. Rozière, S. Granger, Ph. Turcry, and A. Loukili,
'Influence of paste volume on shrinkage cracking
and fracture properties of self-compacting concrete',
*Cement and Concrete Composites*, vol. 29, no. 8, pp.
626–636, Sep. 2007.
doi.org/10.1016/j.cemconcomp.2007.03.010

[14] M. Nasir, O. S. Baghabra Al-Amoudi, and M.
Maslehuddin, 'Effect of placement temperature and
curing method on plastic shrinkage of plain and
pozzolanic cement concretes under hot weather',
*Construction and Building Materials*, vol. 152, pp.
943–953, Oct. 2017.
doi.org/10.1016/j.conbuildmat.2017.07.068

[15] J. Tang, H. Cheng, Q. Zhang, W. Chen, and Q. Li,
'Development of properties and microstructure of
concrete with coral reef sand under sulphate attack
and drying-wetting cycles', *Construction and Building
Materials*, vol. 165, pp. 647–654, Mar. 2018.
doi.org/10.1016/j.conbuildmat.2018.01.085

[16] Y. Li, J. Bao, and Y. Guo, 'The relationship between
autogenous shrinkage and pore structure of cement
paste with mineral admixtures', *Construction and
Building Materials*, vol. 24, no. 10, pp. 1855–1860, Oct.
2010.
doi.org/10.1016/j.conbuildmat.2010.04.018

[17] EFNARC, 'Specification and Guidelines for Self-
Compacting Concrete' Rep. from *EFNARC*, vol. 44,
no. February, p. 32, 2002, [online]. Available: https://
wwwp.feb.unesp.br/pbastos/c.especiais/Efnarc.pdf

Pradana KR

*Cardiff University*
*School of Engineering*

Alnajideen M

*Cardiff University*
*School of Engineering*

NET ZERO

# Techno-Economic Environment Assessment of Carbon Capture Storage when Retrofitting Coal-Fired Power Plants in Indonesia

The implementation of Carbon Capture and Storage (CCS) in coal-fired power plants offers a viable solution for reducing greenhouse gas emissions. CCS captures carbon dioxide ($CO_2$) emissions, transporting them to storage sites underground or for industrial use. Despite challenges like high costs and suitable storage requirements, CCS is crucial for meeting climate targets. This study assesses CCS implementation in fossil fuel power plants, focusing on the Indonesia Government State Owned Electricity Company, PT. PLN (Persero). Using the Integrated Environmental Control Model (IECM), it evaluates feasibility, efficiency, and environmental impact. The research investigates energy requirements, costs, and carbon capture efficiency, considering retrofitting CCS technologies. Through detailed analysis, it evaluates the increased cost of electricity in plants with CCS, factoring in infrastructure investments.

## INTRODUCTION

Indonesia contributed about 1.7% of global carbon emissions in 2023. The vast majority of CO2 emissions in the energy sector come from the burning of fossil fuels such as coal, oil and natural gas for power generation accounts for 32% of the total CO2 emissions, as shown in Fig. 1. Figure 2 illustrates that coal provides 61% of electricity in Indonesia.
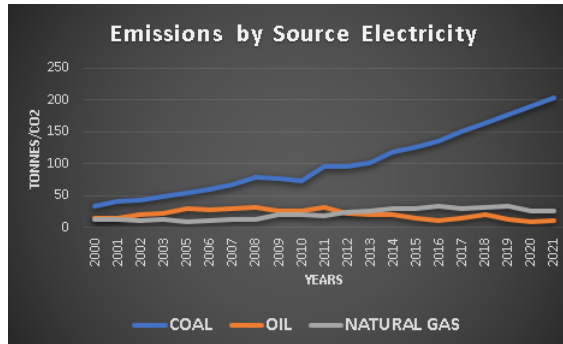


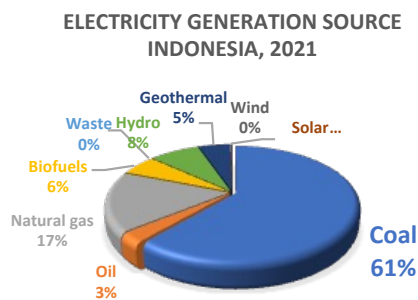Fig. 1. Total emission in electricity [1].



Fig. 2. Electricity generation source [1].

Indonesia's government intends to implement fuel switching from oil to gas, diesel to mixed biofuel, diesel to gas and to roll out the use of more efficient and low carbon technology [2]. However, this dependence raises environmental concerns, particularly regarding carbon dioxide (CO2) emissions. Retrofitting existing fossil fuel power plants with carbon capture and storage (CCS) technology emerges as a promising strategy to address these concerns.

Post-combustion, pre-combustion, and oxyfuel are three key carbon capture and storage (CCS) technologies with distinct advantages and limitations. Post-combustion capture involves removing CO2 from the flue gas after combustion, making it suitable for retrofitting existing power plants [3]. Pre-combustion capture, on the other hand, involves converting fossil fuels into syngas before combustion, enabling CO2 separation and capture prior to power generation [4]. Oxyfuel combustion, utilizing oxygen instead of air during combustion, produces a flue gas stream with a higher CO2 concentration, facilitating easier capture and storage [4]. Each technology offers unique opportunities for reducing emissions from fossil fuel power plants, with factors such as energy efficiency, cost-effectiveness, and scalability influencing their suitability for different applications as shown in Table 1.

| Oxy Combustion | Pre Combustion | Post Combustion |
|---|---|---|
| *Advantages* | | |
| Produces high efficiency steam cycle | Lower energy requirement than other | Applicable for existing and new coal fired power plant |
| Low level pollutants emissions | Requires less amount of water than other | Most commonly used technology in ccs |
| *Disadvantages* | | |
| High energy penalty | Significant loss energy than post combustion | Low co2 partial pressure at ambient pressure |
| High overall cost | High equipment cost | Need more water than other |

Table 1. Strengths and weaknesses of CCS methods [5].

Post-combustion capture technologies vary in their efficiency, energy requirements, and cost-effectiveness. Common techniques include aqueous amine scrubbing, pressure swing adsorption, and membrane separation, each with its advantages and limitations [3, 4]. Aqueous amine scrubbing, for example, involves passing the flue gas through a liquid solvent, such as monoethanolamine (MEA) and ammonia, which selectively absorbs CO2 molecules. The solvent is then regenerated through heating to release the captured CO2 for compression and storage (Fig. 3).
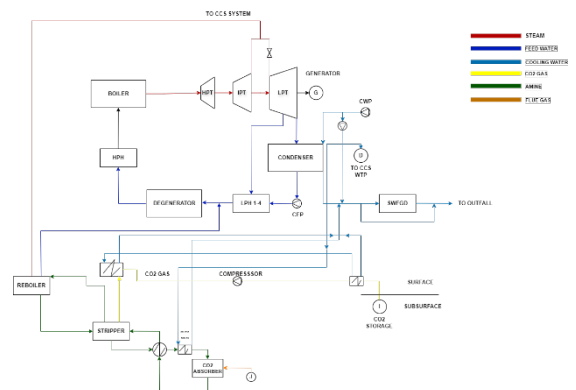


Fig. 3. Illustration of typical CFPP with a CCUS System.

The performance and cost-effectiveness of post-combustion capture technologies depend on factors such as the concentration and composition of CO2 in the flue gas, the availability and cost of capture solvents, and the energy penalties associated with capture and regeneration processes [3, 4]. Techno-economic assessments utilizing simulation tools like Integral Environment Control Mode (IECM) enable researchers to evaluate the feasibility of post-combustion capture retrofitting in specific case studies, considering factors such as plant size, fuel type, and operational conditions [6]. By incorporating detailed engineering models, economic parameters, and environmental considerations.

## MATERIALS AND METHODS

*Input Data IECM*
The methodology employed for modeling coal-fired power plant capacity in Indonesia involves compiling data on existing power plants, including their names, capacities, and fuel types. Each power plant is assigned a unique identifier, and relevant information such as capacity and fuel classification is recorded systematically. Additionally, the total capacity of all coal-fired power plants is calculated to provide an overview of the cumulative generation capacity in the country.

The modeling process requires meticulous data collection from reliable sources such as government agencies, energy companies, and industry reports to ensure accuracy and completeness. The classification of fuel types, categorized into different classes, enables the characterization of the coal used for power generation, considering factors such as calorific value and sulfur content. This classification informs decisions regarding fuel procurement, emissions control, and environmental compliance. Additionally, the average capacity of coal-fired power plants is calculated to provide insights into the typical size and scale of operations in the industry. shown in Table 2 below.

| Items | Value | References |
|---|---|---|
| Gross electrical output (MWh) | 2500 MWh | [9] |
| Type generation | Sub-critical | [7] |
| Capacity factor (%) | 64% | [8] |
| Plant location | Indonesia | |
| Fuel cost (USD/Ton) | 36.9 | [9] |
| Coal properties | Class 2 | [7] |
| Coal rank | Sub Bituminous | [7] |
| Carbon storage type | EOR | [10] |
| Pipeline distance | 134 | [10] |
| Emission rate (Kg/kWh) | 0.62 | [11] |
| Cost of electricity (USED/MWH) | 75.05 | [8] |

Table 2. IECM technical data.



Fig. 4. CFPP and CCS schemes in Indonesia.

## RESULTS

The results in Fig. 5 demonstrate significant variations in net electrical output and energy penalties among different CCS technologies compared to the scenario without CCS implementation. In the scenario without CCS, the net electrical output is the highest at 2266 MW. However, with the introduction of CCS technologies utilizing amine and ammonia, there are notable reductions in net electrical output. Specifically, the amine-based CCS technology achieves a net electrical output of 2020 MW, while the ammonia-based CCS technology yields a slightly lower output of 1903 MW. This reduction in net electrical output can be attributed to the energy penalties associated with CCS implementation. The amine-based CCS technology incurs an energy penalty of 156 MW, while the ammonia-based CCS technology experiences a higher penalty of 562 MW. These energy penalties reflect the additional energy requirements for the capture and separation of $CO_2$ from flue gas streams.
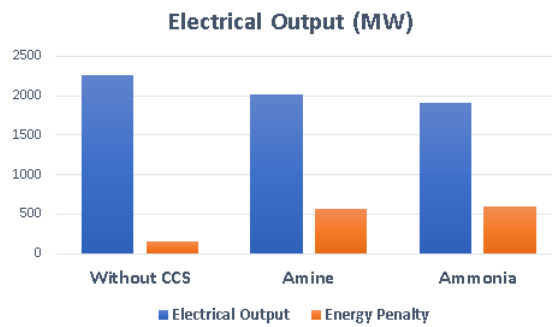


Fig. 5. Electrical output.

The results in Fig. 6 reveal significant differences in the total levelized annual cost and associated costs for $CO_2$ capture, transport, and storage among various carbon capture and storage (CCS) technologies compared to the scenario without CCS implementation. In the scenario without CCS, the total levelized annual cost is the lowest at 531.6 M$/yr. However, with the integration of CCS technologies utilizing amine and ammonia, there are notable increases in total levelized annual costs. Specifically, the amine-based CCS technology incurs the highest total levelized annual cost of 588.6 M$/yr, followed closely by the ammonia-based CCS technology at 553.4 M$/yr.

This increase in costs is primarily attributed to the expenses associated with $CO_2$ capture, transport, and storage. Interestingly, while the amine-based CCS technology has a higher total levelized annual cost, it requires lower expenses for $CO_2$ capture, transport, and storage compared to the ammonia-based CCS technology. This discrepancy highlights the varying cost structures and operational requirements of different CCS technologies. Overall, the results underscore the importance of evaluating not only the net electrical output but also the total economic implications.
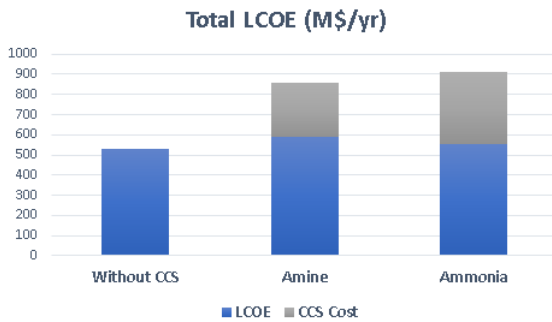
**Techno-Economic Environment Assessment of Carbon Capture Storage when Retrofitting Coal-Fired Power Plants in Indonesia**

45

Fig. 6 Total LCOE.

The results in Fig. 7 illustrate substantial reductions in carbon dioxide (CO2) emissions with the implementation of carbon capture and storage (CCS) technologies compared to the scenario without CCS. In the scenario without CCS, CO2 emissions are highest, totaling 7.34E+04 metric megatonnes. However, with the integration of CCS technologies utilizing amine and ammonia, there are significant reductions in CO2 emissions. Specifically, the amine-based CCS technology achieves a notable decrease in CO2 emissions, with only 8554 metric tons emitted annually. Similarly, the ammonia-based CCS technology also demonstrates substantial CO2 emission reductions, with emissions totaling 8324 metric tons annually. These reductions underscore the effectiveness of CCS technologies in mitigating CO2 emissions from fossil fuel power plants. The results highlight the potential of CCS to contribute significantly to greenhouse gas reduction efforts, aligning with global climate goals and emphasizing the importance of integrating CCS into energy transition strategies for a sustainable future.
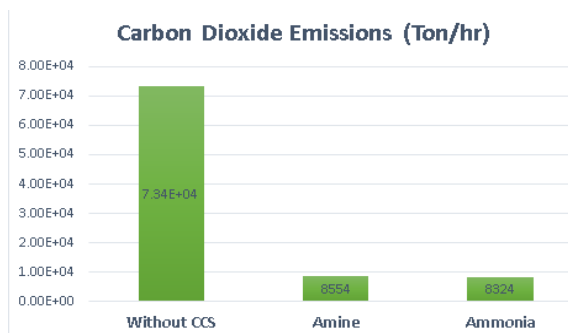


Fig. 7. CO2 emissions.

**DISCUSSION**

The substantial reductions in carbon dioxide (CO2) emissions achieved through the implementation of carbon capture and storage (CCS) technologies, as evidenced by the significant differences in emissions between the scenarios with and without CCS, align with findings from previous research emphasizing the role of CCS in mitigating greenhouse gas emissions from fossil fuel power plants. The observed variations in net electrical output, total levelized annual cost, and associated CO2 capture expenses among different CCS technologies further highlight the importance of considering not only technical performance but also economic feasibility and operational requirements when evaluating CCS deployment options.

From the perspective of working hypotheses, the findings corroborate the hypothesis that CCS technologies can effectively reduce CO2 emissions from coal-fired power plants while also providing insights into the trade-offs involved, such as the impact on net electrical output and associated costs. These results underscore the complexity of CCS implementation and emphasize the need for comprehensive techno-economic assessments to inform decision-making processes.

In the broader context, the implications of the findings extend to global climate change mitigation efforts, emphasizing the potential of CCS to contribute significantly to reducing greenhouse gas emissions from the power generation sector. However, challenges such as high implementation costs and energy penalties underscore the importance of continued research and innovation to optimize CCS technologies and enhance their cost-effectiveness and efficiency.

Future research directions may focus on addressing key knowledge gaps and uncertainties surrounding CCS, including advancing capture technologies, optimizing CO2 transport and storage infrastructure, and exploring policy mechanisms and incentives to facilitate CCS deployment. Moreover, interdisciplinary collaboration and stakeholder engagement are essential for overcoming barriers and accelerating the transition to a low-carbon energy future.

**CONCLUSIONS**

The results of this study underscore the significant potential of carbon capture and storage (CCS) technologies to mitigate carbon dioxide (CO2) emissions from fossil fuel power plants. The substantial reductions in CO2 emissions achieved through the implementation of CCS, as evidenced by the comparison with the scenario without CCS, highlight the effectiveness of these technologies in addressing climate change concerns. However, the observed variations in net electrical output, total levelized annual cost, and associated CO2 capture expenses among different CCS technologies emphasize the importance of conducting comprehensive techno-economic assessments to inform decision-making processes.

*Conflicts of Interest*
*The authors declare no conflict of interest.*

**REFERENCES**

[1]  International Energy Agency, *Energy Outlook: Indonesia*, 2021 [online]. Available: https://www.iea.org/countries/indonesia/electricity

[2]  PLN. *Electricity Supply Business Plan 2031-2040*, p.45, 2022.

[3]  H.J. Herzog, B. Eliasson, and O. Kaarstad, 'Capturing Greenhouse Gases', *Sci. Am.*, vol. 282, no. 2, pp. 72–79, Feb. 2000.
doi: 10.1038/scientificamerican0200-72

[4]  Intergovernmental Panel on Climate Change (IPCC), *Special Report on Carbon Dioxide Capture and Storage*. Cambridge: Cambridge University Press, 2005.

[5]  A. Salma, L. Fryda, and H. Djelal, 'Biochar: A Key Player in Carbon Credits and Climate Mitigation', *Resources* 13(2), p.31, 2024.
doi.org/10.3390/resources13020031

[6]  E.S. Rubin and H. Zhai, 'The cost of carbon capture and storage for natural gas combined cycle power plants', *Environmental Science and Technology'*, 46(6) pp.3076-3084, 2012.
doi.org/10.1021/es204514f

[7]  PLN, Consultation Service For Study About Mass, Volume and Energy Balance of Carbon Capture and Storage for Coal Powerplant.

[8]  PLN. *Electricity Supply Business Plan 2031-2040,* p.81, 2022.

[9]  JWC Indonesia, *Price Index*, 2023 [online]. Available at https://www.jwcindonesia.com/price-index

[10]  International Energy Agency, *Carbon Capture, Utilisation and Storage in Indonesia*, 2023 [online]. Available at https://www.iea.org/reports/carbon-capture-utilisation-and-storage-in-indonesia

[11]  Ember, *Indonesia* , 2023 [online]. Available at https://ember-climate.org/countries-and-regions/countries/indonesia/

Sharifi S
*Cardiff University*
*School of Engineering*

Balzano B
*Cardiff University*
*School of Architecture*

Novelli V
*Cardiff University*
*School of Engineering*

Pinto S
*Cardiff University*
*School of Engineering*

FUTURE ENGINEERING

# Effective Concrete Crack Closure Through Innovative Hybrid PET Tendons

The article delves into the enduring challenge of cracking in concrete structures, examining innovative solutions, with particular emphasis on the development and assessment of a novel Tendon (the Side PET Hybrid Tendon (SPHT)). Traditional approaches to crack closure often prove inadequate in terms of both effectiveness and cost efficiency. Through the fusion of Kevlar®, PET, and Kanthal wire, the SPHT exhibits promising abilities in effectively sealing cracks. Laboratory trials showed significant reductions in crack sizes when the tendons were activated, achieving reductions of 60% to 80%. This underscores their potential to greatly enhance the durability of concrete structures. The SPHT presents a feasible remedy for addressing cracking in concrete structures, offering a pathway towards enhanced longevity and diminished maintenance requirements.

## INTRODUCTION

Cracking stands as a significant factor in the degradation of concrete, enabling the infiltration of chemicals and potentially resulting in the deterioration of the physical, mechanical, and enduring qualities of concrete constructions [1]. With heightened expectations for extended service life, the persistence of cracks continues to pose a challenge, as they significantly reduce the lifespan of concrete structures [2]. In addressing the issue of cracking in concrete, self-healing technologies emerge as an innovative and promising solution. These advancements hold the potential to enhance the durability and lifespan of infrastructure [3].

Numerous researchers have extensively investigated self-healing concrete, contributing to various aspects and potential applications [4]. These methods primarily include vascular self-healing [5], capsule-based self-healing [6], microbiological self-healing [3], electrodeposition self-healing [7], self-healing via shape memory Materials [8].

One highly effective approach involves employing shape memory materials. These materials demonstrated their capability to seal cracks through the force generated by their shrinkage following activation. Although certain types of shape memory materials, like Shape Memory Alloy (SMA), have displayed a notable capacity to close cracks [9], some researchers have directed their attention to Shape Memory Polymer (SMP) due to the comparatively high cost of SMA materials [10][11].

Among the most promising types of SMP is polyethylene terephthalate (PET), which has demonstrated its capability to seal cracks in plain concrete elements [12]. However, its effectiveness was limited in reinforced concrete and heavy structures due to the relatively low strength of shrinkage [13].

Some researchers have sought to enhance the crack-closing capabilities of PET by incorporating them into prestressed tendons. This approach aims to store prestressed force within the tendons, in this manner enhancing their effectiveness in sealing cracks [10]. Despite efforts, the force stored in the tendons has remained insufficient, highlighting the necessity to enhance their capacity for storing prestressed force. Furthermore, the utilization of PET throughout the entire length of the tendons leads to increased costs, coupled with a significant demand for energy to activate them. It's crucial to highlight that based on the tendons structure, substantial energy is wasted due to inefficient activation methods like oven placement or direct contact with concrete[10] . This not only escalates energy consumption but also poses a risk of harming the concrete structure.

To overcome these disadvantages and limitations, this research explores enhancing the crack closure method used in PET tendons by introducing the Side PET Hybrid Tendon (SPHT). The SPHT consists of an inner core made from Kevlar (a type of aramid fibre) and a piece of PET tube on one side, serving as the sealer. During the manufacturing process, the inner core of a tendon is put into tension and the outer sleeve into compression, such that the tendon is in equilibrium. A Kanthal wire thermal coil has been utilised to supply the necessary heat for activating the tendons after cracking. This coil is embedded within the sealer, ensuring it stays insulated from direct contact with the concrete.

## GENERAL CONCEPT

The SPHT tendon consists of inner and outer steel tubes sliding on each other. Inside these tubes, there is a pre-drawn PET tube contain a coil of Kanthal wire (26AWG) acting as a heating generator or activator,. Additionally, it features a pre-stressed core composed of Kevlar® rope, which will be sealed by clamps. The Kevlar® has relatively high strength and low modulus. High strength is necessary for prestressing and reinforcement purposes as it ensures the structural integrity to the tendon, while a low modulus helps minimise prestress losses caused by creep and shrinkage in the mortar or concrete [10]. The components of the tendon are depicted in Fig. 1.
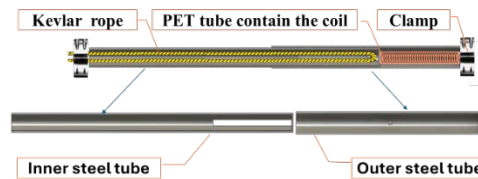


Fig. 1. The components of the tendon.

The pre-stressed core remains constrained by the PET tube until activation occurs. Upon activation, the tension stored within the tendon is released, applying a compressive force on the structure element. This force effectively closes any cracks that develop perpendicular to the axis of the tendon.

The initial phase of manufacturing involves pre-tensioning the inner rob and applying an initial elastic stress. Once the inner cable reaches the desired pre-stress level, the entire system is secured using a commercially available wire clamp. The principle behind the tendon design is shown in Fig. 2.

The tendon will be embedded into the concrete structural element (Fig.3a). Upon the appearance of cracks, the SPHT is activated through heat generated by the coil. This results in the shrinking of PET, thereby releasing the tensile force stored in the Kevlar. Following this, the tendons exert a compressive force on the concrete element through their clamps (Fig.3b). The inclusion of post-tensioning in the beam, combined with the use of stainless steel (304) as inner and outer tube in the tendons, enables both pre- and post-activation unbonded reinforcement. This capability presents the possibility of completely substituting conventional reinforcement within the system.



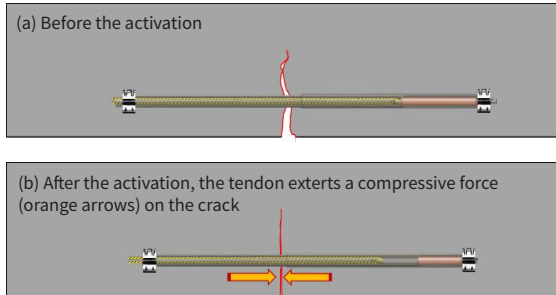Fig. 2. Distribution load and image of the tendon.

Fig. 3. The concept of crack closure by the tendons.

## MATERIALS AND TENDON MANUFACTURE

*Concrete mix*
The concrete mix comprised Portland cement CEM II A/L 32.5 R (CAS number 65997–15-1), sand (CAS number 14808–100 60–7), 10mm aggregates, and tap water. Cement, sand, and aggregates were mixed in a mass ratio of 1:1.55:2.1, with a w/c ratio of 0.55 by mass. After demoulding (24 hours after casting), the specimens were promptly covered with damp hessian for 6 days following the guidelines of BS EN 12390–2:2019. The choice to use wet hessian instead of a water tank was influenced by safety concerns related to the electrical aspects of the experiment.

The compressive strength exhibited a mean value of 31 MPa with a coefficient of variation of 0.3, whereas the tensile splitting strength showed a mean value of 2.5 MPa with a coefficient of variation of 0.13.

*Kevlar® core robe*
Kevlar®, an organic fibre categorised within the aramid family, exhibits notable tensile strength. Table 1 provides details on the mechanical properties of the Kevlar that utilised in this investigation.

| Tensile Strength MPa | Young Modulus MPa | Density kg/m3 |
|---|---|---|
| 600 | 5-7 ×103 | 1440 |

Table 1. The mechanical properties of the Kevlar.

*Steel tubes*
The steel tubes come in two sizes: 16 mm and a 12 mm with a slug, allowing them to slide over each other. The geometric characteristics of the tubes are depicted in Fig. 4.
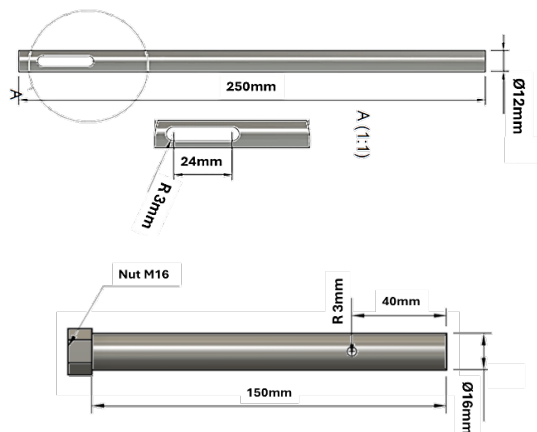


Fig.4. The geometrical properties of the tendon.

*PET tubes and coil*
The PET tube has a diameter of 10 mm and a length of 80 mm. It houses a Kanthal coil with a length of 60 mm and a coil spacing of 0.2 mm (Fig.5). When an electric current is applied to the coil, it generates heat, activating the PET and causing the tube to shrink.



Fig.5. The PET tube and the coil inside it.

The tendons are each 400 mm in length and were cast in pairs at a height of 15 mm from the bottom of the beam. Each tendon stores a force of 2500 N.

## LABORATORY EXPERIMENTS

*Experiment set up*
The tendons' performance was evaluated by embedding them in beams with tendons, along with a control beam (without tendons), all measuring 500x10x10mm. Additionally, four cubes and four cylinders were cast to assess the mix strength. Following curing, notches (0.3 mm wide and 0.5 mm deep) were created in the beams to induce crack formation. Subsequently, the beams were loaded in three-point bending, resulting in the formation of cracks around 0.12 mm wide. Following this, the coils were energised for a period of 1 minute using a power supply providing a voltage of 10 volts and a current of 5 amperes. This resulted in an energy consumption of 3000 joules (calculated as Energy=Power × Time=10 V×5 A×60s). This activation process aimed to generate the necessary heat to activate the PET tubes, as depicted in Fig.6.
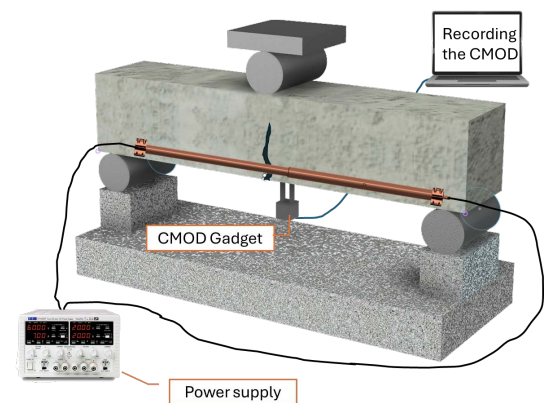


Fig.6. The set up of the experiment.

The size of the crack was continuously monitored using a Crack Mouth Opening Displacement (CMOD) gadget. Additionally, the cracks were photographed both before and after activation using a digital microscope.

## RESULTS AND DISCUSSION

Unfortunately, one of the beams did not crack from the notch during formation, rendering the CMOD device unable to measure the crack size and amount of crack closure. Fig.7 illustrates the force-CMOD responses of the test for other two beams. The initial peak in the response signifies the emergence of the first visible crack on the material. Prior to reaching this peak load, the material exhibits a nearly linear behaviour, where increased force leads to a proportional increase in crack opening. Once the max peak load is reached, the force exerted on the material diminishes rapidly. However, in samples containing tendons, the force begins to rise again until a specific limit of crack opening is attained. This phenomenon suggests that the tendons are functioning as unbonded reinforcement.
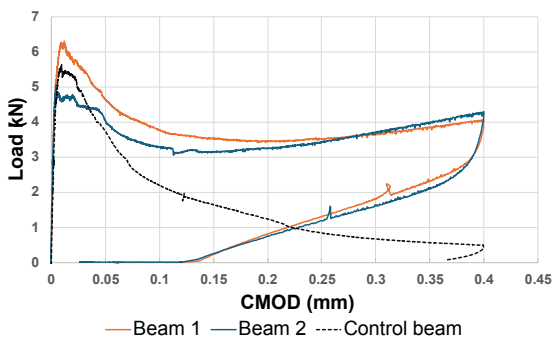


Fig. 7. The force-CMOD diagram.

It occurs due to the tendons generating a hogging moment that counters the sagging moment (bending downwards) applied to the specimens. These opposing forces induced by the tendons cause the overall applied load on the specimen to ascend again following the initial post-peak decline. Once the desired CMOD was achieved, the beams were unloaded, resulting in a reduction in CMOD size. This reduction may be attributed to aggregate interlocking and closure of microcracks [10].

The tendons were activated, and as designed, they successfully reduced crack sizes in beams 1and 2. The crack reduction achieved was 60% for beam 1 and 80% for beam 2 (Fig.7 and 8). These reductions resulted in final CMOD values that are well below the level for significant autogenous (natural) healing to be necessary in the beams.

## CONCLUSIONS

In conclusion, the development and evaluation of the SPHT represent a significant advancement in the quest to address cracking in concrete structures. Through a meticulous combination of materials and design, this innovative tendon demonstrates promising capabilities in effectively sealing cracks and enhancing the durability of concrete elements. However one of the beams was lost, the experiment has shown impressive results, with significant reductions in crack sizes achieved upon activation of the tendons. These findings not only underscore the efficacy of the SPHT but also offer potential for its widespread adoption in concrete construction, where durability and longevity are paramount concerns.

Further study could involve the development of tendons capable of storing higher force and transitioning to the ability to use a single tendon instead of a pair.

*Conflicts of Interest*
*The authors declare no conflict of interest.*



Fig. 8. The crack before (left) and after (right) the activation of the tendons.

## REFERENCES

[1] M. Nodehi, T. Ozbakkaloglu, and A. Gholampour, 'A systematic review of bacteria-based self-healing concrete: Biomineralization, mechanical, and durability properties', *Journal of Building Engineering*, vol. 49, p. 104038, May 2022.
doi: 10.1016/j.jobe.2022.104038

[2] M. G. Alexander, 'Service life design and modelling of concrete structures – background, developments, and implementation', *Revista de la Asociación Latinoamericana de Control de Calidad, Patología y Recuperación de la Construcción*, vol. 8, no. 3, pp. 224–245, Aug. 2018
doi: 10.21041/ra.v8i3.325

[3] V. G. Cappellesso, T. Van Mullem, E. Gruyaert, K. Van Tittelboom, and N. De Belie, 'Bacteria-based self-healing concrete exposed to frost salt scaling', *Cement and Concrete Composites*, vol. 139, p. 105016, May 2023
doi: 10.1016/j.cemconcomp.2023.105016

[4] L. Ferrara *et al.*, 'Experimental characterization of the self-healing capacity of cement based materials and its effects on the material performance: A state of the art report by COST Action SARCOS WG2', *Construction and Building Materials*, vol. 167, pp. 115–142, Apr. 2018.
doi: 10.1016/j.conbuildmat.2018.01.143

[5] E. Vangansbeke, Y. Shields, N. De Belie, K. Van Tittelboom, and E. Tsangouri, 'Autonomous healing by vascular networks: tracking of cracks interaction by Ultrasounds and Acoustic Emission', *MATEC Web Conf.*, vol. 378, p. 04003, 2023.
doi: 10.1051/matecconf/202337804003

[6] A. Sinha, Q. Wang, and J. Wei, 'Feasibility and Compatibility of a Biomass Capsule System in Self-Healing Concrete', *Materials*, vol. 14, no. 4, p. 958, Feb. 2021.
doi: 10.3390/ma14040958

[7] D. Guergova, E. Stoyanova, D. Stoychev, I. Avramova, and P. Stefanov, 'Self-healing effect of ceria electrodeposited thin films on stainless steel in aggressive 0.5 mol/L NaCl aqueous solution', *Journal of Rare Earths*, vol. 33, no. 11, pp. 1212–1227, Nov. 2015.
doi: 10.1016/S1002-0721(14)60548-2

[8] W. Chen, K. Feng, Y. Wang, Y. Lin, and H. Qian, 'Evaluation of self-healing performance of a smart composite material (SMA-ECC)', *Construction and Building Materials*, vol. 290, p. 123216, Jul. 2021.
doi: 10.1016/j.conbuildmat.2021.123216

[9] W. Chen, B. Lin, K. Feng, S. Cui, and D. Zhang, 'Effect of shape memory alloy fiber content and preloading level on the self-healing properties of smart cementitious composite (SMA-ECC)', *Construction and Building Materials*, vol. 341, p. 127797, Jul. 2022.
doi: 10.1016/j.conbuildmat.2022.127797

[10] B. Balzano, J. Sweeney, G. Thompson, C.-L. Tuinea-Bobe, and A. Jefferson, 'Enhanced concrete crack closure with hybrid shape memory polymer tendons', *Engineering Structures*, vol. 226, p. 111330, Jan. 2021.
doi: 10.1016/j.engstruct.2020.111330

[11] O. Teall *et al.*, 'A shape memory polymer concrete crack closure system activated by electrical current', Smart Mater. Struct., vol. 27, no. 7, p. 075016, Jul. 2018.
doi: 10.1088/1361-665X/aac28a

[12] A. Jefferson, C. Joseph, R. Lark, B. Isaacs, S. Dunn, and B. Weager, 'A new system for crack closure of cementitious materials using shrinkable polymers', *Cement and Concrete Research*, vol. 40, no. 5, pp. 795–801, May 2010.
doi: 10.1016/j.cemconres.2010.01.004

[13] O. Teall *et al.*, 'Development of high shrinkage polyethylene terephthalate (PET) shape memory polymer tendons for concrete crack closure', *Smart Mater. Struct.*, vol. 26, no. 4, p. 045006, Apr. 2017.
doi: 10.1088/1361-665X/aa5d66

## Zheng J

*Cardiff University*
*School of Engineering*

## Bhaduri D

*Cardiff University*
*School of Engineering*

## Brousseau E

*Cardiff University*
*School of Engineering*

FUTURE ENGINEERING

# Modelling of Temperature Distribution in Orthogonal Machining

Heat generation during machining has a profound effect on the performance of cutting tools, tool life, machinability of materials, and workpiece surface integrity. Thus, measurement and monitoring of cutting temperature is necessary for tool condition monitoring as well as to achieve the targeted surface and mechanical integrity of the produced parts. However, experimental measurement of cutting temperature could often be challenging, time consuming and cost intensive, and hence prediction of temperature distribution at the machining zone via modelling is imperative. This study verifies and validates prior analytical models from the literature to generate the temperature distribution patterns within the cutting tool, chip, and workpiece during macro-machining. The temperature fields at the shear zone (chip-workpiece interface) and at the friction zone (chip-tool interface) are generated using MATLAB software. The data closely matches with the range of cutting zone temperature found in the literature, with only ~6-7% deviation.

*Nomenclature*

| | |
|---|---|
| $a$ | thermal diffusivity, m²/s. |
| $B$ | fraction of the shear plane heat source conducted into the work material. |
| $(1-B)$ | fraction of the shear plane heat source conducted into the chip. |
| $c$ | Specific heat, J/g °C. |
| $l_i$ | location of the differential small segment of the shear band heat source d relative to the upper end of it and along its width, m. |
| $L$ | width of the shear band heat source, m. |
| $q_{pl}$ | heat liberation intensity of a moving plane heat source, J/ms. |
| $q_{pli}$ | heat liberation intensity of an induced plane heat source, J/ms. |
| $q_{pls}$ | heat liberation rate of the shear plane heat source, J/ms. |
| $R$ | distance between the moving line heat source and point M, where the temperature rise is concerned, m. |
| $r$ | chip thickness ratio (= $t_c$ / $t_{chip}$ or $V_{ch}$ / $V_c$). |
| $t_c$ | depth of cut, or undeformed chip thickness, m. |
| $w$ | width of cut, m. |
| $X, z$ | the coordinates of the point where the temperature rise is concerned in the moving coordinate system, m. |
| $\Theta_M$ | temperature rise at point M, °C. |
| $C, m, k$ | variable parameters, the range of C 2-2.2, the range of m 0.22-0.26, k=16. |
| $\varphi$ | oblique angle, degree. |
| $\alpha$ | rake angle, degree. |

## INTRODUCTION

Since the development of the theoretical models of metal cutting back in the 1940's, assessment of heat generation and the consequent temperature distribution patterns at the machining zone has received considerable attention from the research community. Experimental techniques for measuring the total temperature at the machining zone have been developed over decades. These methods typically involve use of bi-metallic thermocouples or utilising the tool-workpiece combination as a thermocouple. However, experimental measurement of cutting temperature could often be challenging, time consuming and cost intensive. Thus, prediction of cutting temperature has been attempted via analytical and finite element-based modelling. The advent of computer technology has led to the increasing use of theoretical analysis methods, which are faster, time saving, and can predict fairly accurate and reliable temperature data during machining.

In orthogonal machining, heat is generated in three areas: at the primary shear zone between workpiece and chip; at the secondary friction zone between chip and cutting tool, and at the tertiary friction zone between cutting tool and workpiece. To simplify the modelling process, Komanduri and Hou [1-3] first introduced by Hahn (Proceedings of First U.S. National Congress of Applied Mechanics 1951. p. 661–6 only considered the heat source at the first two zones and ignored the friction heat between the tool and the workpiece. Hahn [4] developed a thermal model by considering a moving heat source. The study analysed the effect of different shear angles on the average temperature at the shear zone and the model showed good agreement with experimental data. Jaeger [5] also considered moving heat sources to predict temperature. A study was conducted to classify heat sources as either moving or stationary. When dealing with a heat source in motion, the temperature inside the material undergoes constant change, resulting in a dynamic temperature field. Hahn's model [4] was modified by Trigger and Chao [6], who applied it to an infinite plane. They used this theoretical model to calculate the temperatures at the shear and friction zones and compared them with the measured experimental data. The theoretical results showed a 15% increase in temperature compared to the experimental results, which was considered as a reasonable margin of error. This demonstrates that modifying parameters using this method can result in more precise temperature prediction models. In orthogonal machining, Hahn's model was modified by Komanduri and Hou [1-3] to create the temperature distribution patterns at the chip and workpiece interface, caused by the shear zone heat source. Similarly, Jaeger's model [5] was adapted to produce models of chip and tool temperatures influenced by the secondary friction zone heat source. Integrating the models provides a temperature distribution model when heat sources act at the shear and friction zones simultaneously. By incorporating Trigger and Chao's model [6], a complete temperature distribution model for the workpiece, chip, and tool can be obtained. However, this temperature prediction model for machining is only valid at the macro scale. When the temperature prediction model is applied in a micro-machining scenario, the effects of rubbing and ploughing, together with shear, will need to be taken into account. This paper presents a verification and validation of the prior work on analytical temperature modelling, by using MATLAB software which was not used in the previous studies.

## MATERIALS AND METHODS

*Materials*
Detailed machining parameters are shown in Tables 1 and 2. In particular, Table 1 was used to calculate the temperature distribution in the chip and workpiece due to the shear plane heat source only. In this case, the dimension of the workpiece was 300 μm x 150 μm. The data in Table 2 were employed to calculate the temperature distribution in the chip, tool, and workpiece considering both the frictional heat source and the shear plane heat source. For this, the dimension of the workpiece was 2000 μm x 500 μm.

| Work material | SAE B1113 steel |
|---|---|
| Tool | K2S carbide 20° rake, 5° clearance angle |
| Type of cut | Orthogonal |
| Cutting speed | $V_c$ = 2.32 m/s |
| Undeformed chip thickness | $t$ = 0.00006 m |
| Width of cut | $w$ = 0.00384 m |
| Chip contact length | $L_c$ = 0.0023 m |
| Cutting force | $F_c$ = 356 N |
| Feed force | $F_t$ = 125 N |
| Chip thickness ratio | $r$ = 0.51 |
| Thermal diffusivity | $a$ = 0.00001484 m²/s |
| Thermal conductivity | $\lambda$ = 56.7 W/mK |

Table 1. Cutting data from Loewen and Shaw [7].

| Work material | Steel NE 9445 |
|---|---|
| Tool | Triple carbide, rake angle $\alpha$ = 4° |
| Type of cut | Orthogonal |
| Cutting speed | $V_c$ = 1.524 m/s |
| Depth of cut | $t_c$ = 0.0002484 m |
| Width of cut | $w$ = 0.002591 m |
| Length of tool-chip contact | $L$ = 0.001209 m |
| Cutting force | $F_c$ = 1681.3 N |
| Feed force | = 854.0 N |
| Chip thickness ratio | $F_t$ = 0.375 |
| ***Thermal properties*** | |
| Work material: NE 9445 steel | $\lambda$ = 38.88 w/mK $a$ = 0.000008234 m²/s |
| Tool: carbide | $\lambda_{tool}$ = 41.9w/mK $a_{tool}$ = 0.0000104 m²/s |

Table 2. Cutting data from Trigger and Chao [6].

*Methods*
This work primarily replicates the temperature model developed by Komanduri and Hou [1-3], although by using MATLAB R2023a software, whereas [1-3] utilised an unspecified computer program. The materials listed in Tables 1 and 2 were also used in [1-3]. Komanduri and Hou [1-3] determined the temperature distributions resulted by the shear and friction plane heat sources and then combined them together to calculate the total temperature rise during orthogonal machining. The heat from the shear plane is transferred to the workpiece and chip, and the temperature rise at any point in the workpiece and

chip can be determined by Eq. 1 and 2. At the same time, the temperature distribution at any point in the tool is calculated by Eq. 3.

When considering the frictional heat source, the temperature rise at any point in the chip can be calculated by Eq. 4, 5 and 6, while the temperature rise at any point in the tool is governed by Eq. 7, 8 and 9. Five temperature distribution curves were derived for the chip, workpiece, and tool. The tool and chip temperatures were then superimposed to produce the final temperature profile. Equations 5, 6 and 10 can be used to calculate the temperature of the chip when both the shear plane heat source and the friction plane heat source are considered. Equations 8 - 12 can be used to calculate the temperature of the tool. Equation 1 can be used to calculate the temperature of the workpiece.

(1)
$$\theta_{M_{workpiece}} = \frac{q_{pl}}{2\pi\lambda} \int_{l_i=0}^{L} e^{-\frac{(X-l_i\sin\varphi)V}{2a}} \left\{ \begin{array}{l} K_0\left[\frac{V}{2a}\sqrt{(X-l_i\sin\varphi)^2+(z-l_i\cos\varphi)^2}\right] \\ +K_0\left[\frac{V}{2a}\sqrt{(X-l_i\sin\varphi)^2+(z+l_i\cos\varphi)^2}\right] \end{array} \right\} dl_i$$

(2)
$$\theta_{M_{chip}} = \frac{q_{pls}}{2\pi\lambda} \int_{w_i=0}^{t_{ch}/\cos(\phi-\alpha)} e^{-(X-X_i)V/2a} \left\{ \begin{array}{l} K_0\left[\frac{V}{2a}\sqrt{(X-X_i)^2+(z-z_i)^2}\right] \\ +K_0\left[\frac{V}{2a}\sqrt{(X-X_i)^2+(2t_{ch}-z-z_i)^2}\right] \end{array} \right\} dw_i$$

(3)
$$\theta_{M\_tool} = \frac{q_{pli}}{2\pi\lambda_{tool}} \left\{ \begin{array}{l} (B_{ind}+\Delta B_i)\int_{y_i=-b_0}^{+b_0} dy_i \int_{x_i=0}^{L} \left(\frac{1}{R_i}+\frac{1}{R_i'}\right)dx_i \\ -2\Delta B_i \int_{y_i=-b_0}^{+b_0} dy_i \int_{x_i=0}^{L} \left(\frac{x_i}{L}\right)^m \left(\frac{1}{R_i}+\frac{1}{R_i'}\right)dx_i \\ -C_i\Delta B_i \int_{y_i=-b_0}^{+b_0} dy_i \int_{x_i=0}^{L} \left(\frac{x_i}{L}\right)^k \left(\frac{1}{R_i}+\frac{1}{R_i'}\right)dx_i \end{array} \right\}$$

(4)
$$\theta_{M\_chip} = \frac{q_{pl}}{\pi\lambda} \left\{ (B_{chip}-\Delta B)\int_{l_i=0}^{L} e^{-(X-l_i)V/2a}[K_0(R_iv/2a)+K_0(R_i'v/2a)]dl_i \right.$$
$$+ 2\Delta B \int_{l_i=0}^{L} \left(\frac{l_i}{L}\right)^m e^{-(X-l_i)v/2a}[K_0(R_iv/2a)+K_0(R_i'v/2a)]dl_i$$
$$\left. + C\Delta B \int_{l_i=0}^{L} \left(\frac{l_i}{L}\right)^k e^{-(X-l_i)v/2a}[K_0(R_iv/2a)+K_0(R_i'v/2a)]dl_i \right\}$$

(5) $\quad R_i = \sqrt{(X-l_i)^2+z^2}$

(6) $\quad R_i' = \sqrt{(X-l_i)^2+(2t_{ch}-z)^2}$

(7)
$$\theta_{M\_tool} = \frac{q_{pl}}{2\pi\lambda} \left\{ \begin{array}{l} (B_{tool}+\Delta B)\int_{y_i=-b_0}^{+b_0} dy_i \int_{x_i=0}^{L} \left(\frac{1}{R_i}+\frac{1}{R_i'}\right)dx_i \\ -2\Delta B \int_{y_i=-b_0}^{+b_0} dy_i \int_{x_i=0}^{L} \left(\frac{x_i}{L}\right)^m \left(\frac{1}{R_i}+\frac{1}{R_i'}\right)dx_i \\ -C\Delta B \int_{y_i=-b_0}^{+b_0} dy_i \int_{x_i=0}^{L} \left(\frac{x_i}{L}\right)^k \left(\frac{1}{R_i}+\frac{1}{R_i'}\right)dx_i \end{array} \right\}$$

(8) $\quad R_i = \sqrt{(x-x_i)^2+(y-y_i)^2+z^2}$

(9) $\quad R_i = \sqrt{(x-2L+x_i)^2+(y-y_i)^2+z^2}$

(10)
$$\theta_{M\_chip} = \frac{q_{pl}}{\pi\lambda} \left\{ (B_{chip}-\Delta B)\int_{l_i=0}^{L} e^{-(X-l_i)v/2a}[K_0(R_iv/2a)+K_0(R_i'v/2a)]dl_i \right.$$
$$+ 2\Delta B \int_{l_i=0}^{L} \left(\frac{l_i}{L}\right)^m e^{-(X-l_i)v/2a}[K_0(R_iv/2a)+K_0(R_i'v/2a)]dl_i$$
$$\left. + C\Delta B \int_{l_i=0}^{L} \left(\frac{l_i}{L}\right)^k e^{-(X-l_i)v/2a}[K_0(R_iv/2a)+K_0(R_i'v/2a)]dl_i \right\}$$
$$+ \frac{q_{pls}}{2\pi\lambda} \int_{w_i=0}^{t_{ch}/\cos(\phi-\alpha)} e^{-(X-X_i)V/2a} \left\{ \begin{array}{l} K_0\left[\frac{V}{2a}\sqrt{(X-X_i)^2+(z-z_i)^2}\right]+ \\ K_0\left[\frac{V}{2a}\sqrt{(X-X_i)^2+(2t_{ch}-z-z_i)^2}\right] \end{array} \right\} dw_i$$

(11)

$$\theta_{M\_tool} = \frac{q_{pl}}{2\pi\lambda} \begin{Bmatrix} (B_{tool} + \Delta B) \int_{y_i=-b_0}^{+b_0} dy_i \int_{x_i=0}^{L} \left(\frac{1}{R_i} + \frac{1}{R_i'}\right) dx_i - \\ 2\Delta B \int_{y_i=-b_0}^{+b_0} dy_i \int_{x_i=0}^{L} \left(\frac{x_i}{L}\right)^m \left(\frac{1}{R_i} + \frac{1}{R_i'}\right) dx_i \\ -C\Delta B \int_{y_i=-b_0}^{+b_0} dy_i \int_{x_i=0}^{L} \left(\frac{x_i}{L}\right)^k \left(\frac{1}{R_i} + \frac{1}{R_i'}\right) dx_i \end{Bmatrix}$$

$$+ \frac{q_{pli}}{2\pi\lambda_{tool}} \begin{Bmatrix} (B_{ind} + \Delta B_i) \int_{y_i=-b_0}^{+b_0} dy_i \int_{x_i=0}^{L} \left(\frac{1}{R_i} + \frac{1}{R_i'}\right) dx_i \\ -2\Delta B_i \int_{y_i=-b_0}^{+b_0} dy_i \int_{x_i=0}^{L} \left(\frac{x_i}{L}\right)^m \left(\frac{1}{R_i} + \frac{1}{R_i'}\right) dx_i \\ -C_i\Delta B_i \int_{y_i=-b_0}^{+b_0} dy_i \int_{x_i=0}^{L} \left(\frac{x_i}{L}\right)^k \left(\frac{1}{R_i} + \frac{1}{R_i'}\right) dx_i \end{Bmatrix}$$

(12)  $x_i = l_i$

## RESULTS AND DISCUSSION

The MATLAB reproduction of the temperature distribution data across the tool, workpiece and chip is shown in Figs. 1 and 2. The temperature values are largely consistent with that of Komanduri and Hou's model [1-3], although some discrepancies were noted.

Figure 1 shows the temperature distribution generated by shear plane heat source between the chip and workpiece. The temperature of the workpiece at the shear plane is ~120°C, whereas the maximum temperature of the chip is 280°C. In contrast, the temperature is lower (only ~140°C) when closer to the chip-tool interface region. In the workpiece, the temperature is ~20°C higher than that of [1-3], at the equivalent locations. Figure 2 shows the average temperature distributions in the workpiece, chip, and tool. Difference in the materials' properties cause temperature variations at the contact surfaces. The maximum temperature at the chip-tool contact surface is 700°C, which decreases as the distance from the contact surface increases. The maximum temperature of the workpiece in the middle of the shear plane reaches up to ~250°C. The maximum temperature at the chip-workpiece contact surface, within the chip was ~420-430°C, which was marginally higher than that reported in [1-3].
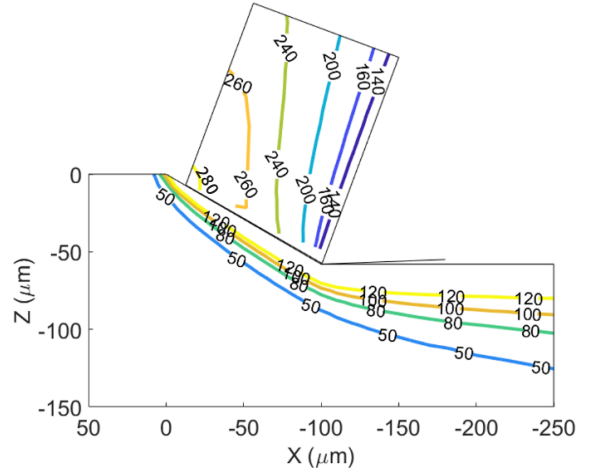


Fig. 1. Temperature distribution in the chip and workpiece due to the shear plane heat source.

The temperature plots using MATLAB did not produce smooth curves within the chips, nearer the shear plane. This was possibly because fewer points were generated by the matrix when calculating the temperature values. Nonetheless, the temperature distribution data was roughly in agreement with [1-3], with ~6-7% variation. Using the MATLAB2023 version, the first temperature model in Fig. 1 was obtained in 5 minutes, while the second model in Fig. 2 was calculated in 14 minutes. Currently, the program's running time is considerably lengthy. As more parameters and complexities will be added in subsequent temperature modelling for micro and nanomachining scenarios, modifications are necessary to shorten the program's running time and to increase its efficiency.
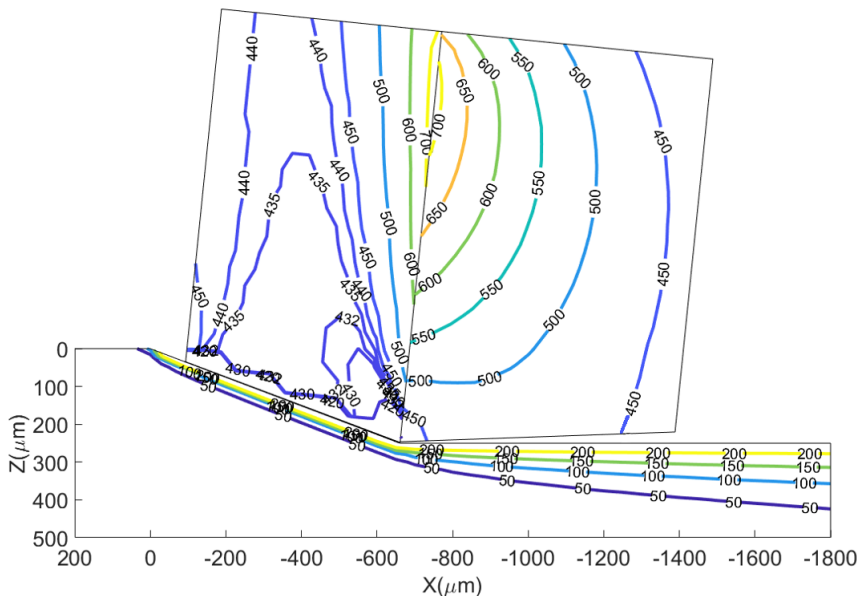


Fig. 2. Temperature distribution in the chip, tool, and workpiece considering both the frictional heat source and the shear plane heat source. Material: Steel NE 9445.

## CONCLUSIONS

The temperature distribution data resulted from the shear plane and friction plane heat sources matches well with the prior analytical models. Thus, it is feasible to use MATLAB programs to adopt the model for predicting machining temperatures at a macroscopic level. Future work will focus on modifying these models to predict temperatures during micro and nanomachining. This will require encompassing the effects of rubbing and ploughing as material failure modes, together with the conventional shear failure mechanism.

*Conflicts of Interest*
*The authors declare no conflict of interest.*

## REFERENCES

1.   R. Komanduri and Z. B. Hou, 'Thermal modeling of the metal cutting process', *International Journal of Mechanical Sciences*, vol. 42, no. 9, pp. 1715–1752, Sep. 2000.
     doi.org/10.1016/S0020-7403(99)00070-3

2.   R. Komanduri and Z. B. Hou, 'Thermal modeling of the metal cutting process — Part II: temperature rise distribution due to frictional heat source at the tool–chip interface', *International Journal of Mechanical Sciences*, vol. 43, no. 1, pp. 57–88, Jan. 2001.
     doi.org/10.1016/S0020-7403(99)00104-6

3.   R. Komanduri and Z. B. Hou, 'Thermal modeling of the metal cutting process — Part III: temperature rise distribution due to the combined effects of shear plane heat source and the tool–chip interface frictional heat source', *International Journal of Mechanical Sciences*, vol. 43, no. 1, pp. 89–107, Jan. 2001.
     doi.org/10.1016/S0020-7403(99)00105-8

4.   R.S. Hahn, 'On the temperature developed at the shear plane in the metalcutting process', *Journal of Applied Mechanics-Transactions of the ASME*. vol. 18. no. 3, pp.323-323, 1951.

5.   J. C. Jaeger, 'Moving sources of heat and the temperature at sliding contacts', *Journal and Proceedings of the Royal Society of New South Wales*, vol. 76, no. 3, pp. 203-224, May 1943.
     doi.org/10.5962/p.360338

6.   K. J. Trigger and B. T. Chao, 'An Analytical Evaluation of Metal-Cutting Temperatures', *Journal of Fluids Engineering*, vol. 73, no. 1, pp. 57–66, Jan. 1951.
     doi.org/10.1115/1.4016141

7.   E. G. Loewen and M. C. Shaw, 'On the Analysis of Cutting-Tool Temperatures', *Journal of Fluids Engineering*, vol. 76, no. 2, pp. 217–225, Feb. 1954.
     doi.org/10.1115/1.4014799

Escudero-Ornelas AY

*Cardiff University*
*School of Engineering*

Bigot S

*Cardiff University*
*School of Engineering*

Valera-Medina A

*Cardiff University*
*School of Engineering*

Bhaduri D

*Cardiff University*
*School of Engineering*

FUTURE ENGINEERING

# A Study on the Influence of Laser Surface Texturing Parameters on the Dimensional Accuracy of the Textured Designs

The research involves an experimental investigation into the laser surface texturing (LST) of stainless steel 316L parts to explore the correlation between the laser process parameters and the dimensional accuracy of the textured designs. A full factorial experimental design was used to analyse the impact of the input parameters via main effects plot and analysis of variance (ANOVA) test. The results indicated that laser track distance along the traverse scanning direction had the most significant effects on all the output responses, i.e. width and depth of the textured grooves and width of the riblet (unmachined region). Laser intensity also had significant effect on the riblet width and groove depth, while scanning velocity did not exhibit any statistically significant influence on any of the responses. The deviations in the riblet and groove widths from the nominal CAD design were the least when using a track distance of 10 μm, whereas the deviations in the groove depth was minimum for a track distance of 100 μm.

## INTRODUCTION

Topological modification, such as surface texturing, is frequently employed to enhance specific properties and performance characteristics of surfaces [1]. In the energy sector, microtextures have demonstrated their effectiveness in reducing energy consumption and improving the tribological properties of various components, including turbines and swirl burners [1,2]. Each component has a certain characteristic that surface texturing aims to enhance. To achieve this goal, these topological modifications can be inspired by biomimetic designs. Some biomimetic designs such as the lotus, scallop, sharkskin, and diamond have already proved to enhance certain characteristics, such as wettability, surface drag, anti-corrosion etc. However, the dimensional parameters of each design can vary, leaving ample opportunity to optimise these parameters.

To test the performance of a textured design, a simulation is typically performed to predict the fluid properties of the texture for a particular application, to reduce the cost of the experimental validation. Once the texture design is successfully optimised it is possible to manufacture these designs on real objects. Nevertheless, the produced textures often display deviations in the dimension from the nominal values used in the simulation. This leads to deviation in the experimental results from the simulated values [3]. Consequently, as a preliminary step to enable the manufacturing process closely adhering to the intended CAD design, this research aims to identify the key process parameters for the fabrication process. Several studies have explored different texture manufacturing technologies, such as micro electro-discharge machining (μ-EDM) and abrasive-based jet machining (ABJM) [4], together with identifying some design and processing challenges. Laser surface texturing (LST) is an alternative manufacturing technology that is clean, automated, flexible and does not involve any dielectric fluid or abrasive slurry [5]. In LST, a laser beam is focused on the surface to remove material by melting and vaporisation. However, this often results in the deviation of texture dimensions from the nominal values. Thus, the aim of the research is to investigate the capability of LST to accurately produce the targeted dimensions from a CAD texture design, together with analysing the surface roughness of the produced textured surfaces [6]. The ultimate is to ensure that the resulting textures closely resemble those designed for the simulation. To achieve this, the LST parameters were evaluated to determine their effects on the texture dimension and roughness, using a full factorial experimental design [7]. The influence of laser intensity, scanning velocity and laser track distance on the texture dimensions was assessed while maintaining the laser pulse frequency and focal distance constant.
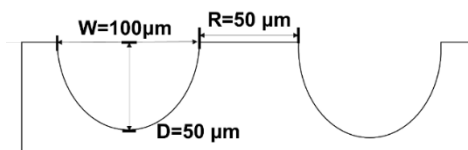
## MATERIALS AND METHODS

*Workpiece material and texture design*
Stainless steel 316L square workpiece samples, measuring $35 \times 35 \times 2$ mm$^3$ were used. Channel texture design was selected for this study, the nominal dimensions of a single channel as seen on the cross-section is in Fig 1. The three simulated and measured texture dimensions were the width and depth of the channel, and the width of the riblet.
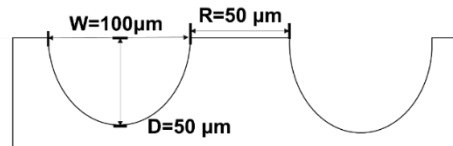


Fig. 1. The dimensional parameters of the Groove texture: Width (W), Depth (D) and Riblet (R).

*Machine and equipment*
Laser texturing was carried out on a Lasertec DMG-40 nanosecond fibre laser machine, with 0.25 mJ laser energy and 80 kHz frequency. The surface topography measurements on the textures were carried out using a 3D optical profilometer Sensofar SMART, with 10X magnification. Representative textured topographies are shown in Fig. 2. The dimensional parameters (groove depth, groove width and riblet width) were measured at five different locations on each specimen, as shown in Fig. 3. Three measurements were taken at each location. The average dimensions and the deviations from the nominal values were recorded.
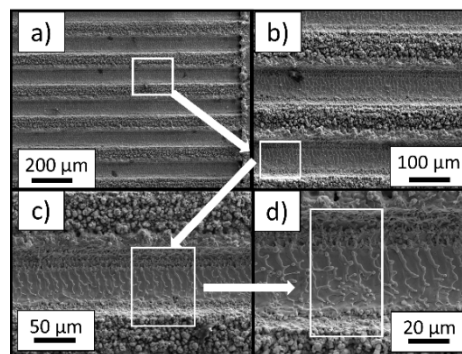


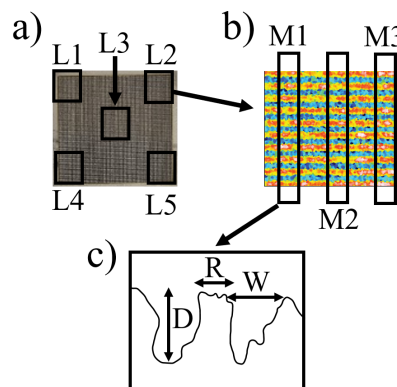Fig. 2. SEM images of Groove texture at different magnifications.



Fig. 3. (a) The five locations on each specimen, (b) three measured areas at each location, and (c) dimensional parameters measured within each area.

A Study on the Influence of Laser Surface Texturing
Parameters on the Dimensional Accuracy of the
Textured Designs

59

*Experimental array*

Experiments were carried out using a full factorial design involving three factors at three levels that resulted in 27 trials, allowing for a comprehensive exploration of the main effects and interactions among these factors.

Table 1 lists the three input parameters, viz. laser intensity (I), scanning velocity (v) and laser track distance (T), together with their respective levels.

| Input parameters | Units | Levels | | |
|---|---|---|---|---|
| | | 1 | 2 | 3 |
| Laser intensity (I) | % | 60 | 80 | 100 |
| Scanning velocity (v) | mm/s | 600 | 800 | 1000 |
| Laser track distance (T) | μm | 10 | 50 | 100 |

Table 1. Factors and their levels.

## RESULTS AND DISCUSSION

The Analysis of Variance (ANOVA) results corresponding to the mean riblet width, mean groove width and mean groove depth, together with the deviations in these dimensions from the nominal values are presented in Table 2. The main effect plots for the aforementioned responses are shown in Fig 4. It is revealed that laser track distance (T) had the most significant effect ($p<0.05$) on all the response variables with the PCRs varying from ~68-83%.

Laser intensity (I) also had statistically significant influence ($p<0.05$) on the mean riblet width and mean groove depth with PCRs of ~5% and 18%, respectively. In contrast, laser scanning velocity (v) did not exhibit significant effects on any of the response variables, with p-values greater than 0.05 and relatively low PCRs (~0.3-5%), suggesting that its impact was minimal compared to that of T and I.

The impact of the input factors on the dimensional deviations of the response variables from their nominal CAD values was also analysed. Laser track distance again showed the maximum influence on the dimensional deviations of all three output responses.

**(a) Mean riblet width**

| Source | DF | SS | MS | P-value | PCR% |
|---|---|---|---|---|---|
| I | 2 | 331.87 | 165.94 | 0.045 | 5.09* |
| v | 2 | 19.85 | 9.93 | 0.762 | 0.30 |
| T | 2 | 5448.43 | 2724.21 | 0.000 | 83.49* |
| Error | 8 | 282.50 | 35.31 | | 4.33 |
| Total | 26 | 6525.61 | | | 100 |

**(b) Mean groove width**

| Source | DF | SS | MS | P-value | PCR% |
|---|---|---|---|---|---|
| I | 2 | 99.48 | 49.74 | 0.563 | 1.99 |
| v | 2 | 254.70 | 127.35 | 0.264 | 5.10 |
| T | 2 | 3404.66 | 1702.33 | 0.001 | 68.19* |
| Error | 8 | 644.02 | 80.50 | | 12.90 |
| Total | 26 | 4993.22 | | | 100 |

**(c) Mean groove depth**

| Source | DF | SS | MS | P-value | PCR % |
|---|---|---|---|---|---|
| I | 2 | 1609.2 | 804.59 | 0.001 | 18.09* |
| v | 2 | 179.3 | 89.65 | 0.188 | 2.02 |
| T | 2 | 6230.7 | 3115.37 | 0.000 | 70.06* |
| Error | 8 | 345.8 | 43.23 | | 3.89 |
| Total | 26 | 8894.0 | | | 100 |

**(d) Deviation riblet width**

| Source | DF | SS | MS | P-value | PCR% |
|---|---|---|---|---|---|
| I | 3 | 43.290 | 43.290 | 0.252 | 7.86 |
| v | 2 | 8.363 | 8.363 | 0.736 | 1.52 |
| T | 2 | 183.038 | 2724.21 | 0.018 | 33.23* |
| Error | 8 | 105.142 | 35.31 | | 19.08 |
| Total | 26 | 550.980 | | | |

**(f) Deviation groove width**

| Source | DF | SS | MS | P-value | PCR % |
|---|---|---|---|---|---|
| I | 2 | 96.36 | 48.18 | 0.363 | 8.05 |
| v | 2 | 25.41 | 12.71 | 0.746 | 2.12 |
| T | 2 | 331.51 | 165.76 | 0.063 | 27.69 |
| Error | 8 | 333.93 | 41.74 | | 27.89 |
| Total | 26 | 1197.07 | | | |

**(g) Deviation groove depth**

| Source | DF | SS | MS | P-value | PCR % |
|---|---|---|---|---|---|
| I | 2 | 314.36 | 157.181 | 0.020 | 37.42* |
| v | 2 | 30.05 | 15.025 | 0.553 | 3.58 |
| T | 2 | 172.50 | 86.251 | 0.074 | 20.53 |
| Error | 8 | 188.45 | 23.556 | | 22.43 |
| Total | 26 | 840.04 | | | |

Table 2. ANOVA analysis on the mean (a) riblet width, (b) groove width, (c) groove depth and (d), (e), (f) their corresponding dimensional deviations.
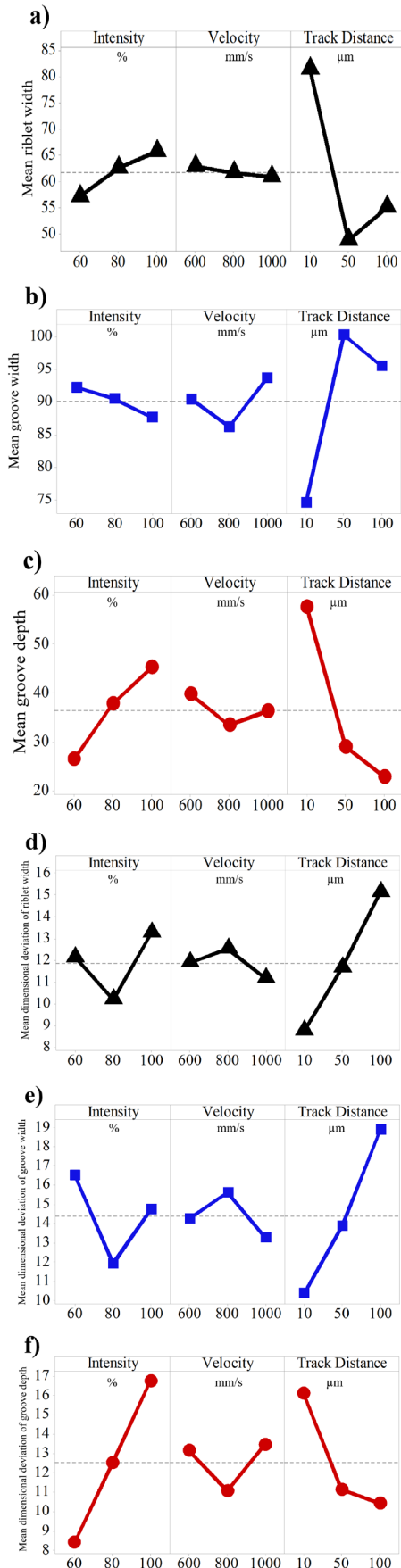
Fig. 4. Main effect plots for mean (a) riblet width, (b) groove width, (c) groove depth and (d), (e), (f) their corresponding dimensional deviations.

The ANOVA analysis on the dimensional deviations shows that laser intensity (I) had the most significant effect on the deviation of groove depth, with a PCR of 37.42% and a p-value of 0.020, which is less than 0.05, indicating statistical significance. Laser scanning velocity (v) did not exhibit significant effects on any of the dimensional deviations, with p-values greater than 0.05 and relatively low PCRs (ranging from 1.52% to 3.58%), suggesting that its impact was minimal compared to that of T and I. The error terms in the ANOVA tables account for a considerable portion of the total variability in the dimensional deviations (ranging from 19.08% to 27.89%).

Regarding the two-way interactions, the overall interaction effect (I × v, I × T, v × T) was not statistically significant for any of the riblet dimensions (riblet width, groove width, and groove depth), with p-values of 0.491, 0.787, and 0.506, respectively. The PCRs for the two-way interactions were also relatively low, ranging from 5.95% to 11.82%, indicating that the combined effects of any two factors did not considerably influence the response variables beyond their individual main effects. Among the two-way interactions, the interaction between intensity and track distance (I × T) had the highest PCR for both riblet width (4.06%) and groove width (7.61%), while the interaction between velocity and track distance (v × T) had the highest PCR for groove depth (2.97%). However, these interactions were still not statistically significant, with p-values greater than 0.05. The low PCRs and high p-values for all the two-way interactions suggest that the input factors can be optimised independently.

**CONCLUSIONS**

The present study investigated the capability of LST to accurately reproduce proposed dimensions from nominal CAD designs on 316 stainless steel surfaces. The aim was to ensure that the resulting texture closely resembled those designed for the simulation. The ANOVA results revealed that laser track distance had the most significant effect on all the response variables. The two-way interactions were not statistically significant, suggesting that the combined effects of any two factors did not significantly influence the response variables beyond their individual main effects.

These findings further suggest that the laser track distance is the most critical parameter in accurately reproducing the proposed dimensions from the CAD design using LST. By carefully controlling the track distance, the resulting texture can be optimised to closely resemble the designed simulation. Laser intensity also plays an important role for certain response variables and should be considered in the process optimisation. To further improve the dimensional accuracy of the laser textured geometries future studies could focus on testing a wider range of the track distance and laser intensity parameters, as well as investigating the effects of other factors, such as material properties (thermal conductivity, reflectivity, diffusivity), and prior surface preparation techniques, such as removal of surface contaminants.

*Conflicts of Interest*
*The authors declare no conflict of interest.*

## REFERENCES

[1]   H. Martinez-Zavala, D. Bhaduri, A. Valera-Medina, S. Bigot, 'Experimental study on heat transfer enhancement during condensation using microstructured surfaces'. *Int. Conf. Appl. Energy*, 2019. doi.org/10.46855/energy-proceedings-2320

[2]   D. V. Feoktistov, D. O. Glushkov, G. V. Kuznetsov, E. G. Orlova, and K. K. Paushkina, 'Ignition and combustion enhancement of composite fuel in conditions of droplets dispersion during conductive heating on steel surfaces with different roughness parameters', *Fuel*, vol. 314, p. 122745, Apr. 2022. doi: 10.1016/j.fuel.2021.122745

[3]   D. Bhaduri et al., 'On Design and Tribological Behaviour of Laser Textured Surfaces', *Procedia CIRP*, vol. 60, pp. 20–25, 2017. doi: 10.1016/j.procir.2017.02.050

[4]   E. Brinksmeier, B. Karpuschewski, J. Yan, and L. Schönemann, 'Manufacturing of multiscale structured surfaces', *CIRP Annals*, vol. 69, no. 2, pp. 717–739, 2020. doi: 10.1016/j.cirp.2020.06.001

[5]   I. Gnilitskyi et al., 'Nano patterning of AISI 316L stainless steel with Nonlinear Laser Lithography: Sliding under dry and oil-lubricated conditions', *Tribology International*, vol. 99, pp. 67–76, Jul. 2016. doi: 10.1016/j.triboint.2016.03.011

[6]   Q. Li, Y. Zeng, M. Zhao, and R. Tian, 'Simulation Analysis of the Influence of Micro-texture Parameters on Tool Strength Based on ANSYS', *J. Phys.: Conf. Ser.*, vol. 1654, no. 1, p. 012076, Oct. 2020. doi: 10.1088/1742-6596/1654/1/012076

[7]   A. Q. Miah, 'Experimental Design', in *Applied Statistics for Social and Management Sciences*, A. Q. Miah (Ed.), Singapore: Springer, 2016, pp. 325–35. doi: 10.1007/978-981-10-0401-8_17

**Cynhadledd Ymchwil
Peirianneg Caerdydd**

**Cardiff Engineering
Research Conference**

**School of Engineering
Cardiff University
Queen's Buildings
The Parade
Cardiff, CF24 3AA**